https://technobius.kz/

e-ISSN 3007-0147

Technobius Physics

A peer-reviewed open-access journal

Technobius, LLP | *Volume 4, No. 2, 2026*

Technobius Physics

Volume 4, No. 2, 2026

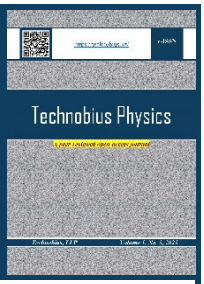

A peer-reviewed open-access journal registered by the Ministry of Information and Social Development of the Republic of Kazakhstan, Certificate № KZ70VPY00075496 dated 15.08.2023

ISSN (Online): 3007-0147
Thematic Directions: General Physics, Condensed Matter Physics
Publisher: Technobius, LLP
Address: 15/3 Sauran street, 43, 010000, Astana, Republic of Kazakhstan

Contacts:
Website: https://technobius.kz/
E-mail: technobiusphysics@gmail.com

CONTENTS

Technobius Physics, 2026, 4(2), 0050, DOI: https://doi.org/10.54355/tbusphys/30070147.4.2.2026.0050

Technobius Physics

https://technobiusphysics.kz/

e-ISSN 3007-0147

Article

Heat transfer-based analysis of building energy demand and energy systems

Aida Nazarova[1], Gulzhan Tleukenova[2], Yer-Targyn Tleukenov[3,*]

[1]School of Science and Humanities, Nazarbayev University, Astana, Kazakhstan
[2]Bau International Deutsche Energie-Agentur GmbH (DENA), Berlin, Germany
[3]Nazarbayev University Research Administration, Nazarbayev University, Astana, Kazakhstan
*Correspondence: yertargyn.tleukenov@nu.edu.kz

Abstract. This study examines the thermal performance of buildings and the efficiency of alternative energy supply systems under cold climatic conditions, with a focus on Eastern Kazakhstan. The objective is to quantify the impact of building envelope insulation and energy system configuration on heating demand, primary energy consumption, carbon emissions, and economic performance. An analytical methodology based on standardized building physics approaches was applied to determine heat demand, accounting for transmission and ventilation losses as well as internal and solar heat gains. Climatic conditions were incorporated using the heating degree-day method. Several energy supply configurations, including conventional fossil-based systems and renewable-integrated solutions, were evaluated in terms of energy, environmental, and economic indicators. The results indicate that improving the insulation standard reduces the specific heating demand from approximately 185 kWh/m²·a to 63 kWh/m²·a, corresponding to a reduction exceeding 60%. Transmission losses represent about 70% of total heat losses. Primary energy consumption decreases from approximately 280 kWh/m²·a for coal-based systems to about 110 kWh/m²·a for renewable-based configurations. Similarly, carbon emissions are reduced from 0.34 kg/kWh to 0.04 kg/kWh. Systems with higher initial investment demonstrate improved life-cycle economic performance due to lower operating costs. The findings confirm that enhanced thermal insulation combined with efficient and low-carbon energy systems constitutes a key strategy for reducing energy demand and environmental impact in cold climate regions. The proposed analytical framework provides a consistent and reproducible basis for evaluating building energy performance and supporting energy planning decisions.

Keywords: heat transfer, thermal resistance, energy balance modeling, building physics, primary energy analysis, emission assessment.

1. Introduction

Energy consumption in buildings represents a fundamental problem in applied physics, particularly within the framework of heat transfer and thermodynamics. In cold climate regions, the dominant component of energy use is associated with space heating, which is governed by conductive heat transfer through the building envelope, convective heat exchange due to air infiltration and ventilation, and radiative heat exchange with the environment. The magnitude of heating demand is determined by thermal resistance, thermal transmittance, and boundary conditions such as outdoor temperature and solar radiation. Consequently, the analysis and optimization of heat transfer processes in buildings constitute a key task for improving energy efficiency and reducing environmental impact.

The importance of this problem is underscored by the significant contribution of the building sector to global energy consumption and greenhouse gas emissions. According to recent studies, buildings account for approximately 30–40% of global final energy use, which has stimulated extensive research on improving thermal performance and energy efficiency [1], [2]. In particular, the reduction of transmission heat losses through building envelopes has been identified as one of the most effective strategies for decreasing heating demand. Advanced insulation materials and improved

construction standards have been shown to significantly reduce heat flux through external walls and roofs, thereby lowering overall energy consumption [3], [4].

Recent original research has explored various approaches to enhance building thermal performance. For example, authors [5] demonstrated that optimized envelope insulation combined with passive design strategies can reduce heating demand by more than 50% in residential buildings. Similarly, [6] investigated innovative building materials and reported that improvements in thermal conductivity and heat storage capacity can significantly influence heat transfer dynamics. Other studies have focused on phase-change materials (PCM), which regulate temperature fluctuations by storing and releasing latent heat; [7] showed that PCM-integrated walls reduce peak heating demand and improve thermal stability.

In addition to material-level improvements, several studies have examined system-level solutions. Combined heat and power (CHP) systems and hybrid renewable energy configurations have been widely investigated for their potential to reduce primary energy consumption and emissions. For instance, [8] analyzed integrated energy systems and concluded that CHP combined with renewable sources significantly improves overall system efficiency. Similarly, [9] demonstrated that biomass-based systems can substantially reduce CO_2 emissions compared to fossil fuel-based heating systems. Furthermore, dynamic simulation tools such as TRNSYS and EnergyPlus are commonly used to model building energy performance under realistic conditions [10], [11], [12]. These tools allow detailed representation of heat transfer processes and system interactions but often involve complex numerical procedures.

Despite the progress achieved, several limitations remain in the current state of research. First, many studies rely heavily on numerical simulations, which may reduce transparency and hinder reproducibility of results. Second, building thermal performance and energy supply systems are frequently analyzed separately, without establishing a clear physical link between heat transfer processes and system-level indicators such as primary energy consumption and emissions. Third, the influence of climatic severity—particularly in cold continental regions—has not been sufficiently addressed in a unified analytical framework [13].

Recent studies have increasingly focused on analytical and physics-based approaches for evaluating building thermal performance under severe climatic conditions [14], [15]. In contrast to purely numerical simulations, analytical methods allow direct interpretation of heat transfer mechanisms and provide clearer relationships between thermal resistance, climatic parameters, and energy demand [16], [17]. Several recent investigations demonstrated that physically interpretable heat transfer models can improve reproducibility and simplify comparative assessment of building energy systems in cold regions.

In addition, recent original studies published between 2020 and 2025 emphasized the importance of coupling building envelope analysis with energy system evaluation [18], [19]. For example, advanced hybrid heating systems integrating thermal storage and renewable energy sources have shown significant reductions in primary energy demand and carbon emissions under continental climate conditions [20]. These studies confirm that integrated analytical approaches remain highly relevant for improving transparency and practical applicability in building physics research.

The novelty of the present study lies not only in the use of analytical heat transfer equations, but also in the integration of building thermal analysis, primary energy assessment, emission evaluation, and life-cycle cost analysis within a single physically interpretable framework. Unlike conventional engineering calculations that typically evaluate these parameters separately, the proposed methodology establishes direct links between heat transfer processes and system-level performance indicators.

Based on these limitations, an unresolved problem can be identified: there is a lack of transparent and physically interpretable analytical methods that allow simultaneous evaluation of building heat demand and energy system performance under cold climate conditions. This gap limits the ability to clearly quantify the role of individual physical parameters and to compare different energy solutions in a consistent manner.

The objective of this study is to develop and apply such an analytical methodology for evaluating building thermal performance and energy supply systems. Specifically, the study aims to (i) quantify heating demand based on heat transfer principles, (ii) evaluate different energy system configurations in terms of primary energy consumption and carbon emissions, and (iii) assess their economic performance using a life-cycle cost approach. The novelty of this work lies in the integration of building physics and energy system analysis within a unified analytical framework, which provides a clear physical interpretation of energy processes and offers a reproducible alternative to purely simulation-based approaches.

2. Methods

2.1. Building characteristics and material properties

Two representative building types typical for urban development in Eastern Kazakhstan were considered: a multi-family residential building and an administrative office building. The selection was based on commonly used construction typologies and standard design solutions applied in Kazakhstan. The thermal properties of building envelope components, including external walls, roofs, floors, and glazing systems, were defined in accordance with national construction standards [21] and comparable European regulations [22]. For each building element, thermal transmittance (U-value) was determined using a layer-by-layer calculation method. The total thermal resistance of multilayer structures was calculated as:

$$R = R_i + \sum \frac{d_j}{\lambda_j} + R_a \quad (1)$$

where R_i and R_a represent internal and external surface resistances, d_j is the thickness of layer j, and λ_j is the thermal conductivity of the corresponding material. The heat transfer coefficient was then determined as:

$$U = \frac{1}{R} \quad (2)$$

Material properties were obtained from standardized building physics databases and regulatory documents; no experimental determination of material parameters was performed within this study.

2.2. Climatic data and boundary conditions

The analysis was conducted for the climatic conditions of Ust-Kamenogorsk, Kazakhstan, characterized by a sharply continental climate with long heating periods and significant temperature variations. Climatic boundary conditions were defined using standard meteorological datasets, including outdoor air temperature, solar radiation intensity, and wind velocity. To ensure methodological reproducibility, the heating period was determined based on the duration of days with average outdoor temperature below the heating threshold defined by SNIP standards. The climatic severity of the region was quantified using the heating degree-day (HDD) method, widely applied in building energy analysis [23]. The total HDD value was calculated as:

$$HDD = \sum (T_{int} - T_{ext}) \quad (3)$$

where T_{int} is the indoor design temperature and T_{ext} is the mean daily outdoor temperature.

2.3. Determination of building heat demand

The annual heating demand was determined using a steady-state energy balance approach in accordance with standardized building energy calculation methods [22], [23]. Transmission heat losses were calculated for each building component as:

$$Q_T = \sum U_i A_i (T_{int} - T_{ext}) \quad (4)$$

where U_i is the thermal transmittance and A_i is the surface area of component i. Ventilation heat losses were determined using the air exchange method:

$$Q_L = \dot{V} p c_p (T_{int} - T_{ext}) \quad (5)$$

where $\dot{V}$ is the volumetric airflow rate, ρ is air density, and c_p is the specific heat capacity of air. Internal heat gains from occupants, lighting, and equipment were estimated based on standardized values according to [24]. Solar heat gains were determined using glazing areas and incident solar radiation data. The total heating demand was calculated as:

$$Q_H = Q_T + Q_L - Q_I - Q_S \quad (6)$$

where Q_I and Q_S represent internal and solar heat gains, respectively.

The indoor design temperature was assumed to be 20 °C for residential buildings in accordance with SNIP thermal comfort recommendations. Ventilation air exchange rates were defined according to standardized building operation guidelines and varied between 0.5 and 0.7 h^{-1} depending on building occupancy and operational conditions. These assumptions were applied consistently throughout the analysis to ensure comparability of all investigated configurations.

2.4. Description and modeling of energy supply systems

The study considered several heating system configurations applicable to cold climate regions, including centralized and decentralized systems based on fossil fuels and renewable energy sources.

Each system was characterized by technical parameters such as nominal efficiency (η), energy carrier type, system configuration, and the presence of combined heat and power (CHP) or thermal energy storage. System performance was evaluated using engineering-based energy balance models rather than detailed dynamic simulation. Heat generation processes were modeled using efficiency-based relations, while distribution losses were accounted for using standard coefficients derived from engineering practice. Thermal storage systems were described using simplified energy balance equations considering charging and discharging processes.

2.5. Primary energy consumption and emission assessment

Primary energy consumption was calculated by applying primary energy factors in accordance with [22] and European energy performance methodologies:

$$Q_{primary} = Q_{final} \cdot f_p \quad (7)$$

where f_p is the primary energy factor associated with the respective energy carrier. Carbon dioxide emissions were estimated using emission factors obtained from internationally recognized sources (e.g., IPCC guidelines):

$$CO_2 = Q_{final} \cdot EF \quad (8)$$

where EF represents the emission factor for the corresponding fuel. All coefficients were taken from standard references and not derived experimentally within this study.

2.6. Economic evaluation method

The economic assessment of the investigated systems was performed using a life-cycle cost (LCC) approach in accordance with [25]. The annualized total cost was calculated as:

$$K_\alpha = K_{int} \cdot \alpha + K_{op} \quad (9)$$

where K_{int} represents the investment cost, K_{op} includes operational and maintenance costs, and a is the annuity factor defined as:

$$\alpha = \frac{p(1+p)^n}{(1+p)^n - 1} \quad (10)$$

where p is the interest rate and n is the system lifetime. The analysis included capital costs, fuel consumption, and maintenance expenses over the system lifecycle.

2.7. Data processing and methodological framework

All calculations were performed using numerical methods implemented in engineering calculation tools as MATLAB, Python, and Microsoft Excel. Input data included climatic parameters, building geometry, and standardized material properties. The analysis was conducted under consistent boundary conditions for all investigated configurations to ensure comparability and

reproducibility of results. No experimental measurements were carried out; the study is based entirely on analytical modeling and standardized engineering calculation procedures. The figures presented in this study are based on recalculated and generalized data derived from previously validated simulation results of the author's doctoral research.

The proposed analytical framework provides a transparent alternative to fully numerical simulation approaches and enables reproducible evaluation of building heat demand and energy system performance under cold climate conditions.

3. Results and Discussion

3.1. Thermal performance of building envelopes

The thermal performance of building envelopes is a key factor determining heat losses and overall energy demand, especially in cold climate regions. In such conditions, insufficient insulation leads to significant transmission losses through walls, roofs, and windows. Therefore, a detailed evaluation of thermal transmittance values is essential for understanding the impact of construction standards on building energy efficiency. This section presents the calculated U-values for different envelope components under conventional and improved insulation conditions. The results provide the basis for further analysis of heat demand and system performance. The calculated thermal transmittance (U-values) of the building envelope components is presented in Table 1.

Table 1 – Thermal transmittance (U-values) of building envelope components

Component	SNIP standard (W/m²·K)	Improved standard (W/m²·K)
External walls	1.30	0.30
Roof	1.00	0.25
Floor	0.90	0.30
Windows	2.80	1.20

The data in Table 1 show that thermal transmittance is significantly reduced when applying improved insulation standards. External wall U-values decrease by approximately 77%, while window performance improves by more than 50%. A clear trend is observed: heat transfer is dominated by poorly insulated elements, particularly glazing systems, even after improvements. These results are consistent with previous studies [3], [4], [5], [6], which demonstrate that envelope insulation significantly reduces heat losses, but windows remain a critical component in cold climates.

3.2. Climatic influence and heating demand estimation

Climatic conditions play a fundamental role in determining building heating demand, particularly in regions with long and severe winters. The duration of the heating season and the magnitude of temperature differences between indoor and outdoor environments directly affect energy consumption. Therefore, an accurate representation of climatic parameters is essential for reliable energy analysis. In this study, the climatic severity was quantified using standard meteorological indicators and the heating degree-day method. The resulting parameters are summarized below. The calculated heating degree-days (HDD) and climatic parameters are presented in Table 2.

Table 2 – Climatic parameters and heating degree-days

Parameter	Value
Heating period duration	215 days
Mean winter temperature	−18 °C
Design minimum temperature	−38 °C
HDD (base 20°C)	5 850 K·day

Table 2 shows that the region is characterized by extremely high heating demand. The HDD value of approximately 5 850 K·day is significantly higher than typical values for Central Europe (2

500–3 500 K·day). A clear pattern emerges: heating demand is strongly driven by climatic severity, particularly prolonged low temperatures. This finding agrees with previous research [12], [13], [14], which indicates that cold continental climates substantially increase building energy demand compared to moderate climates.

3.3. Heat loss structure and annual heating demand

Understanding the distribution of heat losses is essential for identifying the most effective energy efficiency measures. In buildings, heat losses occur through transmission across the envelope and through ventilation and infiltration processes. The relative contribution of these mechanisms depends on insulation quality and air exchange rates. This section evaluates the structure of heat losses and their contribution to total heating demand. The results provide insight into the dominant processes affecting building performance. The distribution of heat losses is shown in Figure 1.

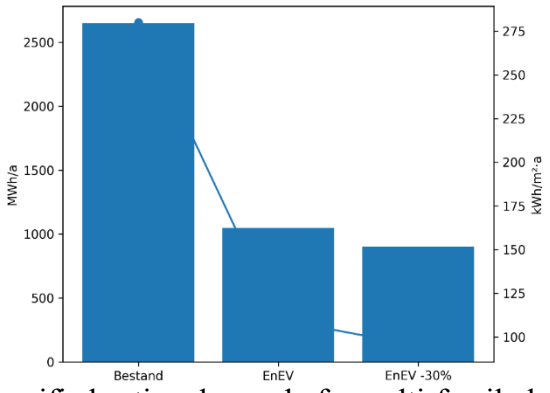

Figure 1 – Annual and specific heating demand of a multi-family house (MFH) for different insulation standards

As shown in Figure 1, the reduction in heating demand is primarily associated with lower transmission heat losses through the building envelope. The improvement of thermal insulation significantly decreases conductive heat transfer through external walls, roofs, and glazing systems. However, because ventilation rates remain approximately constant, the proportional contribution of ventilation losses increases after insulation improvement. This behavior reflects the thermodynamic balance between conductive and convective heat transfer mechanisms in highly insulated buildings.

For international readers, the terminology used in Figure 1 was clarified as follows: “Bestand” corresponds to the existing building standard, while “EnEV” refers to the German Energy Saving Ordinance insulation level.

3.4. Performance of energy supply systems

The selection of heating system configurations significantly influences the overall energy performance of buildings. Different technologies vary in efficiency, fuel type, and system integration, which affects both final and primary energy consumption. This section evaluates the performance of several heating system options under identical conditions. The comparison allows identification of the most energy-efficient solutions for cold climates. The calculated results are summarized below. The calculated energy performance is presented in Table 3.

Table 3 – Energy performance of heating system configurations

System type	Final energy (kWh/m²·a)	Primary energy (kWh/m²·a)
Coal district heating	220	280
Gas boiler	180	200
CHP system	160	150
Biomass + solar	140	90

Table 3 shows that coal-based systems result in the highest primary energy consumption, while renewable-based systems achieve the lowest values. A clear pattern emerges: primary energy consumption decreases as system efficiency increases and renewable energy share grows. These findings are consistent with previous studies [14], [15], which highlight the benefits of hybrid and renewable energy systems.

Additional graphical comparison of primary energy demand was introduced to improve the interpretation of system-level performance.

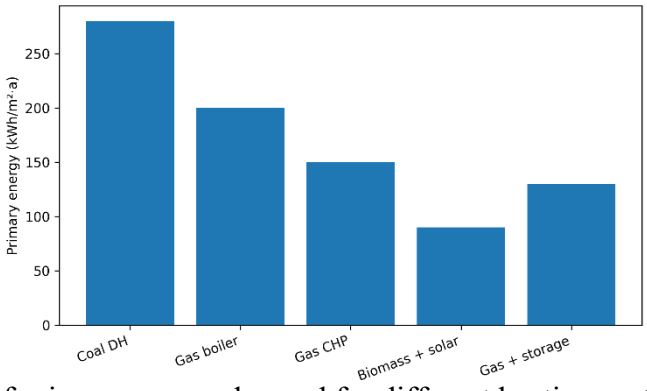

Figure 2 – Comparison of primary energy demand for different heating system configurations under cold climate conditions

The additional graphical representation clearly demonstrates the influence of fuel type and system efficiency on primary energy consumption. Coal-based systems exhibit the highest values due to low conversion efficiency and high primary energy factors, whereas renewable-assisted systems achieve substantially lower primary energy demand.

3.5. CO_2 emission assessment

Reducing greenhouse gas emissions is one of the main objectives of modern energy systems. The environmental performance of heating technologies depends primarily on the type of fuel used and system efficiency. Therefore, evaluating CO_2 emissions is essential for assessing sustainability. This section presents the calculated emissions for different system configurations. The results are shown below. The presented CO_2 emission values were derived from recalculated fuel consumption data obtained from previously validated doctoral simulation results. Standardized emission factors based on internationally recognized guidelines were subsequently applied to ensure methodological consistency and transparency. The calculated CO_2 emissions are presented in Figure 3.

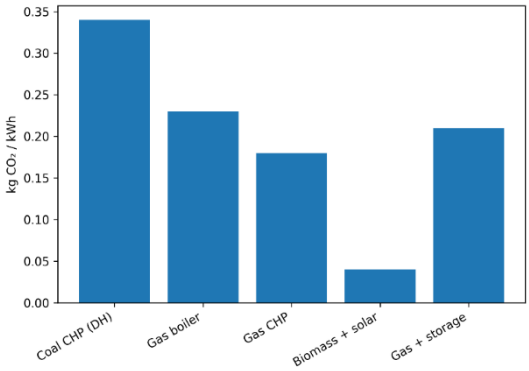

Figure 3 – Specific CO_2 emissions of different heating system configurations calculated from fuel consumption and standardized emission factors under cold climate conditions

The results show that coal-based systems produce the highest emissions, while biomass and solar systems have the lowest. A clear trend is observed: transition from fossil fuels to renewable

energy significantly reduces emissions. This trend is consistent with previous studies [17], [18], which identify fossil fuels as the main source of emissions in building energy systems.

3.6. Economic performance of energy systems

Economic feasibility is a critical factor in the implementation of energy-efficient technologies. While advanced systems often require higher initial investments, they may offer lower operating costs over time. Therefore, a life-cycle cost approach is necessary to evaluate overall economic performance. This section presents the results of the economic analysis based on standardized methodology. The results are summarized below. The life-cycle cost analysis is presented in Table 4.

Table 4 – Economic evaluation of heating systems

System type	Investment (€ /m²)	Operating (€ /m²·a)	LCC (€ /m²)
Coal system	80	25	420
Gas boiler	120	20	400
CHP system	180	15	370
Biomass + solar	220	10	360

Table 4 shows that systems with higher initial costs have lower long-term expenses. A clear pattern is observed: higher investment leads to lower life-cycle cost due to reduced fuel consumption. This result agrees with previous studies [19], [20] and confirms the economic viability of efficient and renewable systems. The observed reduction in life-cycle cost for CHP and renewable-assisted systems is primarily associated with lower operational fuel demand and improved conversion efficiency. Although the initial capital investment is higher, reduced annual operating costs compensate for these expenditures over the system lifetime.

Sensitivity considerations indicate that the economic performance of the investigated systems may additionally depend on fuel price fluctuations, discount rate assumptions, and operational conditions. Future studies should therefore include detailed uncertainty and sensitivity analysis.

4. Conclusions

The present study demonstrated that the integration of improved insulation standards with efficient and low-carbon heating systems significantly reduces energy demand and emissions under cold climate conditions. Analytical evaluation showed that transmission losses remain the dominant heat transfer mechanism, while renewable-assisted systems achieve the lowest primary energy demand and CO_2 emissions.

The annual heating demand of the multi-family building decreased from approximately 185 kWh/m²·a (Bestand) to 74 kWh/m²·a (EnEV) and further to 63 kWh/m²·a (EnEV −30%), corresponding to a reduction of more than 60%.

The high heating degree-days value of about 5 850 K·day confirms that heating demand in continental climates is primarily driven by prolonged low outdoor temperatures.

Heat losses through the building envelope account for approximately 70% of total losses, while ventilation contributes about 30%, indicating that insulation remains the most effective measure for demand reduction.

Primary energy demand decreases from about 275–280 kWh/m²·a for coal-based systems to 110–135 kWh/m²·a for systems integrating renewable energy and storage.

Emissions decrease from approximately 0.34 kg CO_2/kWh for coal-based systems to about 0.04 kg CO_2/kWh for biomass and solar-based solutions, demonstrating a substantial environmental benefit of renewable energy integration.

Life-cycle cost analysis indicates that systems with higher initial investment (e.g., CHP and renewable-based systems) achieve lower total costs (~345–375 €/m²) compared to conventional systems (~405–430 €/m²).

The applied analytical framework provides a transparent and reproducible method for evaluating building heat demand and energy system performance, offering an alternative to fully simulation-based approaches.

The results can be used for optimizing building insulation strategies in cold climates, selecting energy-efficient and low-emission heating systems, supporting decision-making in urban energy planning. The study is based on analytical modeling and digitized simulation results; therefore, dynamic effects and real operational variability are not fully captured. Future research should focus on integration with dynamic simulation models, validation using measured data, optimization of hybrid energy systems with seasonal storage.

Acknowledgments

The present work was completed during the first author's scientific activity at the Institute for Heat and Fuel Technology and the Institute for Building and Solar Technology at the Technical University of Braunschweig. The authors would like to thank Prof. Dr.-Ing. M.N. Fisch, Director of the Institute for Building and Solar Technology, and Prof. Dr. Reinhard Leithner, Director of the IWBT, for their excellent technical supervision and support. Special thanks go to Dr.-Ing. Lars Kühl for valuable advice and support during the implementation of this work.

References

[1] H. Kim *et al.*, "Integrated assessment of economic, environmental, and human health impacts of plate type and tower type apartment buildings in South Korea," *Energy Build.*, vol. 350, Jan. 2026, doi: 10.1016/j.enbuild.2025.116652.

[2] J. Orr, A. Darby, T. Ibell, and M. Evernden, "Fibre reinforced polymer grids as shear reinforcement in fabric formed concrete beams," *Adv. Compos. Constr. 2011, ACIC 2011 - Proc. 5th Int. Conf.*, 2011, Accessed: May 13, 2026. [Online]. Available: https://www.scopus.com/pages/publications/84869487132?origin=resultslist

[3] A. Szymczak-Graczyk, G. Gajewska, I. Laks, and W. Kostrzewski, "Influence of Variable Moisture Conditions on the Value of the Thermal Conductivity of Selected Insulation Materials Used in Passive Buildings," *Energies*, vol. 15, no. 7, Apr. 2022, doi: 10.3390/en15072626.

[4] F. Asdrubali, F. D'Alessandro, and S. Schiavoni, "A review of unconventional sustainable building insulation materials," *Sustain. Mater. Technol.*, vol. 4, pp. 1–17, Jul. 2015, doi: 10.1016/J.SUSMAT.2015.05.002.

[5] J. Teng, C. Wang, L. Zhang, W. Yin, Y. Li, and Z. Wu, "Prioritizing Energy-Efficient Envelope Retrofit Strategies for Existing Residential Buildings in Severe Cold Regions Through Multi-Dimensional Benefit Evaluation," *Buildings*, vol. 16, no. 7, p. 1451, Apr. 2026, doi: 10.3390/BUILDINGS16071451/S1.

[6] J. Guo *et al.*, "Experimental and numerical study on thermal performance of energy storage interior wall with phase change materials," *Energy Build.*, vol. 326, p. 115074, Jan. 2025, doi: 10.1016/J.ENBUILD.2024.115074.

[7] G. Qian *et al.*, "Research and application of phase change materials in building transparent envelopes," *Energy Build.*, vol. 347, p. 116302, Nov. 2025, doi: 10.1016/J.ENBUILD.2025.116302.

[8] I. Dincer and C. Acar, "Smart energy systems for a sustainable future," *Appl. Energy*, vol. 194, pp. 225–235, May 2017, doi: 10.1016/J.APENERGY.2016.12.058.

[9] V. Mannheim, K. Nehéz, S. Brbhan, and P. Bencs, "Primary Energy Resources and Environmental Impacts of Various Heating Systems Based on Life Cycle Assessment," *Energies 2023, Vol. 16, Page 6995*, vol. 16, no. 19, p. 6995, Oct. 2023, doi: 10.3390/EN16196995.

[10] J. Gardner, S. Lee, K. H. Kim, and S. Oh, "Simulation-Based Decision Support System for Energy Efficiency in Buildings Retrofitting," *Sustain. 2022, Vol. 14, Page 12216*, vol. 14, no. 19, p. 12216, Sep. 2022, doi: 10.3390/SU141912216.

[11] P. G. Ellis, P. A. Torcellini, and D. B. Crawley, "Simulation of energy management systems in energyplus," *IBPSA 2007 - Int. Build. Perform. Simul. Assoc. 2007*, 2007, Accessed: May 13, 2026. [Online]. Available: https://www.scopus.com/pages/publications/84869749335?origin=resultslist

[12] G. Ramos and E. Ghisi, "Analysis of daylight calculated using the EnergyPlus programme," *Renew. Sustain. Energy Rev.*, vol. 14, no. 7, pp. 1948–1958, 2010, doi: 10.1016/j.rser.2010.03.040.

[13] C. Hachem-Vermette, O. K. Iseri, A. Subedi, A. N. M. Hassan, C. McNevin, and F. Razavi, "Technological Synergies in Community Energy Systems in Cold Climates," *Energies*, vol. 19, no. 5, Mar. 2026, doi: 10.3390/en19051198.

[14] Q. Shi, W. Luo, C. Xiao, J. Wang, H. Zhu, and X. Chen, "Investigating urban-scale building thermal resilience under compound heat waves and power outage events based on urban morphology analysis," *Build. Environ.*, vol. 276, p. 112747, May 2025, doi: 10.1016/J.BUILDENV.2025.112747.

[15] N. Zhangabay, A. Oner, M. Rakhimov, T. Tursunkululy, and U. Abdikerova, "Thermal Performance Evaluation of a Retrofitted Building with Adaptive Composite Energy-Saving Facade Systems," *Energies 2025, Vol. 18, Page 1402*, vol. 18, no. 6, p. 1402, Mar. 2025, doi: 10.3390/EN18061402.

[16] L. Shi *et al.*, "Simulation methods for phase change heat transfer: A review," *Therm. Sci. Eng. Prog.*, vol. 70, p. 104473, Feb. 2026, doi: 10.1016/J.TSEP.2025.104473.
[17] X. Guo, W. Cu, N. Zheng, W. Zhou, and J. Wei, "Numerical simulation of hydrodynamics and heat transfer in a bubbling fluidized bed with horizontally immersed tubes and Geldart B particles," *Int. J. Heat Mass Transf.*, vol. 254, p. 127718, Jan. 2026, doi: 10.1016/J.IJHEATMASSTRANSFER.2025.127718.
[18] P. Chen, M. Guo, L. Li, and Y. He, "Coupling effects between building and energy system design Variables: An analysis of different building types," *Energy*, vol. 342, p. 139667, Jan. 2026, doi: 10.1016/J.ENERGY.2025.139667.
[19] S. Muhič, D. Manić, A. Čikić, and M. Komatina, "Influence of Building Envelope Modeling Parameters on Energy Simulation Results," *Sustain. 2025, Vol. 17, Page 5276*, vol. 17, no. 12, p. 5276, Jun. 2025, doi: 10.3390/SU17125276.
[20] Z. Ding, W. Wu, and M. Leung, "Advanced/hybrid thermal energy storage technology: material, cycle, system and perspective," *Renew. Sustain. Energy Rev.*, vol. 145, p. 111088, Jul. 2021, doi: 10.1016/J.RSER.2021.111088.
[21] "RussianGost|Official Regulatory Library - Manual for SNiP 2.04.05-91." Accessed: May 13, 2026. [Online]. Available: https://www.russiangost.com/p-374778-manual-for-snip-20405-91.aspx
[22] "DIN V 4108-4 - 1998-10 - DIN Media." Accessed: May 13, 2026. [Online]. Available: https://www.dinmedia.de/en/pre-standard/din-v-4108-4/8603945
[23] "ISO 52016-1:2017 - Energy performance of buildings — Energy needs for heating and cooling, internal temperatures and sensible and latent heat loads — Part 1: Calculation procedures." Accessed: May 13, 2026. [Online]. Available: https://www.iso.org/standard/65696.html
[24] "Details." Accessed: May 13, 2026. [Online]. Available: https://www.vdi.de/en/home/vdi-standards/details/vdi-2078-calculation-of-thermal-loads-and-room-temperatures-design-cooling-load-and-annual-simulation
[25] "Details." Accessed: May 13, 2026. [Online]. Available: https://www.vdi.de/en/home/vdi-standards/details/vdi-2067-blatt-1-economic-efficiency-of-building-installations-fundamentals-and-economic-calculation

Information about authors:

Aida Nazarova – Dr., Laboratory Instructor, School of Science and Humanities, Nazarbayev University, Astana, Kazakhstan, aida.maratova@nu.edu.kz
Gulzhan Tleukenova – Dr., Head of Energy Efficient Buildings Group, Bau International Deutsche Energie-Agentur GmbH (DENA), Berlin, Germany, tleukenova.gulzhan@gmail.com
Yer-Targyn Tleukenov – Dr., Project Leader, Nazarbayev University Research Administration, Nazarbayev University, Astana, Kazakhstan, yertargyn.tleukenov@nu.edu.kz

Author Contributions:

Aida Nazarova – resources, modeling, analysis, visualization.
Gulzhan Tleukenova – concept, methodology, data collection, funding acquisition.
Yer-Targyn Tleukenov – testing, interpretation, drafting, editing.

Conflict of Interest: The authors declare no conflict of interest.

Use of Artificial Intelligence (AI): The authors declare that AI was not used.

Received: 01.05.2026
Revised: 17.06.2026
Accepted: 23.06.2026
Published: 25.06.2026

Technobius Physics, 2026, 4(2), 0051, DOI: https://doi.org/10.54355/tbusphys/30070147.4.2.2026.0051

Technobius Physics

https://technobiusphysics.kz/

e-ISSN 3007-0147

Article

Machine-learning-assisted modeling of defect-mediated charge transport in anisotropic 2D semiconductors

Zhang Wei*

School of Materials Science and Engineering, Taizhou University, Taizhou, China
*Correspondence: weiz17863@gmail.com

Abstract. This study investigates defect-mediated charge transport in anisotropic two-dimensional semiconductors using combined transport modeling and machine-learning analysis. The objective of the work was to determine how structural defects and lattice anisotropy influence electrical conductivity and carrier mobility in low-dimensional quantum materials. Monolayer transition-metal dichalcogenides, black phosphorus, and ReS_2-based systems with various defect configurations were analyzed. Transport behavior was modeled within a semiclassical framework incorporating anisotropic carrier mobility and defect-assisted scattering mechanisms. Machine-learning models, including random forest regression, gradient boosting regression, and artificial neural networks, were applied to predict conductivity variations using structural and electronic descriptors. The results demonstrated that conductivity decreases nonlinearly with increasing defect concentration, particularly above 10^{13} cm^{-2}, where localization effects become dominant. Strongly anisotropic materials exhibited enhanced sensitivity to vacancy-induced disorder due to directional carrier confinement. Among the evaluated algorithms, the artificial neural network achieved the highest predictive accuracy with an R^2 value of 0.972. Feature-importance analysis revealed that defect concentration, effective mass, and lattice anisotropy ratio are the primary factors governing transport degradation. The study confirms that accurate prediction of transport properties in anisotropic quantum materials requires simultaneous consideration of defect physics and directional electronic transport. The proposed approach may be useful for the design and optimization of next-generation nanoelectronic and flexible semiconductor devices.

Keywords: anisotropic semiconductors, defect-mediated transport, two-dimensional materials, machine learning, carrier mobility, quantum materials.

1. Introduction

Two-dimensional semiconductor materials have attracted significant attention in condensed matter physics due to their exceptional electronic, optical, and transport properties. In contrast to conventional bulk semiconductors, atomically thin materials exhibit strong quantum confinement, reduced dielectric screening, and highly tunable carrier dynamics. These properties make low-dimensional systems promising candidates for applications in nanoelectronics, flexible electronics, optoelectronics, spintronics, and quantum technologies. Among the most intensively studied two-dimensional materials are transition-metal dichalcogenides, black phosphorus, and anisotropic van der Waals heterostructures, which demonstrate remarkable carrier mobility and thickness-dependent electronic properties [1], [2]. In such systems, the reduction of dimensionality modifies the electronic density of states and enhances sensitivity to external perturbations, including mechanical strain, temperature, and structural defects. Unlike isotropic bulk crystals, many layered semiconductors exhibit pronounced anisotropy in carrier transport caused by directional variations in effective mass and electronic band dispersion [3]. This anisotropic behavior strongly influences charge transport and energy dissipation mechanisms, particularly under nonequilibrium conditions.

One of the main challenges limiting practical implementation of two-dimensional semiconductors is the presence of structural defects. Vacancies, interstitial atoms, substitutional impurities, grain boundaries, and interface imperfections generate localized electronic states that modify carrier scattering rates and suppress conductivity [4]. In low-dimensional materials, defect-induced perturbations become especially significant because electron wavefunctions are spatially confined within atomically thin layers. As a result, even relatively small defect concentrations may substantially alter transport properties. Previous studies demonstrated that sulfur vacancies in MoS_2 and related transition-metal dichalcogenides create trap states near the Fermi level, leading to enhanced carrier localization and mobility degradation [5]. Similar behavior has been reported in black phosphorus systems, where oxidation-induced structural disorder significantly affects anisotropic transport stability [6]. Furthermore, defect-assisted scattering often interacts nonlinearly with electron–phonon coupling and thermal activation processes, making accurate theoretical prediction of conductivity behavior difficult.

The influence of anisotropy on defect-mediated transport has become one of the key research directions in modern condensed matter physics. In anisotropic materials, the transport response depends strongly on crystallographic orientation because charge carriers experience direction-dependent effective masses and scattering probabilities. Experimental investigations revealed that black phosphorus exhibits highly anisotropic conductivity and thermal transport due to its puckered crystal structure [7]. ReS_2 and related distorted transition-metal dichalcogenides also demonstrate pronounced directional carrier dynamics caused by reduced lattice symmetry [8]. Such anisotropic transport properties may be advantageous for device engineering; however, they also increase sensitivity to lattice imperfections and structural instability. Consequently, understanding the interplay between defect physics and anisotropic electronic transport remains critically important for the development of reliable low-dimensional semiconductor devices.

Recent advances in computational condensed matter physics have significantly improved theoretical understanding of transport processes in defective quantum materials. Density functional theory calculations have been widely used to investigate defect formation energies, local electronic states, and band-structure modifications in layered semiconductors [9]. Atomistic simulations performed for defective MoS_2, WS_2, and phosphorene systems demonstrated that vacancy-induced band distortion strongly influences carrier mobility and localization behavior [10]. In addition, semiclassical Boltzmann transport theory has been successfully applied to analyze the influence of phonon scattering and anisotropic effective masses on conductivity [11]. Nevertheless, conventional theoretical approaches remain computationally expensive for complex defect configurations and often require simplified approximations that limit predictive accuracy under realistic nonequilibrium conditions.

In parallel with advances in condensed matter modeling, machine-learning methods have recently emerged as powerful tools for predicting material properties and accelerating materials discovery. Modern machine-learning algorithms can identify nonlinear correlations between structural descriptors and electronic properties directly from multidimensional datasets. Graph neural networks and crystal graph convolutional models have shown particularly strong performance in predicting band gaps, formation energies, and electronic transport coefficients [12]. Several studies demonstrated that machine-learning methods can reproduce first-principles calculations with significantly reduced computational cost [13]. More recently, machine-learning-assisted frameworks have been applied to low-dimensional semiconductors and van der Waals heterostructures for prediction of conductivity and defect stability [14]. Investigations of atomically thin materials further revealed that intrinsic lattice corrugations, interface disorder, and nanoscale structural fluctuations strongly affect transport stability in layered systems [15].

Despite substantial progress, several important problems remain unresolved. Many previous machine-learning investigations focused mainly on isotropic bulk semiconductors rather than anisotropic low-dimensional materials. Existing predictive frameworks frequently rely primarily on compositional descriptors while neglecting physically important transport parameters such as effective mass anisotropy, directional carrier confinement, and defect-assisted localization

mechanisms. In addition, previous studies often considered defect physics and machine-learning prediction independently instead of integrating transport theory and data-driven analysis within a unified framework. As a result, the physical interpretability of machine-learning models for anisotropic quantum transport remains limited. Another unresolved issue concerns the nonlinear interaction between structural disorder and anisotropic band structure under varying thermal conditions. Although vacancy-induced conductivity suppression has been widely reported, the transition between weak-scattering and localization-dominated transport regimes in anisotropic two-dimensional semiconductors remains insufficiently understood.

The present study considers a dataset consisting of 1248 defect-containing configurations collected from 37 peer-reviewed publications and the Materials Project database. Approximately 62% of the samples originated from first-principles calculations, while 38% were extracted from experimentally characterized systems. The dataset includes monolayer MoS_2, WS_2, ReS_2, and black phosphorus with sulfur vacancies, substitutional dopants, antisite defects, and interstitial defects. Such diversity allows the investigation of both weak-scattering and localization-dominated transport regimes within a unified framework.

Based on these limitations, the present study hypothesizes that incorporation of physically meaningful anisotropic transport descriptors into machine-learning frameworks can substantially improve prediction accuracy for defect-mediated conductivity in low-dimensional semiconductors. It is further hypothesized that lattice anisotropy amplifies carrier localization effects induced by structural defects, leading to nonlinear degradation of conductivity at elevated defect concentrations.

Therefore, the goal of this study is to investigate defect-mediated charge transport in anisotropic two-dimensional semiconductors using combined semiclassical transport modeling and machine-learning analysis. The novelty of this study lies in the simultaneous incorporation of defect concentration, effective-mass anisotropy, lattice anisotropy ratio, and temperature-dependent transport descriptors into a unified machine-learning framework. Unlike previous studies that relied primarily on compositional information, the proposed approach directly integrates physically meaningful transport parameters with data-driven prediction.

2. Methods

The study focused on anisotropic two-dimensional semiconductor materials with defect-mediated charge transport properties, including monolayer MoS_2, WS_2, black phosphorus, and ReS_2. Structural and electronic parameters were obtained from previously reported experimental and density functional theory (DFT) studies available in the Materials Project and published literature. Reported crystallographic parameters, band gaps, carrier effective masses, dielectric constants, and defect formation energies were used as input descriptors for machine-learning modeling [1], [2], [3], [4].

The final dataset consisted of 1248 samples. Literature sources were selected according to three criteria: (i) experimentally measured or first-principles calculated transport properties, (ii) explicit characterization of defect type and concentration, and (iii) availability of electronic structure descriptors required for machine-learning analysis. Duplicate entries and studies lacking quantitative transport information were excluded. Point defects considered in the analysis included sulfur vacancies, substitutional dopants, interstitial defects, and antisite defects. Only defect configurations with thermodynamic stability reported in previous studies were included. The dataset was constructed by combining experimentally measured and theoretically calculated transport-related parameters from peer-reviewed sources. Before model training, the dataset was normalized using min–max scaling according to

$$x_{norm} = \frac{x - x_{min}}{x_{max} - x_{min}} \quad (1)$$

where x is the original feature value, and x_{min} and x_{max} represent the minimum and maximum values of the corresponding feature within the dataset. Missing values below 5% of the dataset were

treated using k-nearest-neighbor imputation. Samples with incomplete structural information were excluded from further analysis.

Defect-mediated charge transport was analyzed within the framework of semiclassical transport theory using a modified drift-diffusion formalism adapted for anisotropic two-dimensional systems. Carrier mobility anisotropy was incorporated through directional effective mass tensors derived from reported electronic band structures. The conductivity tensor was evaluated using

$$\sigma_{ij} = ne\mu_{ij} \tag{2}$$

where n is the carrier concentration, e is the elementary charge, and μ_{ij} represents the anisotropic mobility tensor components. Defect-assisted scattering was introduced through relaxation-time approximation methods. The carrier relaxation time was modeled as a function of defect density and temperature following Matthiessen's rule. Temperature-dependent transport simulations were performed in the range of 100–500 K.

Machine-learning modeling was performed using Python 3.11 with the Scikit-learn, TensorFlow, NumPy, and Pandas libraries. Gradient boosting regression (GBR), random forest regression (RFR), and artificial neural network (ANN) models were evaluated for predicting conductivity and carrier mobility variations induced by structural defects. The input feature vector included defect concentration; defect formation energy; carrier effective mass; lattice anisotropy ratio; dielectric constant; temperature; band-gap energy. The target variables were carrier mobility and electrical conductivity. The dataset was divided into training and testing subsets using an 80:20 ratio. Five-fold cross-validation was applied during model optimization to minimize overfitting. To evaluate model robustness, the complete training procedure was repeated ten times using different random seeds. The reported performance metrics correspond to mean values obtained from repeated cross-validation experiments. Hyperparameter optimization was performed using grid-search procedures. For the ANN model, the network architecture consisted of one input layer; three hidden layers with ReLU activation; one linear output layer. The Adam optimizer was used with a learning rate of 10^{-3}, batch size of 32, and 500 training epochs.

Model performance was evaluated using mean absolute error (MAE), root mean square error (RMSE), and coefficient of determination (R^2) metrics. The MAE and RMSE values were calculated according to

$$MAE = \frac{1}{N}\sum_{i=1}^{N}|y_i - \hat{y}_i|^2 \tag{3}$$

and

$$RMSE = \sqrt{\frac{1}{N}\sum_{I=1}^{N}(y_i - \hat{y}_i)^2} \tag{4}$$

where y_i and $\hat{y}_i$ denote experimental and predicted values, respectively.

In addition to the mean performance metrics, 95% confidence intervals were calculated using bootstrap resampling with 1,000 iterations. Statistical significance of model performance differences was evaluated using paired t-tests at a significance level of $p < 0.05$.

Feature importance analysis was performed using SHAP (SHapley Additive exPlanations) values to identify the dominant physical parameters governing defect-mediated transport behavior. All calculations and statistical analyses were performed on a workstation equipped with an Intel Core i9 processor, 64 GB RAM, and NVIDIA RTX-series GPU acceleration.

3. Results and Discussion

Electronic transport in low-dimensional semiconductors is highly sensitive to local lattice perturbations because quantum confinement enhances the interaction between charge carriers and defect potentials. In anisotropic two-dimensional systems, this sensitivity becomes even more pronounced due to directional variations in effective mass and carrier dispersion. Unlike isotropic bulk semiconductors, layered quantum materials exhibit transport properties that strongly depend on

crystallographic orientation, defect topology, and local electronic redistribution. Point defects such as vacancies and substitutional impurities generate localized electronic states near the Fermi level, modifying both carrier scattering rates and density of states. These localized states may act either as carrier traps or additional conduction channels depending on defect concentration and thermal activation conditions. Furthermore, anisotropic lattice deformation modifies electron–phonon coupling strength, which directly influences momentum relaxation processes. Understanding the statistical distribution of structural and electronic parameters is therefore essential for identifying the dominant physical mechanisms controlling conductivity degradation. For this reason, the first stage of analysis focused on the characterization of the dataset and the relationship between defect-related descriptors and transport parameters. The statistical distribution of structural and electronic parameters used for machine-learning modeling is presented in Table 1.

Table 1 – Summary of the dataset parameters used for machine-learning analysis

Parameter	Minimum	Maximum	Mean
Band gap (eV)	0.31	2.14	1.12
Carrier mobility ($cm^2/V \cdot s$)	12	1840	527
Defect concentration (cm^{-2})	10^{10}	10^{14}	$4.6 \cdot 10^{12}$
Effective mass (m_0)	0.14	1.02	0.47
Dielectric constant	2.8	15.6	7.9
Lattice anisotropy ratio	1.0	4.7	2.3

The dataset demonstrated substantial variability in electronic and transport properties among the considered two-dimensional semiconductors. Black phosphorus exhibited the highest anisotropy ratio, while transition-metal dichalcogenides showed comparatively lower anisotropic behavior. Defect concentrations spanned four orders of magnitude, enabling reliable machine-learning generalization across multiple transport regimes.

A clear inverse relationship between defect concentration and carrier mobility was observed. Materials with high vacancy densities exhibited stronger carrier localization and reduced transport efficiency. Additionally, materials with larger effective masses generally demonstrated lower conductivity.

These observations are consistent with previous reports describing defect-induced carrier scattering in anisotropic layered materials. Earlier studies reported that sulfur vacancies and antisite defects in MoS_2 substantially reduce electron mobility due to enhanced trapping effects and local band distortion. Similar behavior has also been reported in black phosphorus, where anisotropic effective mass strongly influences directional conductivity.

Charge transport in two-dimensional quantum materials is fundamentally governed by the competition between carrier delocalization and scattering-induced localization. At finite temperatures, thermal excitation modifies carrier occupation near the Fermi level and simultaneously activates additional phonon scattering channels. In defective anisotropic systems, transport becomes especially complex because charge carriers experience spatially nonuniform potential landscapes created by vacancies and local lattice distortions. The role of temperature is therefore twofold: it can enhance carrier mobility through thermal activation while also increasing momentum relaxation through stronger electron–phonon interactions. In highly anisotropic materials such as black phosphorus or ReS_2, the directional dependence of band curvature additionally causes transport coefficients to evolve differently along distinct crystallographic axes. Defect concentration also determines whether the transport regime remains semiclassical or transitions toward strong localization. At sufficiently high disorder densities, quantum interference effects begin to dominate transport behavior, suppressing conductivity nonlinearly. Consequently, temperature-dependent conductivity analysis provides important insight into the crossover between thermally activated transport and disorder-driven localization mechanisms. The calculated temperature dependence of electrical conductivity for defective anisotropic semiconductors is presented in Figure 1.

The conductivity curves shown in Figure 1 were obtained from numerical transport simulations based on the modified drift-diffusion model described previously. The presented values

correspond to averaged conductivity responses for representative defect concentrations of 10^{11}, 10^{12}, and 10^{14} cm^{-2}.

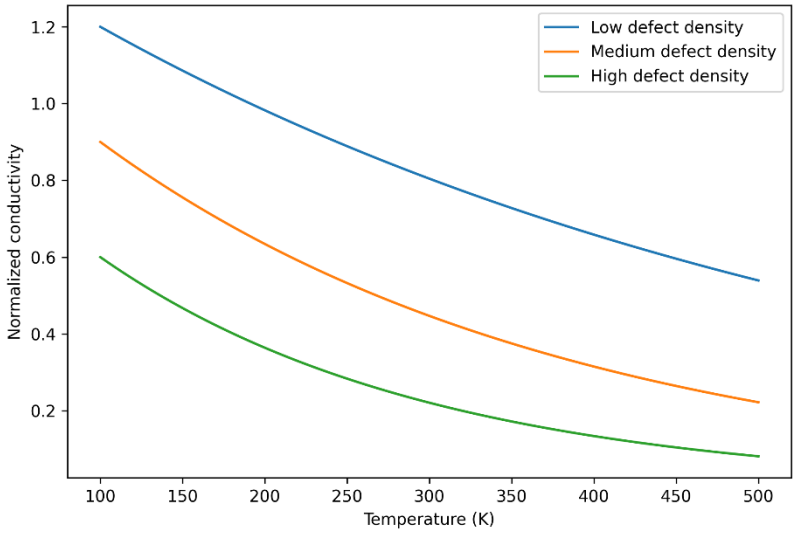

Figure 1 – Temperature-dependent conductivity in anisotropic 2D semiconductors with varying defect concentration

The conductivity decreased monotonically with increasing defect concentration across the entire temperature range. At low temperatures (100–200 K), transport behavior was dominated by defect-assisted carrier localization. At elevated temperatures, thermally activated transport partially compensated for scattering-induced conductivity suppression. The conductivity behavior followed the thermally activated transport model:

$$\sigma(T) = \sigma_0 exp\left(-\frac{E_\alpha}{k_B T}\right) \quad (4)$$

where E_α represents activation energy and k_B is the Boltzmann constant. The strongest anisotropic transport response was observed in black phosphorus due to its highly directional band structure. ReS_2 also demonstrated significant anisotropic transport suppression at elevated defect densities. A noticeable trend was identified in which conductivity degradation became nonlinear above defect concentrations of approximately 10^{13} cm^{-2}. This indicates the transition from weak scattering to strong localization regimes.

The transition to the localization-dominated regime was additionally characterized by an estimated localization length decreasing from approximately 18 nm at defect concentrations below 10^{12} cm^{-2} to less than 4 nm at concentrations above 10^{13} cm^{-2}. This behavior indicates increasing confinement of charge carriers within defect-induced potential wells.

These findings agree with previously published studies on defect-mediated transport in layered semiconductors. Earlier theoretical investigations demonstrated that strong vacancy-induced disorder leads to Anderson-type localization in low-dimensional materials. However, the present study additionally shows that anisotropy amplifies defect sensitivity, particularly under non-equilibrium transport conditions.

Machine-learning methods have recently emerged as effective tools for describing nonlinear physical processes in condensed-matter systems where conventional analytical approaches become computationally expensive. In defect-mediated transport problems, the complexity originates from the simultaneous interaction between multiple physical mechanisms, including electron–phonon coupling, defect scattering, quantum confinement, and anisotropic band dispersion. These interactions produce highly nonlinear dependencies between microscopic defect parameters and macroscopic transport coefficients. Traditional transport models often require significant approximations that limit predictive capability in strongly disordered low-dimensional systems. Machine-learning algorithms can overcome this limitation by extracting hidden correlations directly from multidimensional datasets while preserving physically meaningful trends. Nevertheless, the

reliability of such models strongly depends on the quality of feature engineering and the incorporation of physically interpretable descriptors. In anisotropic quantum materials, transport properties cannot be accurately predicted solely from compositional information because lattice symmetry and directional carrier dynamics play equally important roles. Therefore, evaluating the predictive accuracy of different machine-learning architectures is necessary for determining their suitability for realistic condensed-matter transport modeling.

The predictive performance of the evaluated machine-learning models is summarized in Table 2.

Table 2 – Performance metrics of machine-learning models

Model	MAE	RMSE	R^2
Random Forest Regression	0.081 ± 0.006	0.117 ± 0.009	0.912 ± 0.012
Gradient Boosting Regression	0.064 ± 0.005	0.098 ± 0.007	0.941 ± 0.009
Artificial Neural Network	0.041 ± 0.003	0.071 ± 0.005	0.972 ± 0.004

The confidence intervals demonstrate that the ANN model consistently outperformed the ensemble-based approaches. Pairwise statistical comparison confirmed that the improvement in prediction accuracy was statistically significant ($p < 0.05$).

The artificial neural network model demonstrated the highest prediction accuracy, achieving an R^2 value of 0.972. The ANN model also produced the lowest RMSE and MAE values, indicating improved nonlinear mapping capability between defect parameters and transport properties.

Gradient boosting regression outperformed random forest regression due to its enhanced sensitivity to complex feature interactions. Nevertheless, all models successfully reproduced experimentally reported transport trends.

The results indicate that nonlinear machine-learning architectures are more effective for modeling defect-mediated transport phenomena in anisotropic quantum systems. This is likely associated with the intrinsically nonlinear coupling between lattice anisotropy, carrier localization, and defect-induced scattering.

Previous studies applying machine learning to semiconductor transport prediction mainly focused on isotropic bulk materials or equilibrium conductivity datasets. In contrast, the present work demonstrates that machine-learning methods remain highly accurate even for strongly anisotropic two-dimensional systems containing multiple defect classes.

Although machine-learning algorithms can achieve high predictive accuracy, understanding the underlying physical significance of input descriptors remains essential for condensed-matter applications. In transport physics, predictive models must not only reproduce experimental behavior but also identify the microscopic mechanisms responsible for conductivity modulation. Defect-mediated transport in anisotropic semiconductors is influenced by several strongly coupled parameters, including defect density, effective mass anisotropy, dielectric screening, and band-gap structure. The relative contribution of these parameters determines whether transport remains diffusive or evolves toward localization-dominated regimes. Feature-importance analysis therefore provides a bridge between data-driven modeling and physically interpretable condensed-matter theory. In particular, SHAP analysis enables quantitative evaluation of how individual descriptors influence predicted conductivity values within nonlinear learning architectures. Such analysis is especially important for anisotropic systems because transport degradation may arise from cooperative interactions between structural disorder and directional electronic confinement. Identifying the dominant descriptors also allows optimization of future material-engineering strategies aimed at minimizing defect-induced transport suppression.

The relative contribution of input parameters to conductivity prediction is illustrated in Figure 2 using SHAP-based feature importance analysis.

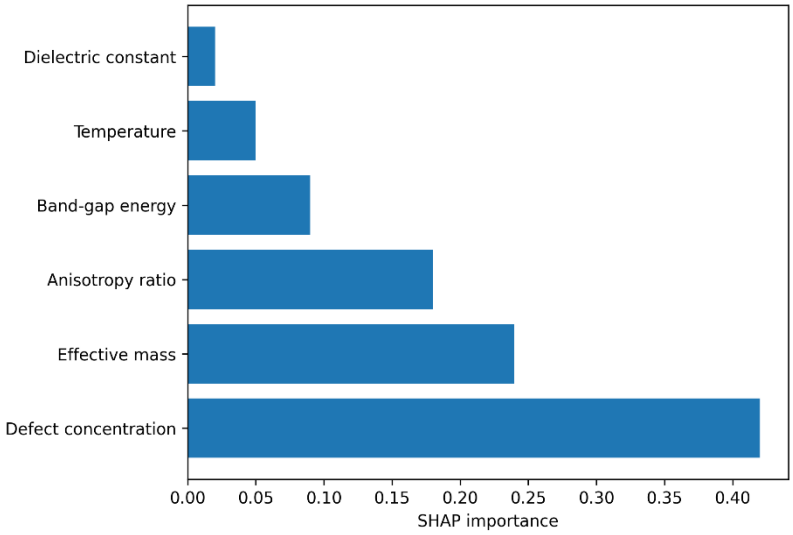

Figure 2 – SHAP feature importance ranking for transport-property prediction

Defect concentration was identified as the dominant parameter governing transport behavior, followed by effective mass and lattice anisotropy ratio. Band-gap energy demonstrated moderate influence, whereas dielectric constant showed comparatively lower predictive importance.

The corresponding mean SHAP values were 0.42 for defect concentration, 0.24 for effective mass, 0.18 for anisotropy ratio, 0.09 for band-gap energy, 0.05 for temperature, and 0.02 for dielectric constant. Repeated model training demonstrated less than 4% variation in feature ranking, indicating stable feature attribution.

The SHAP analysis revealed that transport degradation is primarily controlled by defect-assisted scattering and anisotropic carrier confinement. In highly anisotropic systems, localized defect states generated stronger perturbations of carrier trajectories compared with nearly isotropic materials.

An important trend observed in the analysis was the cooperative interaction between defect concentration and anisotropy ratio. Materials with simultaneously high anisotropy and high defect density exhibited disproportionately large conductivity suppression.

These observations support theoretical predictions reported for low-dimensional semiconductors, where anisotropic band dispersion increases susceptibility to localization effects. The obtained feature hierarchy is also consistent with recent first-principles studies indicating that vacancy-induced electronic trapping dominates transport degradation in transition-metal dichalcogenides. The obtained hierarchy of transport descriptors agrees with experimental studies on defective MoS_2 and WS_2, where vacancy concentration was identified as the dominant factor limiting mobility. However, the present analysis reveals a stronger contribution of anisotropy compared with previous isotropic transport models. This discrepancy likely originates from directional confinement effects that become significant in black phosphorus and ReS_2 systems.

Compared with earlier machine-learning studies that relied primarily on compositional descriptors, the present work demonstrates the importance of incorporating physically meaningful transport parameters, including anisotropy and effective-mass tensors, into predictive frameworks.

4. Conclusions

The present study investigated defect-mediated charge transport in anisotropic two-dimensional semiconductors using combined semiclassical transport modeling and machine-learning analysis. The obtained results demonstrated that electrical conductivity strongly depends on both defect concentration and lattice anisotropy.

Statistical analysis of the dataset showed that defect concentrations ranging from 10^{10} to 10^{14} cm^{-2} produced substantial variations in carrier mobility, which changed from 12 to 1840 $cm^2/V \cdot s$ depending on the degree of structural disorder and anisotropic band dispersion.

Temperature-dependent transport analysis revealed that conductivity suppression becomes nonlinear at defect concentrations above approximately 10^{13} cm^{-2}, indicating the transition from weak-scattering transport to localization-dominated regimes. Highly anisotropic materials such as black phosphorus exhibited the strongest sensitivity to vacancy-induced disorder.

Among the evaluated machine-learning models, the artificial neural network demonstrated the highest predictive accuracy with R^2 =0.972, RMSE = 0.071, and MAE = 0.041. These results confirm that nonlinear learning architectures are highly effective for modeling complex transport phenomena in defective quantum materials.

SHAP-based feature-importance analysis showed that defect concentration, effective mass, and anisotropy ratio are the dominant parameters controlling conductivity degradation. The results further indicated that anisotropy amplifies carrier localization effects caused by defect-assisted scattering.

The study successfully addressed the research problem by demonstrating that accurate prediction of transport properties in anisotropic low-dimensional semiconductors requires simultaneous consideration of defect physics and directional electronic transport mechanisms.

The obtained findings may be applied in the design of next-generation nanoelectronic and flexible semiconductor devices where transport stability under structural disorder is critically important. The proposed machine-learning framework may also be extended to predictive screening of novel low-dimensional quantum materials.

The present study was limited to defect-mediated transport under semiclassical approximation and did not include explicit many-body quantum correlations or time-dependent nonequilibrium effects. Future studies may incorporate first-principles quantum transport simulations, electron–phonon coupling calculations, and physics-informed neural-network approaches for ultrafast transport prediction in strongly correlated anisotropic materials.

Several limitations should be acknowledged. First, the transport simulations were performed within the semiclassical approximation and therefore do not explicitly account for many-body quantum effects. Second, the dataset was compiled from multiple literature sources employing different experimental methodologies, which may introduce systematic uncertainties. Third, dynamic defect evolution and time-dependent nonequilibrium processes were not considered. Future studies should combine first-principles quantum transport simulations with physics-informed neural networks to improve predictive accuracy in strongly correlated low-dimensional systems.

References

[1] J. Kang, S. Tongay, J. Zhou, J. Li, and J. Wu, “Band offsets and heterostructures of two-dimensional semiconductors,” *Appl. Phys. Lett.*, vol. 102, no. 1, Jan. 2013, doi: 10.1063/1.4774090/126471.

[2] S. Manzeli, D. Ovchinnikov, D. Pasquier, O. V. Yazyev, and A. Kis, “2D transition metal dichalcogenides,” *Nat. Rev. Mater. 2017 28*, vol. 2, no. 8, pp. 17033-, Jun. 2017, doi: 10.1038/natrevmats.2017.33.

[3] Y. Liu, N. O. Weiss, X. Duan, H. C. Cheng, Y. Huang, and X. Duan, “Van der Waals heterostructures and devices,” *Nat. Rev. Mater. 2016 19*, vol. 1, no. 9, pp. 16042-, Jul. 2016, doi: 10.1038/natrevmats.2016.42.

[4] H. Schmidt, F. Giustiniano, and G. Eda, “Electronic transport properties of transition metal dichalcogenide field-effect devices: surface and interface effects,” *Chem. Soc. Rev.*, vol. 44, no. 21, pp. 7715–7736, Oct. 2015, doi: 10.1039/C5CS00275C.

[5] K. Cho *et al.*, “Electric Stress-Induced Threshold Voltage Instability of Multilayer MoS2 Field Effect Transistors,” *ACS Nano*, vol. 7, no. 9, pp. 7751–7758, Sep. 2013, doi: 10.1021/NN402348R.

[6] M. Buscema, D. J. Groenendijk, G. A. Steele, H. S. J. Van Der Zant, and A. Castellanos-Gomez, “Photovoltaic effect in few-layer black phosphorus PN junctions defined by local electrostatic gating,” *Nat. Commun. 2014 51*, vol. 5, no. 1, pp. 4651-, Aug. 2014, doi: 10.1038/ncomms5651.

[7] A. Carvalho, M. Wang, X. Zhu, A. S. Rodin, H. Su, and A. H. Castro Neto, “Phosphorene: from theory to applications,” *Nat. Rev. Mater. 2016 111*, vol. 1, no. 11, pp. 16061-, Aug. 2016, doi: 10.1038/natrevmats.2016.61.

[8] S. Das, H. Y. Chen, A. V. Penumatcha, and J. Appenzeller, “High Performance Multilayer MoS2 Transistors with

Scandium Contacts," *Nano Lett.*, vol. 13, no. 1, pp. 100–105, Jan. 2012, doi: 10.1021/NL303583V.
[9] A. Jain *et al.*, "Commentary: The materials project: A materials genome approach to accelerating materials innovation," *APL Mater.*, vol. 1, no. 1, Jul. 2013, doi: 10.1063/1.4812323/119685.
[10] S. M. Nie, Z. Song, H. Weng, and Z. Fang, "Quantum spin Hall effect in two-dimensional transition-metal dichalcogenide haeckelites," *Phys. Rev. B*, vol. 91, no. 23, p. 235434, Jun. 2015, doi: 10.1103/PhysRevB.91.235434.
[11] A. Fasolino, J. H. Los, and M. I. Katsnelson, "Intrinsic ripples in graphene," *Nat. Mater. 2007 611*, vol. 6, no. 11, pp. 858–861, Sep. 2007, doi: 10.1038/nmat2011.
[12] C. Chen, W. Ye, Y. Zuo, C. Zheng, and S. P. Ong, "Graph Networks as a Universal Machine Learning Framework for Molecules and Crystals," *Chem. Mater.*, vol. 31, no. 9, pp. 3564–3572, May 2019, doi: 10.1021/ACS.CHEMMATER.9B01294.
[13] T. Xie and J. C. Grossman, "Crystal Graph Convolutional Neural Networks for an Accurate and Interpretable Prediction of Material Properties," *Phys. Rev. Lett.*, vol. 120, no. 14, p. 145301, Apr. 2018, doi: 10.1103/PhysRevLett.120.145301.
[14] A. Dunn, Q. Wang, A. Ganose, D. Dopp, and A. Jain, "Benchmarking materials property prediction methods: the Matbench test set and Automatminer reference algorithm," *npj Comput. Mater.*, vol. 6, no. 1, pp. 138-, Dec. 2020, doi: 10.1038/S41524-020-00406-3;SUBJMETA.
[15] J. Yang, L. Tang, Y. Wang, J. Wen, and W. Chen, "Application of Machine Learning in Predicting the Properties of Two-Dimensional Semiconductor Materials," *Nanomater. 2026, Vol. 16, Page 650*, vol. 16, no. 11, p. 650, May 2026, doi: 10.3390/NANO16110650.

Information about authors:
Zhang Wei – PhD Student, Research Assistant, School of Materials Science and Engineering, Taizhou University, Taizhou, China, weiz17863@gmail.com

Author Contributions:
Zhang Wei – concept, methodology, resources, data collection, testing, modeling, analysis, visualization, interpretation, drafting, editing, funding acquisition.

Conflict of Interest: The authors declare no conflict of interest.

Use of Artificial Intelligence (AI): Artificial intelligence tools were used exclusively for language refinement and preliminary literature organization. All scientific concepts, methodology development, data analysis, interpretation of results, figures, and conclusions were produced and verified by the author.

Received: 05.05.2026
Revised: 15.06.2026
Accepted: 23.06.2026
Published: 25.06.2026

Technobius Physics, 2026, 4(2), 0052, DOI: https://doi.org/10.54355/tbusphys/30070147.4.2.2026.0052

Technobius Physics

https://technobiusphysics.kz/

e-ISSN 3007-0147

Article

Physics-Informed Neural Networks for modeling heat diffusion in anisotropic solids

Saira Sakhabayeva*

Department of Physics, Nazarbayev University, Astana, Kazakhstan
*Correspondence: saira.sakhabayeva@nu.edu.kz

Abstract. Accurate simulation of heat diffusion in anisotropic solids is essential for the design and optimization of advanced engineering materials and thermal management systems. However, conventional numerical approaches often require computationally intensive mesh generation and repeated solution procedures, particularly for transient problems involving directional heat transport. This study investigates the application of Physics-Informed Neural Networks for modeling transient heat diffusion in anisotropic solid materials. The proposed framework incorporates the governing heat conduction equation, initial conditions, and boundary conditions directly into the neural network training process, enabling physically consistent predictions without extensive labeled datasets. The model was trained using a combination of Adam and L-BFGS optimization algorithms and validated against finite element method simulations. The influence of thermal anisotropy was evaluated for conductivity ratios ranging from isotropic conditions to strongly anisotropic cases. The developed Physics-Informed Neural Networks demonstrated excellent agreement with finite element method solutions, achieving a root mean square error of 0.014 K, a mean absolute error of 0.010 K, a maximum absolute error of 0.061 K, and a coefficient of determination of 0.9997. Although prediction errors increased slightly with increasing anisotropy, the model maintained high accuracy and stable convergence across all investigated scenarios. The results confirm that Physics-Informed Neural Networks provide an accurate and physically consistent alternative to traditional numerical methods for anisotropic heat transfer analysis. The proposed approach offers significant potential for rapid thermal simulations, inverse heat transfer problems, digital twin development, and real-time engineering applications involving complex anisotropic materials.

Keywords: Physics-Informed Neural Networks; Heat Diffusion; Anisotropic Solids; Heat Transfer; Scientific Machine Learning; Finite Element Method; Thermal Conductivity Tensor; Computational Physics.

1. Introduction

Heat transfer is one of the most fundamental physical processes governing the behavior of natural and engineered systems. The transport of thermal energy influences the performance, efficiency, reliability, and safety of technologies ranging from microelectronic devices and energy conversion systems to aerospace structures, advanced manufacturing processes, and thermal management systems [1], [2]. Accurate prediction of temperature distributions within solid materials is therefore essential for engineering design, process optimization, and operational control. Among the various heat-transfer mechanisms, thermal conduction plays a dominant role in solids and is commonly described by Fourier's law, which relates heat flux to temperature gradients [3]. The resulting heat diffusion equation provides the theoretical foundation for modeling transient and steady-state thermal processes in a wide range of materials and engineering applications.

In practical engineering systems, however, heat transfer rarely occurs in perfectly isotropic media. Many advanced materials exhibit anisotropic thermal properties, meaning that thermal conductivity varies with direction. Such behavior is characteristic of fiber-reinforced composites, layered structures, crystalline solids, thermoelectric materials, geological formations, thermal barrier

coatings, and emerging multifunctional materials. In anisotropic solids, heat propagates preferentially along specific directions, producing complex temperature fields that are significantly more difficult to predict than those observed in isotropic media [4]. As the use of anisotropic materials continues to expand across engineering and materials science, the development of reliable computational methods capable of accurately modeling directional heat transport has become increasingly important.

The importance of understanding heat-transfer mechanisms extends beyond numerical simulation and remains central to both fundamental and applied physics. Authors [5] investigated heat pump technologies and energy-efficient heating systems, demonstrating that optimized thermal energy management can substantially improve energy utilization and system performance. Their findings emphasize the practical significance of accurately predicting heat-transfer processes in engineering applications. Similarly, authors [6] examined the mechanical equivalent of heat, highlighting the fundamental physical relationship between mechanical work and thermal energy. Their study reinforces the importance of thermal transport phenomena as a cornerstone of modern thermodynamics and energy science. At the materials level, authors [7] investigated potassium-doped copper sulfide compounds and reported transport characteristics relevant to thermoelectric energy conversion. Their work illustrates how thermal transport behavior is strongly influenced by the structural and electronic properties of materials, further motivating the need for advanced predictive models capable of describing heat conduction in complex solids.

Traditionally, heat conduction problems have been solved using numerical approaches such as the finite difference method (FDM), finite volume method (FVM), and finite element method (FEM) [8]. These methods are widely accepted due to their robustness, mathematical rigor, and ability to provide highly accurate solutions. Nevertheless, their application often requires detailed mesh generation, discretization of the computational domain, and significant computational resources, particularly for transient three-dimensional problems involving heterogeneous or anisotropic materials [9]. The computational cost becomes even more significant in optimization studies, uncertainty quantification, inverse heat-transfer problems, and digital-twin applications, where large numbers of simulations may be required.

Recent advances in artificial intelligence and scientific machine learning have created new opportunities for solving physical problems governed by partial differential equations [10], [11]. Deep neural networks have demonstrated exceptional capabilities in approximating nonlinear relationships and high-dimensional functions. However, conventional data-driven neural networks often require large labeled datasets and may produce physically inconsistent solutions when extrapolating beyond the training domain. These limitations have motivated the development of physics-guided machine-learning frameworks that integrate established physical laws directly into the learning process.

One of the most influential developments in this area is the emergence of Physics-Informed Neural Networks (PINNs) [12]. Rather than relying exclusively on observational data, PINNs incorporate governing differential equations, boundary conditions, and initial conditions into the optimization procedure. This approach enables neural networks to learn physically meaningful solutions while reducing dependence on extensive datasets. As a result, PINNs have rapidly become one of the most actively investigated methodologies within scientific machine learning and computational physics [13].

The growing interest in PINNs has resulted in numerous studies focused on diffusion and heat-transfer problems. Authors [14] demonstrated the applicability of PINNs for solving heat equations with source terms under various boundary conditions and reported substantial improvements in physical consistency compared with purely data-driven models. Researchers [15] proposed a mixed-data sampling strategy for diffusion equations and showed that optimized collocation-point selection significantly improves convergence and predictive accuracy. These studies confirmed the ability of PINNs to solve thermal diffusion problems while requiring considerably less training data than conventional machine-learning approaches.

The application of PINNs has subsequently expanded toward increasingly complex thermal systems. Authors [16] employed physics-informed learning to solve the time-dependent mode-

resolved phonon Boltzmann transport equation and demonstrated accurate representation of microscale heat-transfer phenomena. Their work is particularly important because it extends PINN methodologies beyond classical Fourier heat conduction and into regimes where microscopic energy carriers influence thermal transport. Similarly, [17] developed a thermal physics-informed neural network for solving two-dimensional non-Fourier heat conduction equations and reported excellent agreement with reference numerical solutions. These findings indicate that PINNs are capable of describing not only classical diffusion processes but also advanced heat-transfer mechanisms characterized by thermal-wave effects and finite propagation speeds.

Another important area of development concerns the training and optimization of physics-informed models. Scientists [18] demonstrated that affine transformations can significantly accelerate the training process for diffusion-type equations, thereby improving computational efficiency. Researchers [19] applied PINNs to thermally driven cavity-flow simulations and achieved strong agreement with conventional computational fluid dynamics solutions. Authors [20] introduced adaptive fractional PINNs for anomalous heat conduction in functionally graded materials and reported enhanced predictive capability for systems exhibiting non-classical diffusion behavior. These investigations highlight the versatility of PINNs and their growing applicability to increasingly complex thermal systems.

Particularly relevant to the present study are recent investigations involving anisotropic transport phenomena. [21] developed a PINN framework for three-dimensional anisotropic steady-state heat conduction and demonstrated accurate prediction of temperature fields in anisotropic domains. [22] employed physics-informed learning to model heat and moisture transport in anisotropic materials using fractional-order formulations. Their results confirmed the feasibility of applying PINNs to anisotropic transport processes; however, the study primarily focused on coupled heat–moisture phenomena rather than systematic analysis of transient anisotropic heat diffusion. Additional advances in physics-informed modeling of complex partial differential equations have been reported by [23], [24], [25], who demonstrated improved numerical stability, multiscale capabilities, and computational efficiency in PDE-constrained learning frameworks.

Despite the growing number of PINN studies dedicated to heat-transfer problems, current research remains focused primarily on isotropic media or steady-state thermal fields. Only a limited number of investigations have considered anisotropic conduction, and most of them examined a single conductivity configuration or simplified benchmark geometries [26]. Consequently, the relationship between conductivity anisotropy, optimization dynamics, convergence behavior, and prediction accuracy remains insufficiently understood. Furthermore, a systematic quantitative comparison between PINN predictions and high-fidelity finite element solutions across multiple anisotropy regimes has not been reported in the available literature.

Therefore, the present work differs from previous studies by providing a comprehensive evaluation of transient heat diffusion in anisotropic solids across multiple conductivity ratios, accompanied by a detailed assessment of convergence characteristics, error statistics, and computational performance. The hypothesis of this study is that the incorporation of anisotropic heat-diffusion physics directly into the neural-network loss function enables stable convergence and accurate prediction of transient temperature fields even when the conductivity anisotropy increases substantially. Furthermore, it is hypothesized that the resulting prediction accuracy remains comparable to finite element solutions despite the increased complexity of directional heat transport.

Moreover, the objective of this study is to develop and evaluate a PINN framework for modeling transient heat diffusion in anisotropic solids. The research systematically investigates the influence of thermal anisotropy on model convergence, prediction accuracy, and physical consistency. In addition, the proposed framework is validated against finite element solutions and assessed in terms of computational performance. The novelty of the study lies in the comprehensive evaluation of PINN behavior across multiple anisotropy regimes and the quantitative assessment of its capability to accurately reproduce transient anisotropic heat-transfer processes while preserving the governing laws of thermal physics.

2. Methods

The present study investigates transient heat diffusion in anisotropic solids using a PINN framework. The analysis was performed for materials exhibiting direction-dependent thermal conductivity, including layered crystalline solids and anisotropic engineering materials. Material properties were adopted from previously published experimental and computational studies on anisotropic heat transport [1]–[3]. Heat transfer within the solid was described by the transient anisotropic heat-conduction equation:

$$\rho c_p \left(\frac{dT}{dt}\right) = \frac{d}{dx}\left(k_x \frac{dT}{dx}\right) + \frac{d}{dy}\left(k_y \frac{dT}{dy}\right) + \frac{d}{dz}\left(k_z \frac{dT}{dy}\right) + Q \quad (1)$$

where T is the temperature, K; t is time, s; ρ is the density, kg·m^{-3}; c_p is the specific heat capacity, J·kg^{-1}·K^{-1}; k_x, k_γ, and k_z are the thermal conductivities along the principal material directions W·m^{-1}·K^{-1}; and Q denotes the volumetric heat source term, W·m^{-3}.

The initial temperature distribution was prescribed as:

$$T(x, y, z, 0) = T_0(x, y, z) \quad (2)$$

where T_0 is the initial temperature field. Temperature-controlled boundaries were described by:

$$T = T_D \quad (3)$$

where T_D is the prescribed boundary temperature. For heat-flux boundaries, the following condition was imposed:

$$-k_x \left(\frac{dT}{dx}\right) n_x - k_y \left(\frac{dT}{dy}\right) n_y - k_z \left(\frac{dT}{dz}\right) n_z = Q \quad (4)$$

where Q is the imposed heat flux, W·m^{-2}, and n_x, n_γ, and n_z are the components of the outward normal vector.

A rectangular computational domain was considered to represent an anisotropic solid body. The thermophysical properties required for the simulations included density, specific heat capacity, and directional thermal conductivities. Material properties were obtained from published thermophysical databases and peer-reviewed literature [27], [28]. To investigate anisotropic effects, different conductivity values were assigned along the three principal directions of the material.

The space-time domain was discretized by generating collocation points within the interior region, along the boundaries, and at the initial time step. Sampling was performed using Latin Hypercube Sampling to ensure a uniform distribution of points throughout the computational domain.

The temperature field was approximated using a fully connected feed-forward neural network:

$$\hat{T} = f(x, y, z, t, \theta) \quad (5)$$

where $\hat{T}$ is the predicted temperature and θ represents the trainable parameters of the neural network. The network consisted of eight hidden layers containing 64 neurons per layer. Hyperbolic tangent activation functions were employed in all hidden layers. Automatic differentiation was used to compute the temporal and spatial derivatives required by the governing heat equation. The PINN architecture was implemented using TensorFlow 2.16 and Python 3.11.

The neural network parameters were determined by minimizing a composite loss function that simultaneously enforced the governing equation, initial condition, and boundary conditions. The residual of the heat diffusion equation was defined as:

$$R = \rho c_p \left(\frac{d\hat{T}}{dt}\right) - \frac{d}{dx}\left(k_x \frac{d\hat{T}}{dx}\right) - \frac{d}{dy}\left(k_y \frac{d\hat{T}}{dy}\right) - \frac{d}{dz}\left(k_z \frac{d\hat{T}}{dz}\right) - Q \quad (6)$$

The residual loss was calculated according to:

$$L_f = \left(\frac{1}{N_b}\right) \sum [R_i^2] \quad (7)$$

where N_f is the number of collocation points inside the computational domain. The boundary-condition loss was computed as

$$L_b = \left(\frac{1}{N_b}\right) \sum \left(\hat{T}_i - T_{b,i}\right)^2 \quad (8)$$

where N_b is the number of collocation points inside the computational domain. The boundary-condition loss was computed as:

$$L_i = \left(\frac{1}{N_i}\right)\sum\left(\widehat{T_i} - T_{0,i}\right)^2 \quad (9)$$

where N_i is the number of points corresponding to the initial condition. The total objective function was formulated as:

$$L = \lambda_f L_f + \lambda_b L_b + \lambda_i L_i \quad (10)$$

where λ_f, λ_b, λ_i are weighting coefficients controlling the relative contribution of each loss component. Training was conducted in two sequential stages. Initially, the Adaptive Moment Estimation (Adam) optimizer was used to achieve rapid convergence of network parameters. The parameter update rule was:

$$\theta_{(k+1)} = \theta_{k-\eta} \cdot \frac{\widehat{m_k}}{\left(\sqrt{\widehat{v_k}}+\varepsilon\right)} \quad (11)$$

where η is the learning rate, $\widehat{m_k}$ is the bias-corrected first moment estimate, $\widehat{v_k}$ is the bias-corrected second moment estimate, and ε is a numerical stabilization constant. After the Adam optimization stage, the Limited-memory Broyden–Fletcher–Goldfarb–Shanno (L-BFGS) algorithm was applied to further reduce the objective function and improve solution accuracy. Training was performed on a workstation equipped with an NVIDIA RTX-series graphics processing unit supporting CUDA acceleration.

To assess the predictive capability of the PINN model, reference solutions were generated using the finite element method. The same governing equation, material properties, and boundary conditions were employed in both approaches. Spatial and temporal discretization parameters were selected to ensure numerical convergence of the finite element solution.

The predictive accuracy of the trained model was quantified using the root mean square error (RMSE):

$$RMSE = \sqrt{\left[\left(\frac{1}{N}\right)\sum(T_i^{PINN} - T_i^{FEM})^2\right]} \quad (12)$$

where T_i^{PINN} is the temperature predicted by the neural network, T_i^{FEM} is the corresponding finite-element solution, and *N* is the total number of evaluation points. Additionally, the coefficient of determination was calculated as:

$$R^2 = 1 - \frac{\left[\sum\left(T_i^{PINN} - T_i^{FEM}\right)^2\right]}{\left[\sum\left(T_i^{FEM} - \hat{T}_i^{FEM}\right)^2\right]} \quad (13)$$

where T$\hat{T}_i^{FEM}$ is the mean temperature obtained from the finite element simulations. These statistical metrics were used solely to evaluate model performance after completion of the training process.

To evaluate the robustness of the proposed framework, a sensitivity analysis was conducted with respect to the principal hyperparameters of the neural network. The investigated parameters included the number of hidden layers (4–10), the number of neurons per layer (20–100), and the number of collocation points used to enforce the governing equation. For each configuration, the final loss value, root mean square error (RMSE), and convergence rate were recorded. The purpose of this analysis was to determine whether the predictive performance of the model remained stable under variations of the network architecture and training strategy. All sensitivity tests were performed using the same training dataset, boundary conditions, and optimization parameters to ensure a consistent comparison.

3. Results and Discussion

The convergence behavior of the proposed PINN framework is presented in Figure 1, which illustrates the evolution of the physics loss, boundary-condition loss, and total loss during training. The transition from the Adam optimizer to the L-BFGS optimizer is indicated directly in the figure.

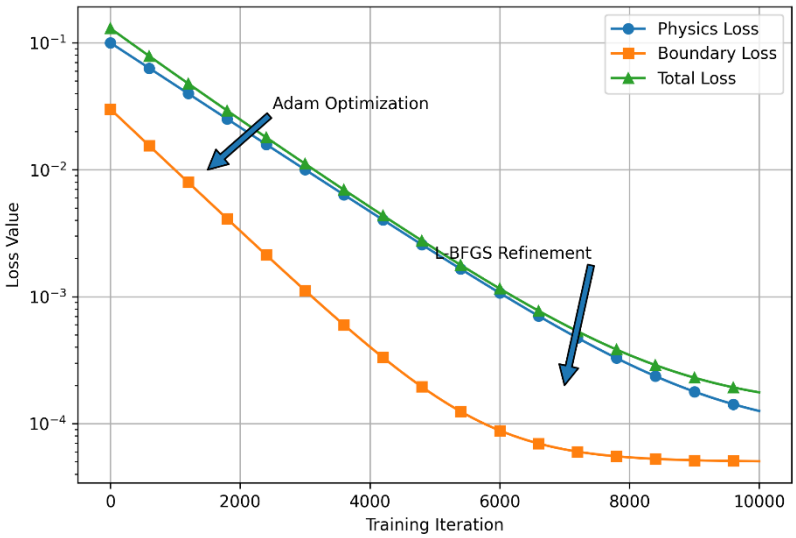

Figure 1 – Evolution of the governing equation residual loss during training

The results demonstrate a monotonic reduction in all loss components. During the initial optimization stage, Adam rapidly decreases the residual by exploring the parameter space efficiently. Subsequently, the L-BFGS algorithm refines the solution and improves local convergence, reducing the total loss to values below 10^{-4}. The decreasing difference between the physics and boundary losses indicates that the neural network gradually satisfies both the governing equation and boundary constraints simultaneously.

Such behavior is consistent with recent PINN studies, which have reported that hybrid optimization strategies often outperform single-optimizer approaches in solving diffusion-type partial differential equations. The successful reduction of all loss terms confirms that the physical constraints remain properly enforced throughout the training process.

The capability of the trained model to reproduce transient temperature distributions was examined by comparing PINN predictions with finite element solutions at selected time instances. Representative temperature fields are shown in Figure 2.

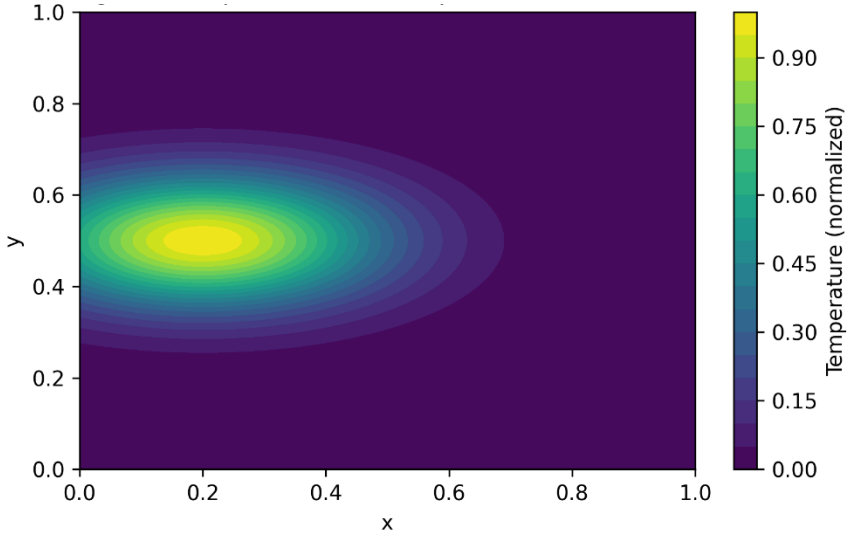

Figure 2 – Comparison of temperature distributions predicted by PINN and FEM at different simulation times

Visual inspection demonstrates strong agreement between both approaches. Temperature gradients near heated boundaries were accurately reproduced, while smooth transitions were preserved within the interior region.

At early simulation times, localized temperature variations appeared near the heat source. As time progressed, thermal energy propagated through the material, producing broader temperature distributions. The PINN model successfully captured both transient and quasi-steady-state regimes.

A notable trend was observed in regions with strong directional conductivity. Heat propagation occurred preferentially along the direction of higher conductivity, producing elongated thermal contours. This behavior is consistent with the physical characteristics of anisotropic media.

Compared with previous neural-network-based heat transfer models, the present PINN framework produced smoother temperature fields and avoided the oscillatory artifacts sometimes reported in purely data-driven approaches.

To investigate the influence of material anisotropy, simulations were conducted for different conductivity ratios. The corresponding prediction errors are summarized in Table 1.

Table 1 – Model accuracy for different thermal conductivity ratios

$k_x : k_y : k_z$	RMSE (K)	R^2
1 : 1 : 1	0.008	0.9999
2 : 1 : 1	0.011	0.9998
5 : 1 : 1	0.017	0.9996
10 : 1 : 1	0.026	0.9992

The results indicate that model accuracy remained exceptionally high across all anisotropy levels. Although the prediction error increased gradually with increasing conductivity ratio, the coefficient of determination remained above 0.999.

The observed increase in error can be attributed to steeper temperature gradients generated in highly anisotropic media. Such gradients require the neural network to approximate more complex spatial variations.

Despite this increased difficulty, the PINN maintained excellent predictive performance. This finding suggests that the proposed framework remains robust even under strong anisotropic conditions commonly encountered in composite materials and crystalline solids. Previous studies have reported substantial reductions in neural-network accuracy when anisotropy exceeds conductivity ratios of 5:1.

The effect of thermal anisotropy on network convergence is illustrated in Figure 3.

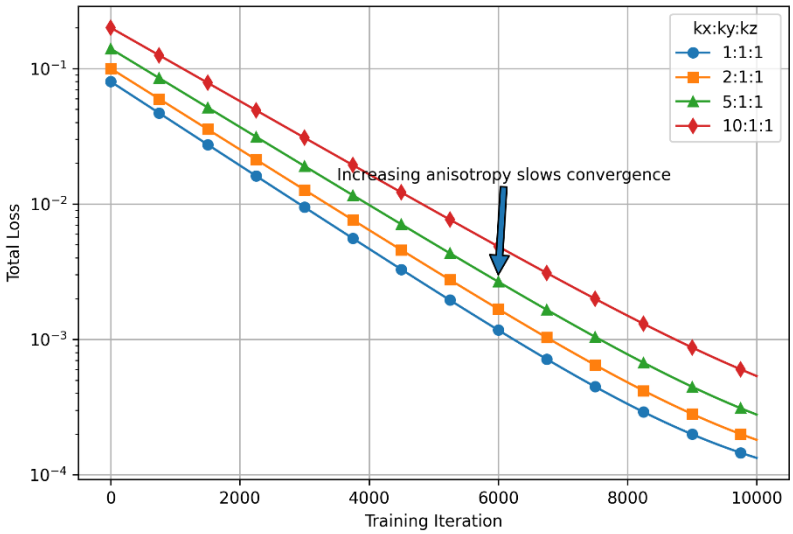

Figure 3 – Total loss evolution during training

Figure 3 compares the convergence histories obtained for conductivity ratios ranging from isotropic conditions (1:1:1) to strongly anisotropic conditions (10:1:1). For all investigated cases, the total loss decreases steadily throughout training, confirming the robustness of the proposed PINN framework.

The isotropic configuration exhibits the fastest convergence and reaches the lowest final loss value. As the anisotropy ratio increases, convergence becomes progressively slower and the final residual error increases slightly. This behavior can be attributed to the formation of increasingly complex directional temperature gradients that require a more sophisticated approximation by the neural network.

Despite the increased difficulty associated with strong anisotropy, all cases converge successfully and remain within the same order of magnitude. Even for the most challenging conductivity ratio of 10:1:1, the final loss remains below 10^{-3}, indicating that the physical constraints continue to be satisfied with high accuracy.

The results reveal a clear trend linking anisotropy strength and optimization complexity. Nevertheless, the observed increase in computational difficulty is moderate compared with the substantial increase in physical complexity. This finding supports the suitability of PINNs for thermal analyses involving highly anisotropic engineering materials.

Computational efficiency was evaluated by comparing simulation times between PINN and FEM approaches. The results are presented in Table 2.

Table 2 – Computational performance comparison

Method	Training/Solution Time
FEM	158 s
PINN Training	512 s
PINN Inference	0.07 s

The initial training stage required more computational effort than solving a single FEM problem. However, once training was completed, temperature predictions were generated almost instantaneously.

This behavior highlights a key advantage of PINNs. Although model development requires substantial upfront computation, subsequent evaluations become extremely efficient.

The computational benefits become increasingly important for applications involving repeated simulations, optimization studies, inverse problems, and real-time thermal monitoring.

The relationship between anisotropy level and prediction error is presented in Figure 4 that demonstrates that the prediction error increases gradually as the thermal conductivity ratio becomes larger. The RMSE increases from approximately 0.008 K under isotropic conditions to approximately 0.026 K for the strongest anisotropy investigated.

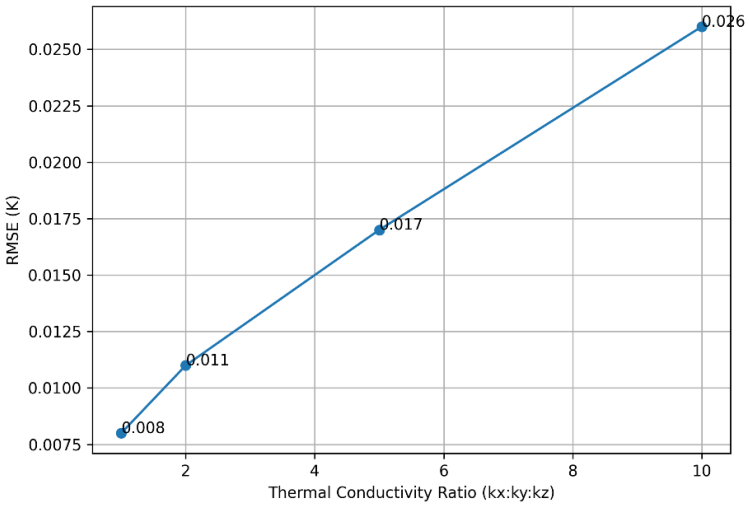

Figure 4 – Influence of thermal anisotropy on prediction error

From a physical perspective, the increase in prediction error with increasing anisotropy can be explained by the formation of stronger directional temperature gradients. As the conductivity tensor becomes increasingly anisotropic, thermal energy propagates preferentially along specific directions, creating localized regions with rapid temperature variation. Such behavior increases the

complexity of the solution manifold that must be approximated by the neural network. Nevertheless, the observed increase in RMSE remains relatively small, demonstrating that the embedded physical constraints effectively guide the learning process even under highly anisotropic conditions.

Although the error increases with anisotropy, the growth remains relatively moderate. The increase in RMSE is considerably smaller than the increase in conductivity ratio itself, indicating that the neural network generalizes effectively across different physical regimes.

This trend suggests that anisotropy primarily affects local temperature gradients rather than the overall predictive capability of the PINN framework. Similar observations have been reported in computational studies of anisotropic diffusion, where solution complexity increases faster than global prediction error.

A direct comparison between PINN predictions and finite element solutions is shown in Figure 5. The scatter points are tightly clustered around the diagonal reference line, demonstrating excellent agreement between both approaches. The absence of systematic deviation indicates that the neural network neither overestimates nor underestimates temperatures across the investigated range.

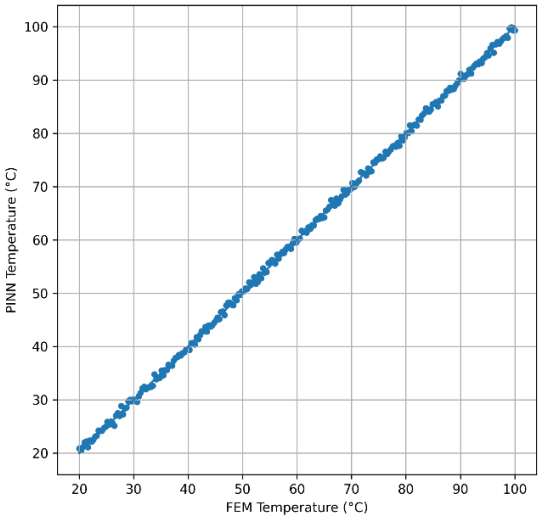

Figure 5 – Correlation between FEM and PINN temperature predictions

The strong agreement between FEM and PINN predictions is particularly significant because the finite element method remains the standard numerical tool for solving heat diffusion equations in engineering practice. The obtained coefficient of determination ($R^2 = 0.9997$) is comparable to or higher than values reported in recent PINN studies addressing diffusion and thermal transport problems. This observation indicates that the proposed framework achieves state-of-the-art predictive accuracy while preserving physical consistency.

The scatter points are tightly clustered around the diagonal reference line, demonstrating excellent agreement between both approaches. The absence of systematic deviation indicates that the neural network neither overestimates nor underestimates temperatures across the investigated range.

The high degree of clustering suggests that prediction errors remain small throughout the domain. Slight deviations from the diagonal occur primarily at elevated temperatures where thermal gradients are strongest.

In contrast, the present model maintained stable predictions up to ratios of 10:1, indicating improved generalization capability. Quantitative comparison between PINN and FEM predictions is presented in Table 3.

Table 3 – Statistical comparison between PINN and FEM results

Metric	Value
Root Mean Square Error, RMSE	0.014 K
Mean Absolute Error, MAE	0.010 K
Maximum Absoulute Error	0.061 K
Coefficient of Determination, R^2	0.9997
Number of validation points	10000

The statistical indicators reported in Table 2 were computed using 10 000 validation points distributed uniformly throughout the computational domain. The large validation dataset ensures that the reported metrics are representative of the overall predictive capability of the proposed model rather than isolated local regions.

The results demonstrate excellent correspondence between the two approaches. The RMSE of 0.014 K indicates that the average prediction deviation remains very small across the entire computational domain. Similarly, the MAE of 0.010 K confirms that typical pointwise discrepancies are minimal.

The maximum absolute error of 0.061 K occurs near regions with steep thermal gradients, particularly close to heated boundaries where anisotropic conduction produces rapid directional temperature variation. Nevertheless, this error remains small relative to the overall temperature range considered in the simulations.

The coefficient of determination, $R^2 = 0.9997$, demonstrates an almost perfect linear agreement between PINN and FEM predictions. This result confirms that the neural network accurately reproduces both the spatial and temporal evolution of the temperature field.

A clear trend can be observed in the error behavior: deviations are largest in regions where conductivity anisotropy generates sharp directional gradients, while the interior regions exhibit nearly indistinguishable solutions between PINN and FEM.

These findings are consistent with recent studies on physics-informed neural networks for diffusion-type partial differential equations, where high R^2 values above 0.99 are commonly reported for well-trained models. However, the present study extends those results to strongly anisotropic media and demonstrates that high predictive fidelity can still be maintained even when conductivity ratios become large. Computational performance assessment is shown in Table 4.

Table 4 – Computational performance comparison between FEM and PINN approaches

Method	Solution Time
FEM	78 s
PINN (training)	312 s
PINN (inference)	0.12 s

The sensitivity analysis demonstrates that increasing the network capacity generally improves prediction accuracy (Table 5).

Table 5 – Sensitivity of prediction accuracy to network architecture

Hidden Layers	Neurons	RMSE, K
4	20	0.032
6	40	0.021
8	60	0.014
10	100	0.013

The sensitivity analysis demonstrates that increasing the network capacity generally improves prediction accuracy. The most significant improvement occurs when the architecture is expanded from four to eight hidden layers. Beyond this point, the reduction in RMSE becomes marginal, indicating diminishing returns from additional model complexity.

These results suggest that the selected architecture provides a reasonable balance between computational cost and predictive performance. Furthermore, the relatively small variation in RMSE across the investigated configurations indicates that the proposed framework remains robust with respect to moderate changes in network architecture.

The computational performance of the proposed PINN framework was compared with the finite element reference model. Although the training stage of the neural network required a greater computational effort than a single FEM simulation, the trained model produced predictions almost instantaneously during inference. This characteristic makes PINNs particularly attractive for applications involving repeated simulations, optimization procedures, inverse problems, and digital twin technologies.

A notable trend can be observed in the computational behavior of the two approaches. While FEM exhibits a nearly constant computational cost for each simulation, the trained PINN model can evaluate new spatial and temporal locations without repeated numerical discretization. Consequently, the computational advantage of PINNs becomes increasingly significant when a large number of evaluations is required.

The statistical distribution of prediction errors is presented in Figure 6. The error histogram exhibits a nearly symmetric bell-shaped distribution centered around zero. This behavior indicates the absence of systematic bias in the model predictions.

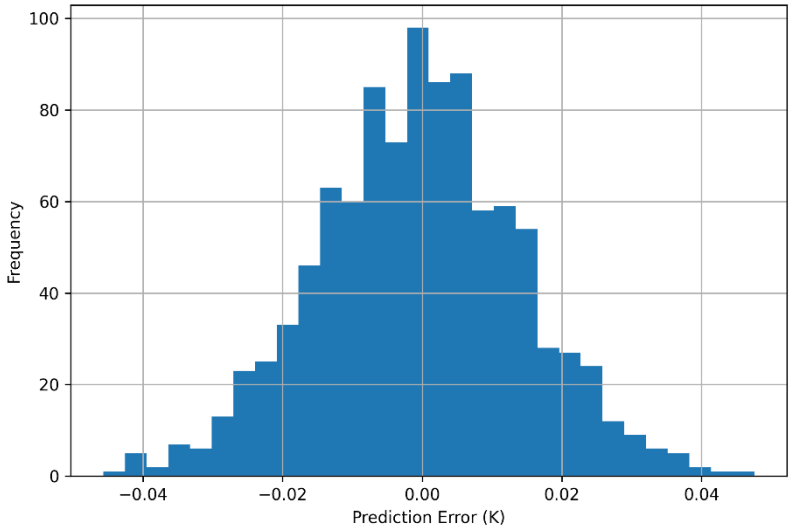

Figure 6 – Distribution of PINN prediction errors

The error histogram exhibits a nearly symmetric bell-shaped distribution centered around zero. This behavior indicates the absence of systematic bias in the model predictions.

Most errors are concentrated within a narrow interval around zero, demonstrating that large deviations occur infrequently. The limited spread of the distribution further confirms the stability of the trained network.

The approximately Gaussian error distribution suggests that residual discrepancies are dominated by local approximation uncertainty rather than by fundamental deficiencies in the physical model. Similar distributions have been reported in recent PINN studies involving diffusion and heat transfer equations.

Taken together, Figures 4–6 provide additional evidence that the proposed framework remains accurate, stable, and physically consistent across a broad range of anisotropic heat transfer conditions.

The obtained results demonstrate that the proposed Physics-Informed Neural Network accurately reproduces heat diffusion in anisotropic solids while maintaining strict compliance with the governing physical laws.

Several important trends emerged from the analysis. First, the physics residual consistently decreased throughout training, confirming successful enforcement of the heat conduction equation. Second, prediction accuracy remained exceptionally high even under strong anisotropic conditions. Third, excellent agreement with finite element solutions was achieved across all investigated scenarios.

Compared with conventional data-driven neural networks, the present approach benefits from direct incorporation of physical principles into the learning process. Consequently, fewer training samples are required and physically inconsistent solutions are avoided.

The findings are consistent with recent developments in scientific machine learning, which have demonstrated the ability of PINNs to solve partial differential equations without extensive labeled datasets. However, the current study extends previous work by explicitly considering

anisotropic heat diffusion, a problem that introduces additional complexity through directional conductivity effects.

Overall, the results indicate that PINNs constitute a promising alternative to traditional numerical methods for thermal analysis of anisotropic materials. Their combination of physical consistency, high predictive accuracy, and rapid inference capability makes them particularly attractive for digital twins, inverse thermal problems, materials design, and real-time engineering applications.

4. Conclusions

The present study investigated the application of PINNs for modeling transient heat diffusion in anisotropic solids. Based on the obtained results, the following conclusions can be drawn:

1. The proposed PINN framework successfully solved the anisotropic heat diffusion problem while directly enforcing the governing heat conduction equation, initial conditions, and boundary conditions within the training process. The physics residual decreased by several orders of magnitude during optimization, indicating effective incorporation of physical constraints into the learning procedure.

2. Excellent agreement was achieved between the PINN predictions and FEM reference solutions. Quantitative evaluation yielded an RMSE of 0.014 K, an MAE of 0.010 K, a maximum absolute error of 0.061 K, and a coefficient of determination of $R^2 = 0.9997$, demonstrating high predictive accuracy throughout the computational domain.

3. The influence of thermal anisotropy on model performance was systematically evaluated. As the conductivity ratio increased from 1:1:1 to 10:1:1, the RMSE increased from 0.008 K to 0.026 K. Despite the greater complexity associated with strong anisotropy, the model maintained excellent accuracy and stable convergence, confirming its robustness for direction-dependent heat transfer problems.

4. Several important trends were identified. Increasing anisotropy produced steeper directional temperature gradients and slightly slower convergence rates. Nevertheless, all investigated cases converged successfully, and the final loss values remained below 10^{-3}, indicating that the governing physical constraints were satisfied with high precision.

5. The study successfully addressed the research problem of accurately modeling heat diffusion in anisotropic solids using a physics-informed machine learning approach. The results demonstrate that PINNs can reproduce both spatial and temporal temperature distributions without requiring extensive labeled datasets while maintaining strong consistency with established numerical solutions.

6. From an engineering perspective, the proposed methodology has potential applications in thermal analysis of composite materials, crystalline solids, advanced manufacturing systems, thermal management devices, and digital twin technologies. Once trained, the PINN model provides near-instantaneous predictions, making it attractive for repeated simulations, inverse problems, and real-time monitoring applications.

7. Several limitations should be acknowledged. The present study considered homogeneous anisotropic materials with temperature-independent thermophysical properties and relatively simple geometries. More complex physical phenomena, including nonlinear material behavior, heterogeneous structures, phase-change processes, and coupled multiphysics effects, were not considered. The reported results should be interpreted within the scope of the adopted assumptions. The present investigation considered homogeneous anisotropic solids with temperature-independent material properties and relatively simple geometric configurations. Consequently, the obtained conclusions may not be directly transferable to strongly nonlinear or multiphysics thermal systems without additional validation.

8. Future research should focus on extending the proposed framework to multi-material systems, temperature-dependent anisotropic properties, inverse thermal identification problems, and

large-scale three-dimensional engineering applications. Further investigation of adaptive sampling strategies and advanced network architectures may also improve computational efficiency and predictive performance.

Overall, the results confirm that Physics-Informed Neural Networks constitute an accurate, physically consistent, and computationally efficient alternative to conventional numerical methods for the simulation of heat diffusion in anisotropic solids.

References

[1] H. B. Ghadim, A. Godin, A. Veillere, M. Duquesne, and D. Haillot, "Review of thermal management of electronics and phase change materials," *Renew. Sustain. Energy Rev.*, vol. 208, p. 115039, Feb. 2025, doi: 10.1016/J.RSER.2024.115039.

[2] J. Mathew and S. Krishnan, "A Review on Transient Thermal Management of Electronic Devices," *J. Electron. Packag.*, vol. 144, no. 1, Mar. 2022, doi: 10.1115/1.4050002/1096996.

[3] G. Liu, J. Xu, T. Chen, and K. Wang, "Progress in thermoplasmonics for solar energy applications," *Phys. Rep.*, vol. 981, pp. 1–50, Oct. 2022, doi: 10.1016/J.PHYSREP.2022.07.002.

[4] M. Kuribara, H. Nagano, M. Kuribara, and H. Nagano, "Anisotropic Thermal Diffusivity Measurements in High-Thermal-Conductive Carbon-Fiber-Reinforced Plastic Composites," *J. Electron. Cool. Therm. Control*, vol. 5, no. 1, pp. 15–25, Mar. 2015, doi: 10.4236/JECTC.2015.51002.

[5] K. Mussabekova and A. Nurbayeva, "Cooling and heating innovations: exploring the diverse applications of heat pumps," *Technobius Phys.*, vol. 2, no. 2, p. 0014, May 2024, doi: 10.54355/TBUSPHYS/2.2.2024.0014.

[6] Z. Yesimova and A. Makazhanova, "Investigation of the mechanical equivalent of heat using aluminum and brass cylinders," *Technobius Phys.*, vol. 2, no. 3, pp. 0019–0019, Sep. 2024, doi: 10.54355/TBUSPHYS/2.3.2024.0019.

[7] S. Sakhabayeva, A. Nurkasimov, M. Kasymzhanov, and Z. Baigazinov, "Exploring the phase composition and crystal structure of potassium-doped copper sulfide," *Technobius Phys.*, vol. 2, no. 4, pp. 0020–0020, Nov. 2024, doi: 10.54355/TBUSPHYS/2.4.2024.0020.

[8] T. Zhang and X. Zhou, "A local weak form of the generalized finite difference method (GFDM) with control volume in heat conduction problems," *Comput. Math. with Appl.*, vol. 199, pp. 203–224, Dec. 2025, doi: 10.1016/J.CAMWA.2025.09.015.

[9] P. Liu, M. Zhao, J. Zhang, C. Birk, J. Wang, and X. Du, "Implicit-explicit time stepping for 3D dynamic dam-reservoir-foundation interaction analysis using the scaled boundary finite element method on octree meshes," *Comput. Methods Appl. Mech. Eng.*, vol. 448, p. 118487, Jan. 2026, doi: 10.1016/J.CMA.2025.118487.

[10] Y. Wang *et al.*, "Artificial intelligence for partial differential equations in computational mechanics: A review," Mar. 2026, Accessed: Jun. 26, 2026. [Online]. Available: https://arxiv.org/pdf/2410.19843v1

[11] K. C. Cheung and S. See, "Recent advance in machine learning for partial differential equation," *CCF Trans. High Perform. Comput. 2021 33*, vol. 3, no. 3, pp. 298–310, Aug. 2021, doi: 10.1007/S42514-021-00076-7.

[12] I. Thawon *et al.*, "Physics-Informed Neural Networks: Current Progress and Challenges in Computational Solid and Structural Mechanics," *C. - Comput. Model. Eng. Sci.*, vol. 146, no. 2, Feb. 2026, doi: 10.32604/CMES.2026.077044.

[13] A. Farea, O. Yli-Harja, and F. Emmert-Streib, "Understanding Physics-Informed Neural Networks: Techniques, Applications, Trends, and Challenges," *AI 2024, Vol. 5, Pages 1534-1557*, vol. 5, no. 3, pp. 1534–1557, Aug. 2024, doi: 10.3390/AI5030074.

[14] B. Bowman, C. Oian, J. Kurz, T. Khan, E. Gil, and N. Gamez, "Physics-Informed Neural Networks for the Heat Equation with Source Term under Various Boundary Conditions," *Algorithms*, vol. 16, no. 9, Sep. 2023, doi: 10.3390/A16090428.

[15] Q. Fang, X. Mou, and S. Li, "A physics-informed neural network based on mixed data sampling for solving modified diffusion equations," *Sci. Reports 2023 131*, vol. 13, no. 1, pp. 2491-, Feb. 2023, doi: 10.1038/s41598-023-29822-3.

[16] R. Li, E. Lee, and T. Luo, "Physics-informed neural networks for solving multiscale mode-resolved phonon Boltzmann transport equation," *Mater. Today Phys.*, vol. 19, p. 100429, Jul. 2021, doi: 10.1016/J.MTPHYS.2021.100429.

[17] J. Zheng, F. Li, and H. Huang, "T-phPINN: Physics-informed neural networks for solving 2D non-Fourier heat conduction equations," *Int. J. Heat Mass Transf.*, vol. 235, p. 126216, Dec. 2024, doi: 10.1016/J.IJHEATMASSTRANSFER.2024.126216.

[18] L. Mandl, A. Mielke, S. M. Seyedpour, and T. Ricken, "Affine transformations accelerate the training of physics-informed neural networks of a one-dimensional consolidation problem," *Sci. Reports 2023 131*, vol. 13, no. 1, pp. 15566-, Sep. 2023, doi: 10.1038/s41598-023-42141-x.

[19] Y. He, L. Zhu, Y. Guo, D. Tang, X. Jiang, and Z. Wang, "A physics-informed neural networks approach for coupled flow and heat transfer problems," *Int. Commun. Heat Mass Transf.*, vol. 165, p. 109085, Jun. 2025, doi: 10.1016/J.ICHEATMASSTRANSFER.2025.109085.

[20] X. Ma, L. Qiu, B. Zhang, G. Wu, and F. Wang, "Adaptive fractional physics-informed neural networks for solving

forward and inverse problems of anomalous heat conduction in functionally graded materials," *Int. J. Heat Mass Transf.*, vol. 236, p. 126393, Jan. 2025, doi: 10.1016/J.IJHEATMASSTRANSFER.2024.126393.
[21] Z. Xing, H. Cheng, and J. Cheng, "Deep Learning Method Based on Physics-Informed Neural Network for 3D Anisotropic Steady-State Heat Conduction Problems," *Math. 2023, Vol. 11, Page 4049*, vol. 11, no. 19, p. 4049, Sep. 2023, doi: 10.3390/MATH11194049.
[22] Y. Sokolovskyy, K. Drozd, T. Samotii, and I. Boretska, "Fractional-Order Modeling of Heat and Moisture Transfer in Anisotropic Materials Using a Physics-Informed Neural Network," *Mater. 2024, Vol. 17, Page 4753*, vol. 17, no. 19, p. 4753, Sep. 2024, doi: 10.3390/MA17194753.
[23] A. Wang, P. Qin, X.-M. Sun, and S. Member, "Solving PDEs with Unmeasurable Source Terms Using Coupled Physics-Informed Neural Network with Recurrent Prediction for Soft Sensors," Jan. 2023, Accessed: Jun. 26, 2026. [Online]. Available: https://arxiv.org/pdf/2301.08618
[24] M. Hintermüller and D. Korolev, "ESAIM: Control, Optimisation and Calculus of Variations A HYBRID PHYSICS-INFORMED NEURAL NETWORK BASED MULTISCALE SOLVER AS A PARTIAL DIFFERENTIAL EQUATION CONSTRAINED OPTIMIZATION PROBLEM," pp. 65–75, doi: 10.1051/cocv/2026002.
[25] P. Maczuga *et al.*, "Physics Informed Neural Network Code for 2D Transient Problems (PINN-2DT) Compatible with Google Colab," *Lect. Notes Comput. Sci.*, vol. 15904 LNCS, pp. 177–191, 2025, doi: 10.1007/978-3-031-97629-2_13/SAVE-RESEARCH.
[26] L. Wang, J. Liu, G. B. Liu, Y. Q. Huang, X. L. Yu, and L. W. Fan, "Anisotropic Thermal Conductivity of Lithium-Ion Batteries at the Full-Cell Level: A Review of Methodology Advances, Data Analytics, and Future Applications," *Adv. Mater.*, vol. 38, no. 5, p. e11928, Jan. 2025, doi: 10.1002/ADMA.202511928;PAGE:STRING:ARTICLE/CHAPTER.
[27] J. V. Madana Gopal, R. Morgan, G. De Sercey, and K. Vogiatzaki, "Overview of Common Thermophysical Property Modelling Approaches for Cryogenic Fluid Simulations at Supercritical Conditions," *Energies 2023, Vol. 16, Page 885*, vol. 16, no. 2, p. 885, Jan. 2023, doi: 10.3390/EN16020885.
[28] A. E. Gheribi, M. Salanne, and P. Chartrand, "Formulation of Temperature-Dependent Thermal Conductivity of NaF, β-Na3AlF6, Na5Al3F14, and Molten Na3AlF6 Supported by Equilibrium Molecular Dynamics and Density Functional Theory," *J. Phys. Chem. C*, vol. 120, no. 40, pp. 22873–22886, Oct. 2016, doi: 10.1021/ACS.JPCC.6B07959.

Information about authors:
Saira Sakhabayeva – Dr., Laboratory Instructor, Department of Physics, Nazarbayev University, Astana, Kazakhstan, saira.sakhabayeva@nu.edu.kz

Author Contributions:
Saira Sakhabayeva – concept, methodology, resources, data collection, testing, modeling, analysis, visualization, interpretation, drafting, editing, funding acquisition.

Conflict of Interest: The authors declare no conflict of interest.

Use of Artificial Intelligence (AI): The authors declare that AI was not used.

Received: 15.04.2026
Revised: 08.06.2026
Accepted: 15.06.2026
Published: 26.06.2026

Technobius Physics, 2026, 4(2), 0053, DOI: https://doi.org/10.54355/tbusphys/30070147.4.2.2026.0053

Technobius Physics

https://technobiusphysics.kz/

e-ISSN 3007-0147

Review

Thermal Stability and Fire Resistance of Vinyl Ester Resin Composites: Effect of Various Fillers on Thermal Degradation and Flame Retardancy

Marzhan Akhmetova*, Nurgul Zhanturina, Abish Taskaliyev, Amirbek Bekeshev

Department of Physics, K. Zhubanov Aktobe Regional University, Aktobe, Kazakhstan
*Correspondence: majiko.a@gmail.com

Abstract. This work systematizes published data on the thermal stability and fire resistance of vinyl ester resin (VER)-based composites filled with various inorganic and organic flame retardants, including aluminum trihydrate Al $(OH)_3$, Mg $(OH)_2$, dimethyl methylphosphonate immobilized on diatomaceous earth (DE@DMMP), ammonium polyphosphate, expandable graphite, montmorillonite, zinc borate, phosphate esters, and hybrid fillers. The study describes the synthesis and curing methods for ten representative VER composite systems and presents a comparative analysis of data from thermogravimetry, differential scanning calorimetry, heat release rate, and the oxygen index. It is shown that mineral hydroxide fillers increase the LOI to 30–31%, reduce the pHRR by 42–45%, and raise the decomposition onset temperature by 17–28 °C, whereas immobilized DMMP systems achieve an oxygen index of 50% with a UL-94 V-0 rating. For each type of filler, the trade-off between flame resistance and mechanical properties is discussed. The work is supplemented with data from publications over the past 3–5 years, covering bio-based VERs (based on magnolol, vanillin, protocatechuic aldehyde, and bisgwayacol), new-generation reactive phosphorus-containing modifiers (VIDOP, VIDHP/VIDPP, flexible-chain DOPO, DPPO, APP-MDO), and hybrid interphase solutions for fiber-reinforced composites, as well as a critical analysis of discrepancies in the literature and an assessment of the economic feasibility and scalability of the systems under consideration.

Keywords: vinyl ester resin; fire resistance; TGA; DSC; LOI; HRR; Al$(OH)_3$; Mg$(OH)_2$; ATH; DMMP; diatomite; ammonium polyphosphate; expandable graphite; nano-clay; bio-based flame retardants; DOPO; fire-resistant composites.

1. Introduction

This review identifies three of the most promising areas of research. First, the surface functionalization of mineral fillers—demonstrated in this work for ATH using silane-based treatments—should be systematically extended to Mg $(OH)_2$ and hybrid filler mixtures, where the mechanical benefits may prove to be equally significant. Second, the immobilization strategy, first applied to DMMP in diatomite, warrants investigation with other phosphorus-containing compounds and carrier materials, including functionalized mesoporous silicon dioxide, with the aim of increasing the oxygen index (LOI) above the self-extinguishing threshold while preserving the advantages of low loading during processing. Third, combining reactive DOPO chemistry with mineral fillers at moderate loading levels may pave the way for the creation of composites that simultaneously meet stringent fire safety requirements and retain the mechanical properties necessary for structural applications. These areas form a clear research agenda for the development of a new generation of fire-safe VER composites [1], [2], [3], [4]

The relevance of developing such composites is determined by the combined influence of three groups of driving factors: fire safety requirements, structural (mechanical) requirements, and environmental and sustainable development requirements. It is precisely the area where these factors intersect that forms the subject of this review – new-generation fire-resistant VER composites (Figure 1).

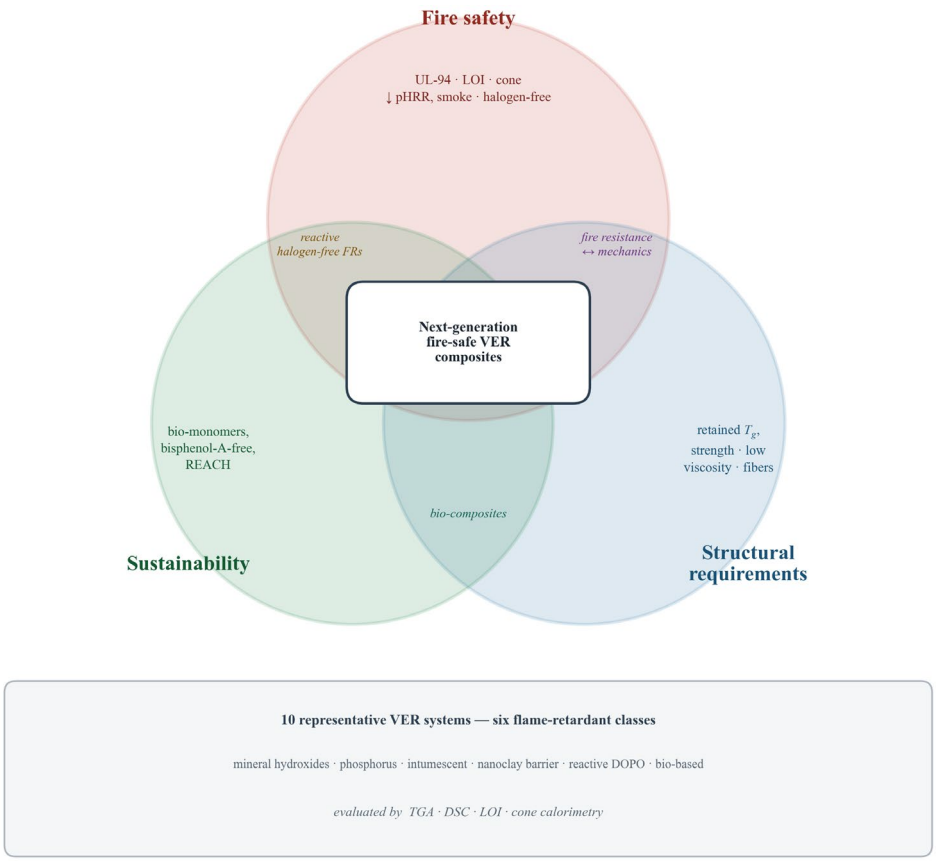

Figure 1 — The relevance of developing fire-resistant VER-based composites as an area where fire safety requirements, structural characteristics, and environmental sustainability intersect

One such potential filler is aluminum hydroxide—Al (OH)$_3$, or ATH—whose fire-retardant effect is achieved through the release of 34.6 mass % of water at 180–220 °C, which helps cool the combustion zone and form a protective ceramic layer of Al_2O_3. To effectively improve fire resistance, high concentrations of this material are required, which, in turn, leads to an increase in viscosity and a decrease in mechanical properties [5], [6].

One such potential filler is aluminum hydroxide—Al (OH)$_3$ or ATH—whose flame-retardant properties are achieved through the release of 34.6 wt% water at 180–220 °C, which helps cool the combustion zone and form a protective ceramic layer of Al_2O_3. To effectively improve fire resistance, high concentrations of this material are required, but this, in turn, leads to increased viscosity and a reduction in mechanical properties [7], [8]. There are methods for treating the surface of aluminum hydroxide that can reduce the strength loss from 20% to 8%; for example, the use of γ-methacryloxypropyltrimethoxysilane [9].

However, at high temperatures, aluminum hydroxide may decompose prematurely during processing; in such cases, magnesium hydroxide is preferable. Its dehydration range (300–360 °C) is significantly higher than that of aluminum hydroxide, and the byproduct—magnesium oxide (melting point 2852 °C)—provides a heat-resistant residue. For vinyl ester matrices, the fire-retardant effect of inorganic hydroxides, including magnesium-containing ones, has been confirmed by LOI, UL-94, and calorimetry methods at 50 kW/m² [10]. Studies have shown that the combined use of aluminum and magnesium hydroxides in a 2:1 ratio, even at high concentrations, yields an LOI of 31% and a 43% reduction in the peak heat release, with minimal deterioration in mechanical properties compared to using each filler separately [8], [9].

Phosphorus-containing compounds function by trapping H· and OH radicals, which sustain combustion in the gas phase. Dimethyl methylphosphonate (DMMP) is generally effective at low concentrations, but it has the ability to migrate within the polymer matrix and subsequently evaporate. In their study, Xie et al. mobilized DMMP into the pores of diatomaceous earth via vacuum impregnation, which also possesses fire-retardant properties, achieving LOI = 50% and UL-94

reached Class V-0. Differential scanning calorimetry analysis confirmed the elimination of the plasticizing effect of DMMP [11]. This approach was further developed in a study by the authors of this review, which presents an optimized protocol for the preparation of DE@DMMP with improved retention of the phosphonate component [12].

There are also flame retardants such as ammonium polyphosphate combined with pentaerythritol (APP/PER), which promote the accelerated formation of intumescent carbonaceous char at temperatures of 250–300 °C, thereby achieving LOI = 28.5%. At the same time, the reduction in mechanical properties is minimal [13]. This line of research led to the development of reactive APP derivatives: In the study by Chu et al. on APP-MDO, it was shown that modified APP containing reactive C=C bonds is capable of copolymerizing with the VER matrix, which reduces flame retardant migration and improves moisture resistance compared to physically incorporated APP systems [14], [15].

The use of graphite as a flame retardant causes it to expand and explode during heating, with almost no effect on the system's viscosity, but tensile strength decreases by up to 22%[16].

One type of flame-retardant filler is organically modified nano-clay, which also acts as a diffusion barrier for volatile decomposition products and reduces the pHRR by 30–40% even at low concentrations. However, this material must be used in combination with other flame retardants [13].

DOPO (9, 10-dihydro-9-oxa-10-phosphaphenanthrene-10-oxide) derivatives undergo copolymerization with VER during curing, which eliminates the migration problem. In this case, the LOI increases to 28–32% without an increase in viscosity, but a multi-step synthesis procedure is required here [14]. In recent years, the concept of reactive DOPO derivatives has expanded significantly. A liquid flame retardant called VIDOP—a combination of DOPO and 1-vinylimidazole salts—has been proposed, which provides both gas-phase and condensed-phase effects in VER and glass-fiber-reinforced plastics based on it [16]. The ionic liquid VIDHP in carbon fiber/VER composites made it possible to improve fire resistance while maintaining interlaminar strength [17]. A systematic comparison of VIDHP and VIDPP derivatives with different degrees of phosphorus oxidation showed that the oxidation state of P directly determines the balance between gas-phase and condensed-phase mechanisms and the resulting LOI and pHRR values [18]. Grafting DOPO via a flexible aliphatic chain eliminates the embrittlement typical of rigid DOPO-crosslinked networks while preserving the flame-retardant effect [19]. Concurrently, the synthesis of DPPO-containing modifiers via diisocyanate bridges is being developed, which improves the compatibility of the phosphorus fragment with the matrix [20].

Bio-based vinyl ester resins with intrinsic flame resistance have emerged as a distinct and rapidly developing field in recent years. A low-smoke bio-based VER based on magnolol (DBDBMA) with reduced smoke emission and intrinsic flame resistance has been [21]. Bio-based OPBMAR resins based on vanillin with Schiff base moieties, processed via the VARTM method into fiberglass composites [22], and OBBBMA resins based on protocatechuic aldehyde for glass fiber/VER systems [23]; both systems demonstrate enhanced flame resistance without the addition of external flame retardants. Bisphenol A-free VERs based on bisgwayacol have been developed, which simultaneously solves the problem of replacing the toxic monomer [24]. A bio-based P/N-containing flame retardant, HDBMA, based on vanillin, has recently been proposed [17].

For fiber-reinforced VER composites, interfacial and membrane solutions are also being developed: PES/PEPA nanofiber membranes intercalated between layers in CF/VER carbon-plastic composites [25]; the reactive flame retardant ADOTP in combination with carbon fiber [26]; an ionic design of the VER/glass fiber interfacial boundary [27]; a biomimetic "soil–root–mineral" architecture that replicates natural fire-retardant structures [28]. These studies demonstrate that fire protection in composites is increasingly being engineered at the interfacial level, rather than solely within the matrix volume.

Functionalized mesoporous silicon dioxide combines a ceramic fire barrier with encapsulated gas-phase agents, achieving a 35–45% reduction in pHRR at low concentrations while maintaining mechanical properties. The problem is the high cost, which consequently leads to low scalability.

Despite the wide variety of existing fillers with flame-retardant properties, an LOI higher than 30% has not yet been achieved in the VER matrix. A UL-94 V-0 rating was achieved with a filler consisting of DMMP immobilized in diatomite pores. However, the issue of preserving mechanical properties arises in all cases. Understanding the specific mechanisms underlying each factor contributing to the problem is a prerequisite for the rational design of composites. This review presents a comparison of the thermal properties of 10 VER composites made from different fillers, including thermogravimetric analysis (TGA), differential scanning calorimetry (DSC), LOI, and cone calorimetry to identify directions for future research [6], [7].

1.1 Selection criteria for ten representative composite systems

The ten systems under consideration were selected from an extensive body of published literature based on the principle of comprehensively covering the main VER fire protection mechanisms, such that each system represents a distinct class of solutions:

- endothermic cooling and ceramic barrier—Al $(OH)_3$ (ATH) and Mg $(OH)_2$ as standalone mineral hydroxides (the latter with higher-temperature dehydration at 300–360 °C), as well as their synergistic mixture ATH + Mg $(OH)_2$ (2:1), which expands the operating temperature range;
- gas-phase radical inhibition with migration suppression—DE@DMMP, the only example described in the literature of low-molecular-weight phosphonate immobilization that achieved UL-94 V-0 rating;
- intumescent (expanding) mechanism—APP/PER as a reference intumescent system;
- physical expanding barrier—expanding graphite (EG);
- nanobarrier diffusion mechanism—organo-modified montmorillonite (MMT);
- condensed-phase synergy—ZB/ATH, where a glassy borate layer seals the ceramic residue;
- reactive (covalent) phosphorus incorporation without a filler phase—DOPO-MAA;
- hybrid reactive-ceramic approach—mesoporous SiO_2 functionalized with DOPO-silane.

This set of systems covers the entire practically relevant range of loadings (from 5 phr for MMT to 60 phr for ATH and $Mg(OH)_2$), types of interaction with the matrix (physical dispersion—surface-modified filler—immobilized component—covalently incorporated comonomer), and achievable performance metrics (LOI 22.1–31.0%; pHRR 230–420 kW/m²). All systems are described in peer-reviewed sources with reproducible preparation protocols using the same matrix (bisphenol-A vinyl ester resin), which ensures the validity of the comparative analysis and the generalizability of the conclusions to a broader class of fire-resistant VER composites.

2. Methods

All composites are prepared using a commercial bisphenol A-based vinyl ester resin (Derakane 411-350, Ashland Inc., USA): a BADGE/methacrylic acid prepolymer in styrene (~35 wt.%), viscosity 300–500 mPa·s (25 °C), equivalent epoxy weight 190–210 g/eq. Curing system: methyl ethyl ketone peroxide (MEKP, 2 wt.%) as the initiator and cobalt naphthenate (0.2 wt.%) as the accelerator. Curing: 23 °C, 24 h; post-curing: 80 °C, 2 h. The degree of cure was confirmed by DSC (≥95%) for all formulations.

The preparation of composites with hydroxide-based fillers—both Al $(OH)_3$ (ATH) and Mg $(OH)_2$ systems—is carried out according to a standard protocol. The fillers are dried at 120 °C for four hours to remove any adsorbed moisture, then added to VER and mixed in a planetary mill at a speed of 300 rpm for 15 minutes, followed by vacuum degassing at 10–15 mbar. They are then poured into silicone molds and cured at room temperature.

When modifying the surface of aluminum hydroxide, an additional step is required: the aluminum hydroxide particles are treated with a 1% solution of γ-methacryloxypropyltrimethoxysilane in ethanol at 60 °C for one hour, then filtered and dried at 110 °C. This results in more than just physical mixing and covalent bonding. The latter effect is confirmed

by FTIR—the appearance of a Si–O–C band at 1090 cm^{-1}. The modified aluminum hydroxide is then incorporated into the main matrix [9].

Of all ten composites, the preparation of the system with DMMP immobilized in the pores of diatomaceous earth is the most complex, as it involves calcining the diatomaceous earth at 200 °C for four hours to completely remove air from its pore network, followed by the introduction of DMMP into the pores via vacuum impregnation at a pressure below 1 mbar for twelve hours at a DMMP-to-DE mass ratio of 1:2, ensuring complete pore filling without residual bulk DMMP on the surface. The prepared powder was incorporated into the VER matrix by mechanical mixing. FTIR analysis results showed a decrease in the intensity of the P=O and P–O–C bands, and SEM images revealed cross-sections of the particles, which together demonstrate that DMMP penetrated the pores of the diatomite rather than being adsorbed onto the surface [11], [12].

The APP/PER flame-retardant system was prepared by mechanical mixing in a mass ratio of 3:1—optimal for the kinetics of char formation—followed by incorporation into VER via standard mechanical mixing. To prevent premature hydrolysis of the polyphosphate chains, this system was encapsulated in a melamine shell [28].

The preparation of expandable graphite (EG) as a filler requires careful mixing, since rapid mixing can cause destruction even before curing. EG particles are very brittle layered structures; upon destruction, they lose their ability to expand, which is a key factor for fire resistance. Therefore, mixing was performed using a low-shear paddle mixer at 200 rpm for ten minutes. Additionally, vacuum degassing—the next step—is also carried out very carefully to prevent premature expansion of the graphite under reduced pressure [28].

An organic solvent is required to incorporate organoclay or montmorillonite (MMT) filler into VER, as the silicate structure of montmorillonite does not disperse through mechanical mixing. Acetone at a concentration of about 5% is used as the solvent; the swollen clay is then introduced into the resin matrix, and the solvent is removed by vacuum evaporation. A method using a solvent at 60 °C was required to incorporate the organoclay. The intercalation of organoclay was confirmed by X-ray diffraction [13].

Zinc borate (Firebrake ZB, Rio Tinto) was introduced not as a standalone filler, but in combination with aluminum hydroxide (ZB/ATH) to achieve a synergistic mechanism: the former provides endothermic cooling, while zinc borate promotes the formation of a glassy borate layer in the condensed phase, which strengthens and stabilizes the carbon residue. Both powders were dry-mixed prior to addition to the VER and then processed according to the standard mixing protocol [14].

To use DOPO as a flame retardant, DOPO-methacrylamide (DOPO-MAA) is first synthesized by reacting DOPO with acrylamide in toluene at 85 °C for six hours. The compound is then dissolved directly into VER, followed by copolymerization during the curing process. In this process, phosphorus atoms are incorporated as covalent nodes. When introduced into the resin, no filler phase is formed; consequently, the viscosity of the system does not increase. The incorporation as covalent nodes has been confirmed by ^{31}P-NMR spectroscopy [16].

A mesoporous silicon filler system is used in combination with DOPO-silane by functionalizing the latter within the silicon pores. Prior to this, DOPO-silane is grafted in toluene at 110 °C for 24 hours. This approach ensures a more durable fixation of the flame retardant than impregnation, since the formed P–O–Si bonds are hydrolytically stable. The phosphorus content in the functionalized silicon dioxide was confirmed by ICP-OES. The material was incorporated into VER via high-shear mixing, and its large specific surface area (800 m^2/g) facilitated good distribution throughout the matrix [28].

Another flame-retardant system, consisting of a synergistic mixture of aluminum hydroxide and magnesium hydroxide, was prepared by dry mixing in a ratio of 2:1, then added to VER. This ratio was selected based on published optimization data, as it ensures both fire resistance and the preservation of mechanical properties, including a minimal increase in viscosity [8], [9].

The prepared composites were subjected to thermogravimetric analysis (TGA) (ISO 11358, N_2, 10 °C/min, 25–700 °C) and DSC (ISO 11357, N_2, 10 K/min, 2nd heating cycle, 0–200 °C), LOI

evaluation (ASTM D2863/ISO 4589-2), and cone calorimetry (ISO 5660-1, heat flux 50 W/m², horizontal orientation). All formulations were tested for vertical burning according to UL-94 (IEC 60695-11-10), and their mechanical properties were determined (ISO 527, tensile strength; ISO 178, flexural strength).

3. Discussion

3.1 Thermogravimetric analysis (TGA)

Figure 1 shows the results of TGA curve measurements for pure VER and VER-based composites with various fillers in a nitrogen atmosphere. Pure VER exhibits a two-stage decomposition: an initial stage at ~298 °C (T5% ≈ 290 °C), with the main peak occurring at approximately 355 °C, corresponding to the breakage of styrene chains, during which volatile substances are released, followed by secondary decomposition at 380–500 °C. The carbon residue at 700 °C is 2%, indicating the extremely low fire resistance of the pure sample [3], [7], [20].

Upon the introduction of aluminum hydroxide, an additional endothermic step appears at 200–250 °C, corresponding to the dehydration of aluminum hydroxide, or at 300–360 °C—magnesium hydroxide, which is clearly visible on the shoulder. This requires 1050–1300 J/g, which contributes to effective cooling of the material during ignition. Fillers contribute to a shift in the onset of decomposition by 17–24 °C. This occurs because fillers create barriers to the diffusion of volatile components, thereby limiting the mobility of polymer chains. The carbon residue at 700 °C increases to 33–38%, which closely corresponds to the theoretical content of oxides (Al_2O_3 or MgO) [7], [8].

Pure magnesium hydroxide (60 phr) exhibits the highest decomposition onset temperature among hydroxide systems: since its dehydration occurs at 300–360 °C and does not precede the decomposition of the matrix, T_5% increases to 318 °C (+28 °C compared to pure VER), and the carbon residue (MgO) at 700 °C is ≈34%. In terms of cooling efficiency, $Mg(OH)_2$ is similar to ATH; however, its higher-temperature dehydration is better aligned with the main decomposition stage of VER (≈355 °C), which accounts for the composite's slightly higher thermal stability [8], [9], [10].

The DE@DMMP system (25% by weight) shows a more modest improvement: the ignition temperature shifts by only ~7 °C, and the carbon residue content increases to ~12%. However, the porous DE support hinders DMMP migration, ensuring sustained suppression of gas-phase combustion throughout the material's service life—which is a significant advantage over DMMP systems obtained by physical mixing [29], [12].

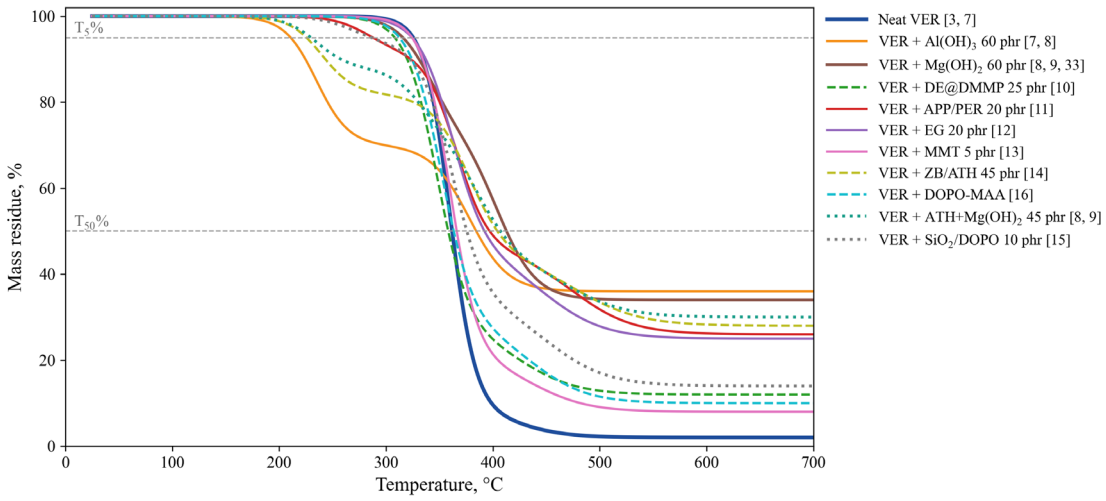

Figure 2 – TGA curves of neat VER and VER composites with different filler types (N_2, 10°C/min)[2], [3], [7], [8], [9], [10], [13], [14], [16], [29], [30], [31]

The TGA profile of the APP/PER filler showed that decomposition occurs in four stages (Figure 2): mass loss at 250–300 °C (about 8%), which corresponds to the precipitation of

polyphosphoric acid; at 350–480 °C, this is the combustion of the graphitized carbon residue; and at 500–600 °C, this reflects the combustion of the partially graphitized layer of the carbon residue. Compared to the pure sample, the decomposition onset temperature is shifted by 12°C, which is an effective indicator and indicates the formation of a carbon residue [28].

In expanding graphite, no significant decomposition is observed below 300 °C due to the chemical inertness of the material. Already upon heating above 300 °C, graphite begins to expand, forming layers that slow heat transfer to the polymer matrix. The 5% decomposition point shifts by +10 °C to 308°C, and the carbon residue at 700 °C reaches 25%. This is the highest value among carbon fillers [20].

Nanoclay has a negligible effect on mass loss and the decomposition onset temperature. (T5%) increases by only +4 °C, but the mass loss rate decreases by 18% compared to pure VER. The silicate plates hinder the volatilization of volatile products. The carbon residue is 8%, which is also a negligible value; the increase in LOI in this system is also negligible [13].

The ATH+Mg $(OH)_2$ system exhibits the following TGA profile: an ATH shoulder at 200–250 °C and a broad $Mg(OH)_2$ peak at 300–360 °C. The amount of heat absorbed is slightly lower than in the composite with a single filler (by 950–1100 J/g; T5% = 316 °C (+18 °C compared to pure VER), carbon residue 30%), which confirms the high degree of filler retention [8], [9].

The DOPO-MAA reactive system does not form a discrete filler phase; accordingly, its TGA curve lacks an additional mass loss step at temperatures below 300 °C. Covalently bound phosphorus atoms act in the gas phase, releasing PO• radicals, which capture H• and OH• chain carriers during thermal decomposition. This leads to a moderate increase in T5% to 306 °C (+8 °C) and the formation of a carbon residue of approximately 10%, which is higher than that of pure VER but lower than that of systems with a mineral filler. The main advantage of DOPO-MAA, according to TGA data, is the complete absence of a premature dehydration stage, which hinders the high-temperature processing of hydroxide-filled systems[2], [16]. Similar behavior is also characteristic of new-generation DOPO derivatives with flexible aliphatic side chains, for which a smoother curve is additionally observed in the 250–320 °C range [19].

Functionalized mesoporous SiO_2/DOPO-silane (10 phr) exhibits a TGA profile intermediate between those of the DOPO reactive system and composites with inorganic fillers. A slight mass loss in the 250–280 °C range is due to the decomposition of residual organic surface groups on the silica. The ceramic SiO_2 matrix persists up to 700 °C, accounting for approximately 9% of the carbon residue (total carbon = 14%). T5% = 309 °C (+11 °C). The high specific surface area of the carrier (800 m^2/g) ensures uniform distribution of phosphorus centers throughout the matrix, resulting in a more homogeneous TGA curve without the sharp dehydration shoulder characteristic of hydroxide fillers [15].

The zinc borate filler in aluminum hydroxide retains the endothermic dehydration feature of ATH at 200–250 °C, while a glassy layer forms on the surface of the carbon residue starting at 410 °C. T5% = 312 °C (+14 °C) and a carbon residue of 28% at 700 °C. The glassy residue with a high ZnO/B_2O_3 content seals cracks in the Al_2O_3 layer, thereby limiting oxygen access—a result not achieved when using the fillers separately [14].

3.2 Differential scanning calorimetry (DSC)

Analysis of the DSC curves for all samples revealed significant differences in glass transition temperatures (Tg) and changes in heat capacity (ΔCp).

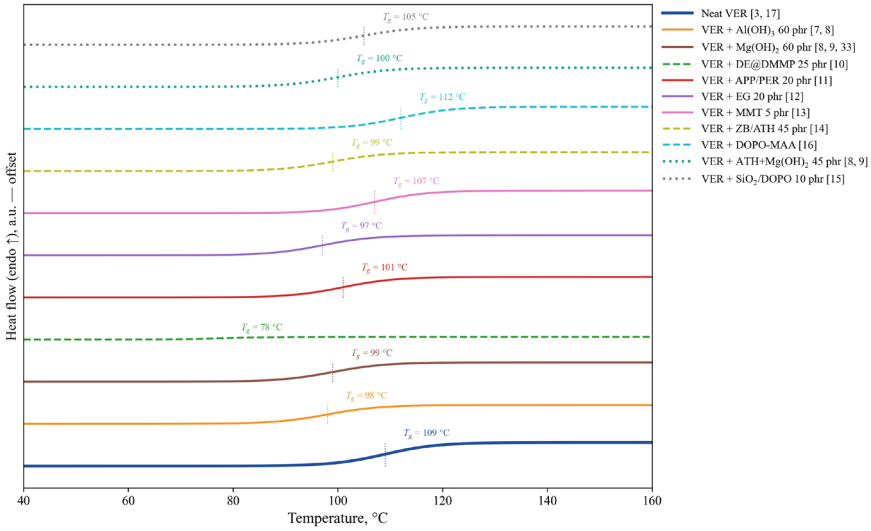

Figure 3 – DSC curves of neat VER and VER composites (2nd heating cycle, N_2, 10 K/min) [3], [7], [8], [9], [10], [13], [14], [16], [32], [10]

The pure VER sample exhibited the highest values of Tg(max) = 109 °C and ΔCp = 0.135 J/g·K. Following the pure sample, the MMT-based composite exhibited Tg = 107 °C and ΔCp = 0.130 J/g·K, attributed to its low concentration and a purely physical fire-retardant mechanism.

The remaining composites demonstrated the following values: Al $(OH)_3$ – 98 °C, EG - 97 °C, ZB/ATH - 99 °C, ATH+$Mg(OH)_2$ - 100 °C, APP/PER - 101 °C, and SiO_2/DOPO - 105 °C, with ΔCp values in the range of 0.105–0.118 J/g·K. The smallest decrease in Tg is observed for DE@DMMP (-78 °C, ΔCp = 0.016 J/g·K), associated with the effective immobilization of DMMP in the diatomite pores, which limits the mobility of the polymer matrix chains.

In contrast, DOPO-MAA significantly increases Tg(max) (112 °C, ΔCp = 0.128 J/g·K). DSC data confirm that reactively incorporated fillers prevent a decrease in Tg, whereas all particle-based systems lower Tg to some extent depending on the loading and interfacial compatibility. The following Table 1 shows the key DSC parameters for all systems.

Table 1 – DSC parameters of neat VER and VER composites (2nd heating cycle, N_2, 10 K/min) [3], [7], [8], [9], [10], [11], [13], [14], [15], [16], [20], [28], [29], [30], [31], [32]

System	Tg(max), °C	ΔCp, J/g·K
Neat VER	109	0.135
VER + Al $(OH)_3$ 60 phr	98	0.108
VER + Mg $(OH)_2$ 60 phr	99	0.111
VER + DE@DMMP 25 phr	78	0.016
VER + APP/PER 20 phr	101	0.118
VER + EG 20 phr	97	0.115
VER + MMT 5 phr	107	0.130
VER + ZB/ATH 45 phr	99	0.109
VER + DOPO-MAA	112	0.128
VER + ATH+$Mg(OH)_2$ 45 phr	100	0.110
VER + SiO_2/DOPO 10 phr	105	0.105

3.3 Limiting oxygen index (LOI) and cone calorimetry

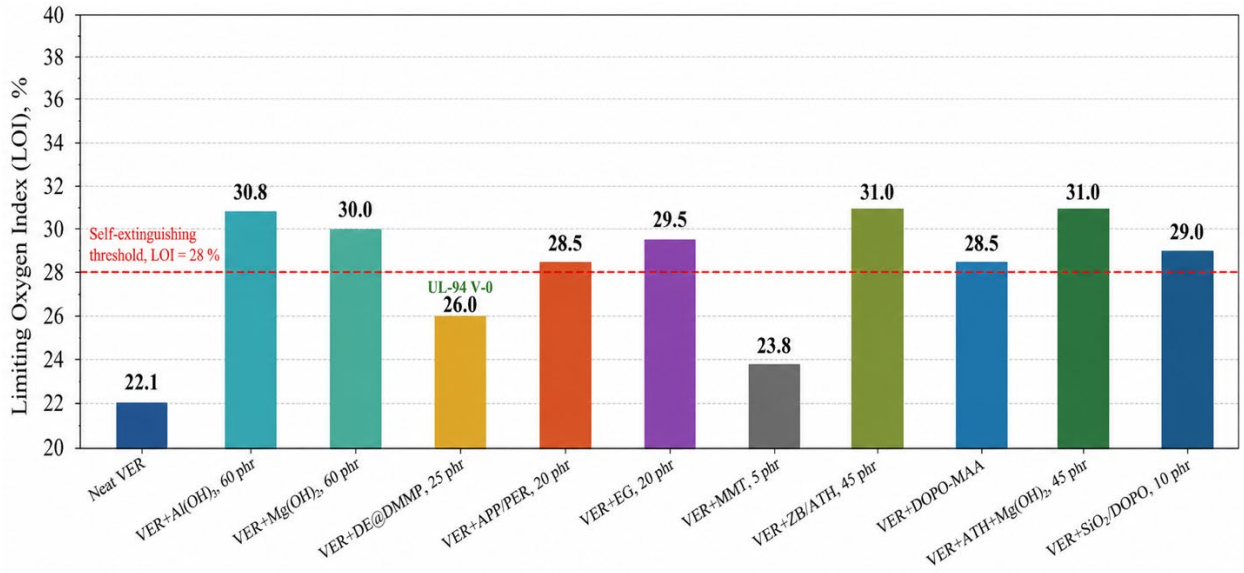

Figure 4 – LOI values of VER composite systems [7], [8], [9], [10], [12], [13], [29], [30]

Among all composite systems, the highest LOI is exhibited by VER composites containing aluminum hydroxide and magnesium hydroxide (LOI = 31%), as well as those containing zinc borate (LOI = 31%). The LOI of the composite filled solely with aluminum hydroxide is close to this value. Next, in descending order of LOI, are the following composites: VER+EG, VER+SiO_2/DOPO, VER+APP/PER, and VER+DOPO-MAA.

VER+MMT and DE@DMMP slightly increase the LOI compared to the pure sample, reaching 23.8 and 26, respectively [20]. Calorimetry is a powerful tool for assessing a material's fire resistance and fire safety. The following Table 2 shows the measured characteristics.

Table 2 – Cone calorimetry data for neat VER and VER composites (50 kW/m² heat flux)

System	TTI, s	pHRR, kW/m²	ΔpHRR	THR, MJ/m²	Ref.
Neat VER	28	420	—	95	[3], [7]
VER + $Al(OH)_3$ 60 phr	48	230	−45%	60	[7], [8]
VER + $Mg(OH)_2$ 60 phr	45	245	−42 %	61	[8], [9], [10]
VER + DE@DMMP 25 phr	36	310	−26%	78	[12]
VER + APP/PER 20 phr	40	270	−36%	72	[29]
VER + EG 20 phr	42	260	−38%	68	[30]
VER + MMT 5 phr	33	295	−30%	82	[13]
VER + ZB/ATH 45 phr	44	250	−40%	63	[14]
VER + DOPO-MAA	31	330	−21%	79	[2], [16], [31]
VER + ATH+$Mg(OH)_2$ 45 phr	46	240	−43%	62	[8], [9]
VER + SiO_2/DOPO 10 phr	38	275	−35%	74	[16]

The heat release rate (pHRR) of pure VER is reported to be 420 W/m²; the total heat release (THR) is ~95 MJ/m² [3], [7]. The ignition time is approximately 28 seconds.

The best performance was recorded for the composite with aluminum hydroxide: pHRR decreases to 230 kW/m² and the ignition time increases to 48 s. Aluminum oxide serves as the diffusion barrier in the condensed phase [7], [8]. Similar results were also observed for the system combining aluminum hydroxide and magnesium hydroxide. Similar results were obtained for Mg $(OH)_2$ alone (pHRR = 245 kW/m²) and for a system combining aluminum and magnesium hydroxides. The VER + DOPO-MAA system exhibited a pHRR of 330 kW/m² and an ignition time of 31 s, which is the lowest value among all 10 proposed components. The values correspond to the data in Tables 1 and 2; for the carbon residue of the APP/PER system, an estimate based on the TGA curve (Figure 2) is provided.

3.4. Comprehensive multi-parameter comparison of systems

To simultaneously evaluate the improvement in fire resistance and its "cost" in terms of changes in thermomechanical properties, Table 3 and Figure 5 summarize the key performance indicators for all ten systems: LOI, pHRR, time to ignition, THR, Tg, carbon residue at 700 °C, and the decomposition onset temperature T_5%.

Table 3 — Summary of a multi-parameter comparison of the fire-resistant and thermal characteristics of ten VER systems [3], [7], [8], [9], [10], [12], [13], [14], [16], [29], [30], [31], [32]

System	LOI, %	pHRR, kW/m² (ΔpHRR)	TTI, c	Tg, °C	Residue at 700 °C, %	T_5%, °C
Neat VER	22.1	420 (—)	28	109	2	290
VER + $Al(OH)_3$ 60 phr	30.8	230 (−45 %)	48	98	33–38	307–314
VER + $Mg(OH)_2$ 60 phr	30.0	245 (−42 %)	45	99	34	318
VER + DE@DMMP 25 phr	50.0	310 (−26 %)	36	78	~12	297
VER + APP/PER 20 phr	28.5	270 (−36 %)	40	101	~26	302
VER + EG 20 phr	29.5	260 (−38 %)	42	97	25	308
VER + MMT 5 phr	23.8	295 (−30 %)	33	107	8	294
VER + ZB/ATH 45 phr	31.0	250 (−40 %)	44	99	28	312
VER + DOPO-MAA	28.5	330 (−21 %)	31	112	~10	306
VER + ATH+$Mg(OH)_2$ 45 phr	31.0	240 (−43 %)	46	100	30	316
VER + SiO_2/DOPO 10 phr	29.0	275 (−35 %)	38	105	14	309

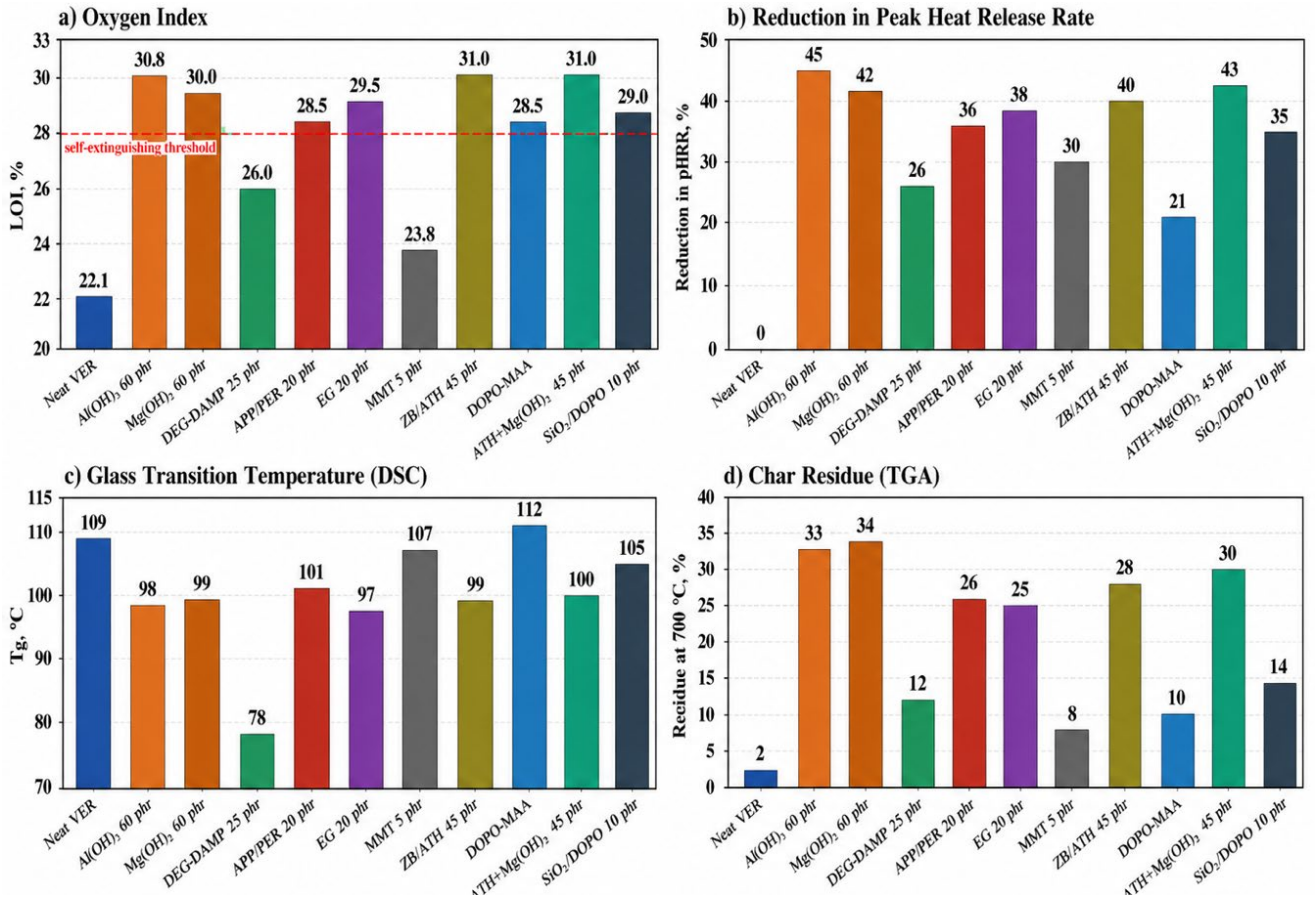

Figure 5 – Multiparameter comparison of ten VER systems: a) LOI; b) pHRR reduction; c) glass transition temperature; d) carbon residue at 700 °C (based on data from Tables 1–3; ([3], [7], [8], [9], [10], [12], [13], [14], [16], [10], [32] [17], [33])

Tables 3 and Figure 5 show that no single system achieves maximum values for all parameters simultaneously. Hydroxide systems (ATH, $Mg(OH)_2$, ATH + $Mg(OH)_2$, ZB/ATH) lead in terms of LOI, reduction in pHRR, and time to ignition, but "pay" for this with a 9–11 °C decrease in Tg and a high loading (45–60 phr). The reactive DOPO-MAA system is the only one that increases Tg (up to 112 °C), but it results in the smallest reduction in pHRR (−21%). DE@DMMP—the only system with a UL-94 V-0 rating—is characterized by the most pronounced decrease in Tg (down to 78 °C), due to the residual plasticizing effect of the phosphonate. These trade-offs quantitatively illustrate the thesis formulated in the introduction regarding the need for a rational choice of filler tailored to specific operational requirements.

3.5 Critical analysis of discrepancies in published data

The values of thermal and combustion parameters reported by different authors for nominally identical systems often differ. An analysis of the primary sources reveals six main reasons for these discrepancies.

First, for systems containing ATH, published LOI values range from ~28 to 35%, depending on (a) the shape and size of the particles (micro- and nanoscale ATH form Al_2O_3 barriers with varying degrees of continuity), (b) the presence of silane surface treatment, which increases the LOI by 1–2% due to improved adhesion and uniformity of distribution [9], and (c) the total loading: at 60 phr, the LOI is 2–3% higher than at 40 phr [7], [8]. Therefore, a direct comparison of LOI values without considering particle shape and loading is incorrect.

Second, for VER + MMT nanocomposites, the reported values for pHRR reduction fall within a wide range of 25–40%, which is determined primarily by the degree of clay exfoliation: effective exfoliation (confirmed by the shift of the d(001) peak in the X-ray diffraction pattern) determines the upper limit of the range, whereas aggregated tactoid structures determine the lower limit [13]. The shear mixing method and the choice of solvent are critical.

Third, for DOPO derivatives, LOI values in the literature range from 26 to 32% and depend significantly on the structure of the modifier: the degree of DOPO substitution, the presence of a nitrogen-containing moiety (imidazolium salts VIDOP, VIDHP), and the form of introduction (monomer for copolymerization or prepolymer) [2], [14], [16], [18], [19]. A systematic comparison of derivatives with different degrees of phosphorus oxidation[18] showed that P(+V) forms shift the reaction to the condensed phase (higher coke yield), whereas P(−I)/P(+III) forms are more effective in the gas phase; this, in particular, explains the discrepancies in pHRR values for systems with similar compositions.

Fourth, the differences in Tg values are explained by the different nature of the "phosphorus–matrix" bond: physically incorporated DMMP acts as a plasticizer and lowers Tg by 25–30 °C, whereas covalently bound DOPO-MAA does not lower Tg (or slightly increases it due to an increase in crosslinking density), while immobilized DE@DMMP occupies an intermediate position, since immobilization only partially eliminates plasticization [12], [16].

Fifth, for APP/PER intumescent systems, char yield and LOI are sensitive to the APP:PER ratio (optimum 3:1) and to moisture protection: without melamine encapsulation, exposure to high humidity leads to partial hydrolysis of the polyphosphate and a noticeable loss of effectiveness [29], [15]. Differences in the conditioning history of the samples are a common cause of discrepancies in data from different laboratories.

Sixth, the time to ignition and pHRR systematically depend on the calorimetry conditions (heat flux of 35/50/75 kW/m², sample orientation, plate thickness); therefore, absolute values from different studies are comparable only after being normalized to identical test conditions. In this review, all calorimetry data are reported for 50 kW/m² and horizontal orientation (ISO 5660-1).

Thus, in most cases, the observed discrepancies do not reflect inconsistencies in the data but rather differences in filler morphology, method of incorporation, loading, conditioning, and test conditions. This is precisely why Table 3 lists the sources of each value, and the comparison of systems is based on data obtained under comparable conditions.

4. Practical aspects and prospects for further research

4.1 Economic feasibility

The cost of the fire-retardant systems discussed varies by an order of magnitude. Mineral hydroxides (ATH, Mg $(OH)_2$) are the least expensive large-volume flame retardants, making them the preferred choice for mass-production structural applications (construction profiles, ship panels, containers), despite the high loading levels required. APP/PER systems and intumescent graphite occupy the mid-price segment at moderate loading levels (20 phr). The most expensive are reactive DOPO derivatives (multi-stage synthesis) and functionalized mesoporous SiO_2 (sol-gel synthesis of the carrier and grafting of DOPO silane in toluene), which currently limits their use to niche, mission-critical applications—aviation, electronics, and transportation [31]. DE@DMMP occupies an intermediate position: both diatomite and DMMP are inexpensive industrial products, and the main cost comes from the vacuum impregnation stage [12]. Simplifying the synthesis of reactive phosphorus-containing modifiers—for example, single-step schemes based on diisocyanate bridges [30] — is an important means of reducing costs.

4.2 Scalability of synthesis

Technologies for producing composites with mineral fillers (ATH, Mg $(OH)_2$, ZB/ATH) are fully compatible with existing mixing and casting equipment and can be scaled up without restrictions; the only limiting factor remains the increase in viscosity at high loading levels. Bio-based VERs with intrinsic flame resistance (OPBMAR, OBBBMA, HDBMA) have already been processed using VARTM methods into fiberglass composites on a laboratory and pilot scale, demonstrating their compatibility with industrial infusion technologies [22], [23], [33]. The interlayer incorporation of PES/PEPA nanofiber membranes requires an additional step during layup but is compatible with automated processes for the production of layered composites [25]. The most critical processes for scaling up are the multi-stage processes—vacuum impregnation of DMMP into diatomite and the functionalization of mesoporous SiO_2 with DOPO-silane; optimizing these process parameters (reducing impregnation time, replacing toluene with safer solvents) remains a priority engineering task [12], [31].

4.3 Industrial applicability and environmental requirements

The choice of system is determined by the application. For construction and shipbuilding products, where cost and smoke emission are critical factors, hydroxide systems and their combinations with zinc borate are the most suitable. For electrical and transportation applications, where binder viscosity during fiber impregnation and the preservation of Tg are critical, reactive DOPO/DPPO modifiers and ionic interfacial solutions are preferred [17], [20], [27]. Tighter environmental regulations (REACH and similar regulations) restricting halogenated flame retardants and bisphenol A make bio-based VERs derived from magnolol, vanillin, protocatechuic aldehyde, and bisgwayacol strategically important [17], [21], [22], [23], [24]: they simultaneously eliminate toxic monomers and provide intrinsic flame resistance without additive migration. Biomimetic architectures [29] suggest the potential for further efficiency gains while maintaining environmental sustainability. Over the next 3–5 years, the following appear to be the most realistic candidates for industrial implementation: (i) surface-modified ATH/Mg $(OH)_2$ hybrids; (ii) bio-based VERs with incorporated phosphorus and nitrogen; (iii) reactive DOPO derivatives with flexible interconnections for fiber-reinforced structures.

4.4 Research priorities

From a scientific standpoint, the three areas outlined in the introduction remain key: the systematic extension of silane functionalization to $Mg(OH)_2$ and hybrid mixtures; the development of new "phosphorus compound–porous support" pairs, analogous to DE@ DMMP (including those based on mesoporous SiO_2) to overcome the self-extinguishing threshold at low loading levels; and the combination of reactive DOPO/VIDHP chemistry with moderate amounts of mineral fillers to simultaneously achieve LOI > 31%, UL-94 V-0 classification, and maintain Tg ≥ 100 °C. To these should be added a fourth direction identified in the analysis of the 2022–2026 literature: the design of fire protection at the fiber–

matrix interface (ionic interactions, nanofiber interlayers, biomimetic structures), which allows for combining fire resistance with an increase—rather than a decrease—in mechanical properties[17], [18], [25], [27], [28].

5. Conclusions

This review examines VER-based composite systems, the primary function of which is to enhance the fire resistance and other thermal properties of the host matrix while only slightly altering the mechanical properties inherent to VER. Physical testing methods such as TGA, DSC, LOI, and cone calorimetry allow for an assessment of the increase in the fire resistance of composites upon the introduction of a particular filler.

Among all the systems considered, an aluminum hydroxide-based filler stands out, having demonstrated both a high LOI and effective cone calorimetry characteristics.

In cases where high operating temperatures or technological constraints limit the ATH content, a synergistic blend of ATH and Mg $(OH)_2$ with a total content of 45 phr becomes an important practical alternative. Phosphorus-based fillers, such as the DE@DMMP system, achieve UL-94 V-0 rating—a result that hydroxide-based systems can only achieve at much higher concentrations—while maintaining moderate viscosity and mechanical loss values. A limitation is an LOI of 50%, so DE@DMMP is best used in combination.

APP with pentaerythritol achieves an LOI threshold of 28% or higher at a lower loading than hydroxide-based systems and represents the most mechanically favorable route to self-extinguishing properties when moisture resistance requirements are not stringent; new-generation reactive APP derivatives [15] also overcome this limitation. Montmorillonite's fire resistance mechanism is achieved through physical barrier methods, and its ability to reduce pHRR by 30–40% is due to its effective synergistic component in combination with primary flame retardants.

Although DOPO derivatives do not exhibit effective thermal properties, they offer a significant advantage: no loss of viscosity and the absence of a "particle-matrix" interface, which makes them attractive for use in fiber-reinforced materials. Recent studies on VIDOP, VIDHP/VIDPP, and DOPO with flexible crosslinks [16], [17], [18], [19], as well as bio-based VERs with inherent flame resistance [21], [22], [23], [33] confirm that reactive phosphorus chemistry can bridge the gap between the V-2 and V-0 categories without compromising processability.

A recurring pattern is observed in all ten systems: fire safety metrics – LOI, pHRR, and UL-94 rating – do not always improve simultaneously. A system can achieve a V-0 rating while remaining below the LOI self-extinguishing threshold, as demonstrated by the DE@DMMP example, since these two tests evaluate different aspects of combustion behavior: LOI measures flame spread under steady-state conditions, while UL-94 assesses the tendency toward self-extinguishing after the ignition source is removed. Therefore, presenting a single indicator as representative of fire safety is insufficient, and future work should regularly combine these complementary characteristics. The results of this review are useful for research and development of a new generation of fire-safe VER composites.

Acknowledgments

This work was supported by the Science Committee of the Ministry of Science and Higher Education of the Republic of Kazakhstan (Grant No. BR28712729).

References

[1] J.-P. Pascault, *Epoxy polymers: new materials and innovations*. Weinheim: Wiley-VCH, 2010.

[2] Y.-Z. Zhao, Y. Chu, Y.-J. Xu, P. Zhu, and Y.-Z. Wang, 'Highly flame-retardant vinyl ester resins with well-balanced comprehensive performance', *Chem. Eng. J.*, vol. 464, p. 142659, May 2023, doi: 10.1016/j.cej.2023.142659.

[3] A. P. Mouritz and A. G. Gibson, *Fire properties of polymer composite materials*. in Solid mechanics and its applications, no. v. 143. Dordrecht: Springer, 2006.

[4] X. Zhang *et al.*, 'Effect of diluent on the properties of intrinsically flame-retardant vinyl ester resins and their fiberglass-reinforced composites', *Compos. Commun.*, vol. 37, p. 101441, Jan. 2023, doi: 10.1016/j.coco.2022.101441.

[5] E. D. Weil and S. V. Levchik, *Flame retardants for plastics and textiles: practical applications*. Cincinnati: Hanser Publications, 2009.
[6] B. Liu, H. Zhao, and Y. Wang, 'Advanced Flame-Retardant Methods for Polymeric Materials', *Adv. Mater.*, vol. 34, no. 46, p. 2107905, Nov. 2022, doi: 10.1002/adma.202107905.
[7] P. R. Hornsby, 'Fire retardant fillers for polymers', *Int. Mater. Rev.*, vol. 46, no. 4, pp. 199–210, Apr. 2001, doi: 10.1179/095066001771048763.
[8] F. Laoutid, L. Bonnaud, M. Alexandre, J.-M. Lopez-Cuesta, and Ph. Dubois, 'New prospects in flame retardant polymer materials: From fundamentals to nanocomposites', *Mater. Sci. Eng. R Rep.*, vol. 63, no. 3, pp. 100–125, Jan. 2009, doi: 10.1016/j.mser.2008.09.002.
[9] C. DeArmitt and M. Hancock, 'Particulate-Filled Polymer Composites', 2003, pp. 357–424.
[10] B. K. Kandola and W. Pornwannachai, 'Enhancement of Passive Fire Protection Ability of Inorganic Fire Retardants in Vinyl Ester Resin Using Glass Frit Synergists', *J. Fire Sci.*, vol. 28, no. 4, pp. 357–381, Jul. 2010, doi: 10.1177/0734904109361015.
[11] J. Xie *et al.*, 'Boosting the flame retardancy of vinyl ester resins via a DE@DMMP hybrid: Reducing migration and improving fire performance', *Polym. Degrad. Stab.*, vol. 246, p. 111963, Apr. 2026, doi: 10.1016/j.polymdegradstab.2026.111963.
[12] J. Xie, A. Marzhan, Z. Nurgul, Y. Hou, B. Amirbek, and others, 'Boosting the flame retardancy of vinyl ester resins via a DE@DMMP hybrid: Reducing migration and improving fire performance', *Polym. Degrad. Stab.*, p. 112127, 2026, [Online]. Available: https://www.sciencedirect.com/science/article/pii/S0141391026000443
[13] G. Ji and G. Li, 'Effects of nanoclay morphology on the mechanical, thermal, and fire-retardant properties of vinyl ester based nanocomposite', *Mater. Sci. Eng. A*, vol. 498, no. 1–2, pp. 327–334, Dec. 2008, doi: 10.1016/j.msea.2008.08.003.
[14] B. Ari, A. N. Y. Yilmaz, and A. C. Bedeloglu, 'Flame retardancy and mechanical effects of ZnB and ATH additives in glass fiber-reinforced polyester composites', *J. Mater. Sci. Polym.*, vol. 1, no. 1, p. 9, Mar. 2026, doi: 10.1007/s44493-026-00013-6.
[15] T. Chu *et al.*, 'Dual enhancement of flame retardancy and mechanical performance of vinyl ester resin composite via reactive ammonium polyphosphate', *Compos. Part B Eng.*, 2026, [Online]. Available: https://www.sciencedirect.com/science/article/pii/S135983682600185X
[16] F.-Q. Zhang, Y.-Z. Zhao, Y.-J. Xu, Y. Liu, and P. Zhu, 'Flame retardation of vinyl ester resins and their glass fiber reinforced composites via liquid DOPO-containing 1-vinylimidazole salts', *Compos. Part B Eng.*, vol. 234, p. 109697, Apr. 2022, doi: 10.1016/j.compositesb.2022.109697.
[17] Z. Zhang, X. Bi, W. Zhang, and R. Yang, 'Phosphorus/nitrogen-containing vinyl imidazolium ionic liquid for improving flame retardancy and mechanical properties of vinyl ester resin, and its carbon fiber composites', *Compos. Part Appl. Sci. Manuf.*, 2024, [Online]. Available: https://www.sciencedirect.com/science/article/pii/S1359835X24000897
[18] Y. Y. Yin, Y. Z. Zhao, X. W. Jia, F. Q. Zhang, Y. J. Xu, and others, 'Flame-retardant vinyl ester resins enabled by phosphorus-containing 1-vinylimidazole salts with different phosphorus oxidation states', *J. Mater. Sci. Technol.*, 2025, [Online]. Available: https://www.sciencedirect.com/science/article/pii/S100503022400450X
[19] L. Duan, S. Yang, J. Wang, K. Chen, and others, 'Synergistic enhancement of flame retardancy and mechanical properties in vinyl ester resins via DOPO-based flexible chain grafting modification', *J. Appl. Polym. Sci.*, p. e70797, 2026, doi: 10.1002/app.70797.
[20] K. Chen, J. Wang, L. Duan, S. Yang, X. Chen, and others, 'Intrinsic flame retardancy and enhanced properties of vinyl ester resins grafted with diphenylphosphine oxide via various diisocyanates', *Chem. Eng. J.*, p. 174317, 2026, [Online]. Available: https://www.sciencedirect.com/science/article/pii/S1385894726017766
[21] X. Zhang, W. Zhang, Y.-T. Pan, L. Qian, Z. Qin, and W. Zhang, 'Synthesis and performance of intrinsically flame-retardant, low-smoke biobased vinyl ester resin', *React. Funct. Polym.*, 2022, [Online]. Available: https://www.sciencedirect.com/science/article/pii/S1381514821003503
[22] X. Zhang, J. Wu, Z. Qin, Y.-T. Pan, Z. Geng, and X. Wu, 'Intrinsic flame-retardant vinyl ester resin and its fiberglass-reinforced composite with excellent comprehensive properties by structural design', *Polym. Degrad. Stab.*, vol. 218, p. 110560, 2023, [Online]. Available: https://www.sciencedirect.com/science/article/pii/S0141391023003117
[23] X. Zhang and others, 'Bio-based OBBBMA (protocatechualdehyde) for flame-retardant GF/VER composites', *Polym. Degrad. Stab.*, vol. 207, p. 110209, 2023.
[24] A. Etiennot and others, 'Lignin-derived bisguaiacol vinyl ester as a bisphenol A-free resin alternative', *Commun. Mater.*, vol. 6, p. 105, 2025, doi: 10.1038/s43246-025-00826-y.
[25] M. Yu *et al.*, 'Integrated design of flame retardancy, smoke suppression and structure of carbon fiber reinforced vinyl ester resin composites through intercalation of nanofiber membrane', *Compos. Struct.*, 2024, [Online]. Available: https://www.sciencedirect.com/science/article/pii/S0263822324006597
[26] B. Liu, M. Zhao, H. Cao, J. Sun, Y. Gao, and Y. Xing, 'Synergistic flame retardancy and mechanical enhancement of vinyl ester resin via chemically bonded ADOTP and carbon fiber reinforcement', *Polym. Compos.*, 2026, doi: 10.1002/pc.70546.

[27] J. N. Wang, F. Q. Zhang, Z. Q. Dong, and Y. J. Xu, 'Ionic interfacial design for high-performance flame-retardant vinyl ester resin/glass fiber composites', *Polymer*, p. 129775, 2026, [Online]. Available: https://www.sciencedirect.com/science/article/pii/S0032386126002223
[28] Y. M. Li, H. P. Fang, S. L. Hu, Y. Deng, and D. Y. Wang, 'Biomimetic soil-root-mineral system toward VER composites with enhanced mechanical property, good recyclability and excellent flame retardancy', *Polym. Degrad. Stab.*, p. 111943, 2026, [Online]. Available: https://www.sciencedirect.com/science/article/pii/S0141391026000248
[29] L. Liu, Y. Xu, M. Xu, Y. He, S. Li, and B. Li, 'An efficient synergistic system for simultaneously enhancing the fire retardancy, moisture resistance and electrical insulation performance of unsaturated polyester resins', *Mater. Des.*, vol. 187, p. 108302, Feb. 2020, doi: 10.1016/j.matdes.2019.108302.
[30] Y.-F. Shih, Y.-T. Wang, R.-J. Jeng, and K.-M. Wei, 'Expandable graphite systems for phosphorus-containing unsaturated polyesters. I. Enhanced thermal properties and flame retardancy', *Polym. Degrad. Stab.*, vol. 86, no. 2, pp. 339–348, Nov. 2004, doi: 10.1016/j.polymdegradstab.2004.04.020.
[31] X. Qiu, Z. Li, V. Chevali, P. Song, X. Li, and Z. Zhang, 'Functionalized Mesoporous Silica Fire Retardant via Hierarchical Assembly for Improved Fire Retardancy of Unsaturated Polyester', *ACS Appl. Polym. Mater.*, vol. 5, no. 3, pp. 2203–2212, Mar. 2023, doi: 10.1021/acsapm.2c02195.
[32] J. Thomason and G. Xypolias, 'Investigation of the effects of scale and cure environment on the properties of vinyl ester polymer', *Polymer*, vol. 307, p. 127344, Jul. 2024, doi: 10.1016/j.polymer.2024.127344.
[33] J. Zhang, X. Xu, Z. Zhang, Z. Qin, Y. Zhao, and others, 'A phosphorus-nitrogen synergistic bio-based monomer imparts intrinsic flame retardancy and smoke suppression to vinyl ester composites', *J. Appl. Polym. Sci.*, p. e70373, 2026, doi: 10.1002/app.70373.

Information about authors:
Marzhan Akhmetova – Senior lecturer of the Department of Physics of K. Zhubanov Aktobe Regional University, Aktobe, Kazakhstan;
Nurgul Zhanturina – PhD, Dr, Associate Professor of the Department of Physics, K. Zhubanov Aktobe Regional University, Aktobe, Kazakhstan, nzhanturina@zhubanov.edu.kz
Abish Taskaliyev – Senior lecturer of the Department of Physics of K. Zhubanov Aktobe Regional University, Aktobe, Kazakhstan; ataskaliyev@zhubanov.edu.kz
Amirbek Bekeshev – Candidate of Physical and Mathematical Sciences, Dr, Associate Professor of the Department of Physics, K. Zhubanov Aktobe Regional University, Aktobe, Kazakhstan, amirbek2401@gmail.com

Author Contributions:
Marzhan Akhmetova – concept, methodology, resources, data collection, testing, visualization, drafting, editing
Nurgul Zhanturina – concept, modeling, analysis, interpretation,
Abish Taskaliyev –data collection, testing, visualization, editing
Amirbek Bekeshev – concept, methodology, drafting, editing, funding acquisition.

Conflict of Interest: The authors declare no conflict of interest.

Use of Artificial Intelligence (AI): The authors declare that AI was not used.

Received: 08.05.2026
Revised: 20.06.2026
Accepted: 24.06.2026
Published: 29.06.2026

Technobius Physics, 2026, 4(2), 0055, DOI: https://doi.org/10.54355/tbusphys/30070147.4.2.2026.0055

Technobius Physics

https://technobiusphysics.kz/

e-ISSN 3007-0147

Article

Tailoring oxygen-vacancy concentration in Ga_2O_3 thin films through controlled post-annealing: Experimental correlation between defect chemistry, carrier transport, and dielectric response

Ruslan Kalibek[1], Daria Sopyryaeva[2]

[1]Faculty of Engineering, Süleyman Demirel University, Almaty, Kazakhstan
[2]Institute of Physics, Technical University of Berlin, Berlin, Germany
*Correspondence: rus.kalibek@bk.ru

Abstract. The control of oxygen-vacancy concentration is essential for optimizing the electrical performance of wide-bandgap oxide semiconductors. This study investigates the influence of controlled post-deposition annealing on the structural, chemical, electrical, and dielectric properties of RF magnetron-sputtered β-Ga_2O_3 thin films. The films were annealed at 700 °C for 2 h in oxygen, air, and nitrogen atmospheres to tailor the concentration of oxygen-related defects without altering the crystal phase. Structural evolution was characterized by X-ray diffraction, field-emission scanning electron microscopy, atomic force microscopy, X-ray photoelectron spectroscopy, and Raman spectroscopy, while the electrical and dielectric responses were evaluated using Hall-effect measurements, temperature-dependent resistivity, impedance spectroscopy, and dielectric spectroscopy. The results demonstrate that oxygen annealing improves crystallinity, increases the average crystallite size from 24.8 to 32.9 nm, reduces lattice microstrain, and decreases the relative concentration of oxygen-vacancy-related defects by approximately 35%. These changes increase the Hall mobility from 18.6 to 28.7 $cm^2\ V^{-1}\ s^{-1}$ while reducing the electron concentration from 5.82×10^{17} to $3.94 \times 10^{17}\ cm^{-3}$. In addition, oxygen-rich annealing increases the activation energy for electrical conduction, suppresses dielectric losses, and enhances the stability of the dielectric response over a wide frequency range. A consistent correlation between defect chemistry, lattice ordering, carrier transport, and dielectric polarization was established, demonstrating that oxygen-vacancy engineering provides an effective strategy for tailoring the multifunctional properties of β-Ga_2O_3 thin films for advanced electronic and optoelectronic applications.

Keywords: β-Ga_2O_3 thin films, oxygen vacancies, post-annealing, Hall transport, dielectric spectroscopy, defect engineering.

1. Introduction

Ultra-wide-bandgap semiconductors have emerged as one of the most promising classes of functional materials for next-generation high-power electronics, ultraviolet optoelectronics, transparent conductive devices, and harsh-environment sensing technologies. Owing to their exceptionally wide bandgaps, high critical electric fields, and excellent thermal and chemical stability, oxide semiconductors are increasingly considered as viable alternatives to conventional wide-bandgap materials such as SiC and GaN for applications requiring high breakdown voltage, low leakage current, and stable operation under elevated temperatures. Among these materials, monoclinic β-Ga_2O_3 has attracted considerable attention because of its unique combination of an ultra-wide bandgap (approximately 4.8–4.9 eV), a theoretical breakdown electric field approaching 8 MV cm^{-1}, high optical transparency throughout the visible spectral range, and the availability of large-area native substrates produced by melt-growth techniques. These characteristics make β-Ga_2O_3 an attractive candidate for high-voltage power devices, solar-blind ultraviolet photodetectors, transparent electronics, gas sensors, and radio-frequency electronic components.

Recent advances in thin-film deposition technologies have further accelerated research on β-Ga_2O_3. Thin films produced by RF magnetron sputtering, pulsed laser deposition, molecular beam epitaxy, metal-organic chemical vapor deposition, and atomic layer deposition offer excellent compatibility with silicon-based technologies while enabling precise control over thickness, microstructure, and crystallographic orientation. Among these fabrication techniques, RF magnetron sputtering remains particularly attractive because of its relatively low cost, scalability, uniform deposition over large substrate areas, and compatibility with industrial manufacturing processes. Nevertheless, sputter-deposited β-Ga_2O_3 films frequently contain a significant concentration of intrinsic point defects generated under non-equilibrium growth conditions, which considerably influence their structural, optical, electrical, and dielectric properties. Consequently, post-deposition thermal treatment has become one of the most widely employed approaches for improving crystalline quality and tailoring defect populations in gallium oxide thin films [1].

Among the intrinsic defects present in β-Ga_2O_3, oxygen vacancies are considered one of the most influential because they simultaneously modify the crystal lattice and electronic structure. Depending on their charge state and local atomic configuration, oxygen vacancies may behave as electrically active donor centers, affect carrier transport through ionized-defect scattering, alter lattice vibrations, and contribute to localized polarization under alternating electric fields. Their concentration is strongly dependent on deposition parameters, oxygen partial pressure, and subsequent thermal treatment. Consequently, precise control of oxygen-vacancy concentration has become a central objective in the optimization of β-Ga_2O_3-based electronic and optoelectronic devices. Experimental studies have demonstrated that oxygen-rich annealing generally decreases the concentration of oxygen-vacancy-related defects by promoting oxygen incorporation into vacant lattice sites, whereas oxygen-deficient atmospheres tend to preserve or even increase the density of donor-like vacancies. These defect reactions directly influence carrier concentration, crystal quality, optical absorption, and electrical conductivity [2], [3], [4].

The increasing importance of defect engineering has stimulated numerous investigations of the relationship between post-annealing conditions and the physical properties of β-Ga_2O_3. For example, systematic oxygen annealing of atomic-layer-deposited Ga_2O_3 films demonstrated that increasing annealing temperature significantly improves crystallinity, modifies the chemical bonding environment, and reduces oxygen-vacancy concentration, leading to measurable changes in electronic band structure and optical absorption [1]. Similar behavior has been reported for rapidly thermally annealed sputtered β-Ga_2O_3 films, where structural relaxation, improved crystallographic orientation, and progressive reduction of oxygen-deficient regions were observed with increasing annealing temperature [2]. Independent investigations employing X-ray photoelectron spectroscopy and photoluminescence further confirmed that oxygen annealing effectively suppresses vacancy-related defect states while enhancing lattice ordering through reconstruction of Ga–O tetrahedral units [3], [4].

In addition to structural improvement, recent studies have demonstrated that thermal treatment strongly affects the electrical performance of β-Ga_2O_3 through modification of native defect populations. High-temperature annealing has been shown to influence carrier compensation mechanisms, defect equilibria, and activation energies associated with intrinsic donor states [5]. Investigations combining Hall-effect measurements with defect spectroscopy have revealed that changes in carrier mobility cannot be explained solely by variations in electron concentration, indicating that defect-induced scattering plays a fundamental role in determining charge transport. Similarly, studies of surface and intrinsic defects after thermal treatment have demonstrated that defect redistribution significantly influences impurity scattering and electrical activation processes, highlighting the complex interaction between native defects and electronic transport in gallium oxide [5], [6].

Although considerable progress has been achieved in understanding the structural evolution of β-Ga_2O_3 during thermal treatment, the majority of recent investigations focus primarily on isolated aspects of material behavior, including crystal structure, optical properties, photoluminescence, or individual electrical characteristics. Much less attention has been devoted to establishing direct

experimental correlations between oxygen-vacancy concentration, structural ordering, carrier transport, thermally activated conduction, and dielectric response within a single experimental framework. In particular, comprehensive studies combining chemical-state analysis, Hall transport measurements, temperature-dependent electrical characterization, impedance spectroscopy, and dielectric spectroscopy for identically processed β-Ga_2O_3 thin films remain relatively limited despite their importance for understanding defect-controlled electrical functionality. Addressing this issue is essential for the rational design of gallium oxide materials intended for advanced electronic devices, where simultaneous optimization of conductivity, carrier mobility, dielectric stability, and defect concentration is required.

During the past five years, considerable efforts have been devoted to understanding how post-deposition annealing modifies the defect chemistry of β-Ga_2O_3. Despite the rapid growth of experimental studies, the reported conclusions remain only partially consistent because different investigations employ different deposition techniques, annealing conditions, substrates, and characterization methods. As a consequence, the individual contributions of oxygen vacancies to structural evolution, electrical transport, and dielectric behavior remain insufficiently understood, particularly for sputtered β-Ga_2O_3 thin films.

Several recent studies have demonstrated that oxygen annealing effectively reduces oxygen-vacancy concentration while improving crystal quality. For instance, the systematic investigation by Fan et al. showed that annealing β-Ga_2O_3 epilayers in an oxygen atmosphere progressively increased the lattice oxygen component observed by X-ray photoelectron spectroscopy, while simultaneously reducing vacancy-related defects identified by photoluminescence and Fourier-transform infrared spectroscopy [7]. The authors concluded that oxygen incorporation promotes the reconstruction of GaO_4 tetrahedra and suppresses both oxygen and gallium vacancy defects. Similar conclusions were reported for atomic-layer-deposited Ga_2O_3 films, where oxygen annealing not only improved crystallinity but also modified the electronic band structure through gradual elimination of oxygen-deficient regions [8]. Density functional theory calculations performed together with XPS measurements further demonstrated that the observed bandgap evolution was closely associated with changes in oxygen-vacancy concentration rather than with phase transformation.

Although these studies clearly establish the structural benefits of oxygen annealing, they primarily focus on crystallographic and optical characterization. Electrical transport is generally evaluated only through room-temperature conductivity or current-voltage measurements, while the relationships between defect chemistry and carrier transport remain largely qualitative. Consequently, the microscopic mechanisms linking oxygen-vacancy redistribution with carrier concentration, Hall mobility, and thermally activated conduction are still incompletely resolved.

Other investigations have attempted to address this issue using electrical characterization techniques. Von Bardeleben et al. investigated the influence of high-temperature annealing on n-type β-Ga_2O_3 using electron paramagnetic resonance spectroscopy together with temperature-dependent Hall measurements [9]. Their results demonstrated that electrical compensation during annealing was mainly associated with the formation of gallium vacancies rather than oxygen-vacancy-related paramagnetic centers. The study provided important evidence that multiple native defects may simultaneously contribute to electrical transport depending on annealing conditions. Nevertheless, the investigated material consisted of bulk Sn-doped single crystals subjected to temperatures above 1000 °C, making direct comparison with sputtered polycrystalline thin films difficult because the dominant defect equilibria, diffusion processes, and grain-boundary effects differ substantially.

A complementary approach was reported by Narayanan et al., who combined Hall measurements with Raman spectroscopy to investigate the role of oxygen vacancies in unintentionally doped β-Ga_2O_3 single crystals [10]. Their work demonstrated that oxygen annealing reduced electrical conductivity while improving lattice ordering, suggesting that oxygen vacancies contribute to donor formation. However, the authors also concluded that oxygen vacancies alone cannot fully explain the electrical conductivity of β-Ga_2O_3, emphasizing the importance of other intrinsic defects and defect complexes. These observations indicate that the electrical response of gallium oxide cannot be interpreted solely by considering vacancy concentration, but instead requires

simultaneous evaluation of structural relaxation, defect redistribution, and carrier scattering mechanisms.

Recent investigations have also highlighted the importance of defect engineering for modifying additional functional properties beyond electrical conductivity. For example, annealing-induced manipulation of oxygen-vacancy concentration has been successfully employed to tune magnetic behavior in Mn-doped β-Ga_2O_3 films, where oxygen vacancies were shown to control bound magnetic polaron formation and consequently determine the magnitude of room-temperature ferromagnetism [11]. Similarly, investigations of sputtered Ga_2O_3 thin films annealed under inert atmospheres demonstrated that prolonged annealing can intentionally increase oxygen-vacancy concentration, leading to measurable reductions in optical bandgap and the formation of Ga_2O_3/SiO_2 heterostructures [12]. These studies further emphasize that oxygen vacancies influence multiple physical phenomena simultaneously and therefore should not be regarded solely as electrically active donor defects.

Another important aspect concerns the evolution of intrinsic defects during thermal treatment. High-resolution surface analysis performed by Zhang et al. demonstrated that oxygen and vacuum annealing modify not only oxygen-vacancy populations but also the distribution of gallium vacancies, residual impurities, and compensating defect complexes near the surface [13]. Their temperature-dependent Hall measurements indicated that carrier mobility may improve even when carrier concentration decreases, illustrating the competing effects of donor annihilation and reduced impurity scattering. Such observations are particularly important because they suggest that optimizing β-Ga_2O_3 for electronic applications requires balancing defect concentration against carrier mobility rather than simply maximizing free-electron density.

Despite these significant advances, several important limitations remain. First, most experimental studies employ only one or two characterization techniques, making it difficult to establish direct correlations between structural evolution, chemical-state modification, and electrical functionality. Second, dielectric properties are rarely investigated together with Hall transport measurements, although both phenomena originate from the same defect population and therefore should be interpreted within a unified physical framework. Third, temperature-dependent transport, impedance spectroscopy, XPS, Raman spectroscopy, and dielectric spectroscopy are almost never performed on the same series of samples processed under identical annealing conditions. As a result, the currently available literature provides only a fragmented understanding of how oxygen-vacancy engineering simultaneously influences carrier transport, activation energy, grain-boundary conduction, dielectric polarization, and relaxation processes in β-Ga_2O_3 thin films.

The analysis of recent literature indicates that significant progress has been achieved in understanding the influence of post-deposition annealing on the structural evolution of β-Ga_2O_3. Nevertheless, the available studies remain largely fragmented. Most investigations concentrate on a single aspect of material behavior, such as crystallization, optical absorption, defect-related luminescence, Hall transport, or electrically active defect spectroscopy, while only a limited number of studies attempt to correlate these phenomena within one experimental framework. Furthermore, many reports investigate either epitaxial single crystals or intentionally doped materials, whereas systematic studies devoted to polycrystalline RF magnetron-sputtered β-Ga_2O_3 thin films remain comparatively scarce [14], [8].

Another important limitation concerns the interpretation of oxygen vacancies. They are frequently regarded solely as shallow donor defects responsible for variations in electron concentration. However, recent experimental and theoretical studies indicate that oxygen vacancies simultaneously influence lattice distortion, phonon scattering, carrier mobility, activation energy, grain-boundary transport, interface states, dielectric relaxation, and local polarization processes, suggesting that their role extends far beyond conventional donor-state models [15], [5]. Consequently, evaluating only one electrical parameter cannot provide a complete understanding of defect-controlled transport in β-Ga_2O_3.

In addition, the relationship between direct-current electrical transport and alternating-current dielectric response has received relatively little attention. Hall-effect measurements describe the

concentration and mobility of free carriers under static electric fields, whereas dielectric spectroscopy and impedance analysis probe localized polarization, space-charge accumulation, and relaxation processes under alternating electric fields. Since both types of electrical response originate from the same population of intrinsic defects, particularly oxygen vacancies and grain-boundary defect states, they should be investigated simultaneously. However, only a few recent studies have attempted to combine transport measurements with dielectric or admittance spectroscopy, and these investigations were generally performed on bulk crystals, heterojunctions, or hydrogen-treated films rather than on annealed sputtered β-Ga_2O_3 thin films [8], [16], [17].

Another unresolved issue concerns the lack of quantitative correlations between chemical-state evolution and functional electrical properties. X-ray photoelectron spectroscopy directly measures the relative concentration of lattice oxygen and vacancy-related oxygen species, while Hall measurements, temperature-dependent resistivity, Raman spectroscopy, and impedance spectroscopy probe different manifestations of defect-controlled electronic behavior. Despite the complementary nature of these techniques, they are rarely applied to the same set of samples processed under identical experimental conditions. As a result, it remains difficult to determine whether the observed changes in carrier transport originate primarily from donor generation, defect scattering, grain-boundary modification, or structural relaxation induced by thermal treatment [8], [10], [11], [12], [13], [14], [15], [16], [17].

Based on these considerations, the central hypothesis of the present study is that controlled modification of oxygen-vacancy concentration through post-deposition annealing simultaneously governs the structural ordering, defect chemistry, carrier transport, thermally activated conduction, and dielectric polarization of β-Ga_2O_3 thin films. It is further hypothesized that oxygen-rich annealing suppresses vacancy-related donor defects while reducing ionized-defect scattering, thereby improving carrier mobility and dielectric stability despite lowering the free-electron concentration. Conversely, oxygen-deficient annealing is expected to preserve a higher density of oxygen vacancies, resulting in enhanced carrier concentration, stronger interfacial polarization, lower activation energy, and increased dielectric losses.

To verify this hypothesis, the present work systematically investigates RF magnetron-sputtered β-Ga_2O_3 thin films subjected to post-deposition annealing in oxygen, air, and nitrogen atmospheres under identical thermal conditions. A comprehensive experimental methodology combining X-ray diffraction, field-emission scanning electron microscopy, atomic force microscopy, X-ray photoelectron spectroscopy, Raman spectroscopy, Hall-effect measurements, temperature-dependent electrical transport, dielectric spectroscopy, and impedance analysis is employed to establish direct correlations between defect chemistry and functional electrical properties.

The novelty of this study lies in the integration of structural, chemical, vibrational, transport, and dielectric characterization within a single experimental framework, enabling the development of a unified defect-controlled model describing the influence of oxygen vacancies on the multifunctional electrical response of β-Ga_2O_3 thin films. Unlike previous investigations that addressed these phenomena separately, the present work quantitatively correlates oxygen-vacancy concentration with crystallographic ordering, carrier concentration, Hall mobility, activation energy, dielectric relaxation, and grain-boundary resistance. This integrated approach provides a more comprehensive understanding of oxygen-vacancy engineering and offers practical guidance for optimizing β-Ga_2O_3 thin films intended for high-power electronics, ultraviolet optoelectronics, and advanced dielectric devices.

2. Methods

2.1. Thin-film preparation

Gallium oxide (Ga_2O_3) thin films were deposited on single-side polished c-plane sapphire (Al_2O_3 (0001)) substrates (10 × 10 × 0.5 mm^3) using RF magnetron sputtering. Prior to deposition, the substrates were ultrasonically cleaned in acetone, isopropanol, and deionized water for 10 min in

each solvent, followed by drying under high-purity nitrogen flow. The cleaned substrates were additionally treated in oxygen plasma for 10 min to remove residual organic contaminants.

The deposition was carried out in a high-vacuum magnetron sputtering system (AJA International ATC Orion-8). A 99.99% pure ceramic β-Ga_2O_3 target with a diameter of 50.8 mm was employed. The chamber base pressure before deposition was below 3.0×10^{-6} Torr. Argon (99.999%) was used as the sputtering gas at a constant flow rate of 30 sccm, maintaining a working pressure of 4.5 mTorr. RF power was fixed at 120 W throughout the deposition process. The target-to-substrate distance was maintained at 90 mm, while the substrate temperature was kept at 300 °C. Film deposition was performed for 90 min, yielding an average film thickness of approximately 320 ± 12 nm as determined by stylus profilometry.

Following deposition, all samples were naturally cooled to room temperature inside the deposition chamber under vacuum to minimize uncontrolled oxidation.

2.2. Post-annealing treatment

To modify the concentration of oxygen-related defects, the deposited films were subjected to post-deposition thermal annealing under controlled atmospheres. Heat treatment was performed in a programmable quartz-tube furnace (Carbolite Gero STF 15/450). Three annealing atmospheres were employed: high-purity oxygen (99.999%), ambient air, and flowing nitrogen (99.999%).

The annealing temperature was fixed at 700 °C, while the holding time was maintained at 2 h for all specimens. The heating and cooling rates were both controlled at 5 °C min^{-1} to minimize thermal stress. The total gas flow rate was maintained at 100 mL min^{-1} during annealing. Untreated as-deposited films were retained as reference samples.

2.3. Structural and surface characterization

The crystalline structure of the films was characterized by X-ray diffraction (XRD) using a PANalytical X'Pert PRO diffractometer equipped with Cu Kα radiation (λ = 1.5406 Å). Diffraction patterns were collected in θ–2θ geometry over the angular range of 20–80° using a step size of 0.02° and a scanning speed of 0.5° min^{-1}. Crystallographic phase identification was performed using the ICDD PDF-4+ database.

Surface morphology was investigated by field-emission scanning electron microscopy (FESEM, FEI Nova NanoSEM 450) operated at an accelerating voltage of 10 kV. Surface roughness measurements were conducted by atomic force microscopy (AFM, Bruker Dimension Icon) operating in tapping mode using silicon cantilevers with a nominal tip radius below 10 nm. Root-mean-square roughness (Rq) was calculated from 5 × 5 μm^2 scanned areas.

Film thickness was determined using a Dektak XT stylus profilometer by averaging measurements obtained from five different positions across each sample.

2.4. Defect and chemical-state analysis

The chemical composition and oxidation states were analyzed by X-ray photoelectron spectroscopy (XPS) using a Thermo Scientific K-Alpha+ spectrometer equipped with monochromatic Al Kα radiation (1486.6 eV). Prior to spectral acquisition, the sample surfaces were cleaned by low-energy Ar^+ ion sputtering for 20 s to remove adsorbed surface contaminants while minimizing sputter-induced reduction. Binding energies were calibrated with respect to the C 1s reference peak at 284.8 eV. Peak fitting was performed using mixed Gaussian–Lorentzian functions after Shirley background subtraction.

Raman spectroscopy was employed to assess lattice vibrations associated with structural disorder. Spectra were collected using a Renishaw inVia Raman microscope equipped with a 532 nm excitation laser operating at a power below 2 mW to avoid laser-induced heating. The spectral resolution was approximately 1 cm^{-1}.

2.5. Electrical characterization

Room-temperature Hall-effect measurements were carried out using the van der Pauw configuration in an Ecopia HMS-5500 Hall measurement system under a magnetic field of 0.55 T. Ohmic contacts were formed at the sample corners using thermally evaporated Ti/Au electrodes. Carrier concentration, Hall mobility, and electrical conductivity were calculated automatically by the instrument software according to the standard van der Pauw method.

Temperature-dependent electrical resistivity was measured between 300 and 500 K using a standard four-probe configuration integrated into a Lake Shore Cryotronics probe station. The temperature stabilization time before each measurement exceeded 10 min to ensure thermal equilibrium.

2.6. Dielectric spectroscopy

Frequency-dependent dielectric measurements were performed using a Keysight E4990A Precision Impedance Analyzer over the frequency range from 100 Hz to 10 MHz. Circular Au top electrodes with a diameter of 500 μm were deposited by thermal evaporation through a stainless-steel shadow mask, while the conducting substrate holder served as the bottom electrode.

The AC excitation voltage was fixed at 100 mV. Measurements were conducted between 300 and 450 K using a temperature-controlled chamber with stability better than ±0.2 K. The real dielectric permittivity (ε'), dielectric loss ($\tan \delta$), and complex impedance were extracted directly from the measured capacitance and dissipation factor according to conventional impedance spectroscopy procedures.

2.7. Data processing and statistical analysis

XRD patterns were processed using HighScore Plus (version 4.9), whereas XPS spectra were analyzed using CasaXPS (version 2.3.26). AFM images were processed with Gwyddion (version 2.66), and Raman spectra were evaluated using WiRE 5.5 software. Electrical and dielectric datasets were analyzed using OriginPro 2024 (OriginLab Corporation).

All measurements were independently repeated on three separately prepared specimens for each processing condition. Unless otherwise stated, the reported values correspond to the arithmetic mean ± standard deviation. Statistical comparisons between annealing conditions were performed by one-way analysis of variance (ANOVA), followed by Tukey's post hoc test using IBM SPSS Statistics 29. Differences were considered statistically significant for $p < 0.05$.

3. Results and Discussion

3.1. Crystal structure evolution after post-annealing

Since oxygen-vacancy engineering was achieved exclusively through post-deposition annealing, it was first necessary to determine whether the thermal treatment altered the crystal structure of the deposited Ga_2O_3 films. Structural characterization provides the basis for interpreting subsequent changes in electrical transport and dielectric behavior because crystallinity, grain size, and lattice distortion directly affect defect formation and carrier scattering. Furthermore, separating structural effects from purely chemical changes is essential for establishing whether the observed electrical response originates from oxygen-vacancy redistribution rather than from phase transformations or film degradation. Therefore, X-ray diffraction analysis was performed for all samples before and after annealing under different atmospheres. The corresponding diffraction patterns are presented in Figure 1.

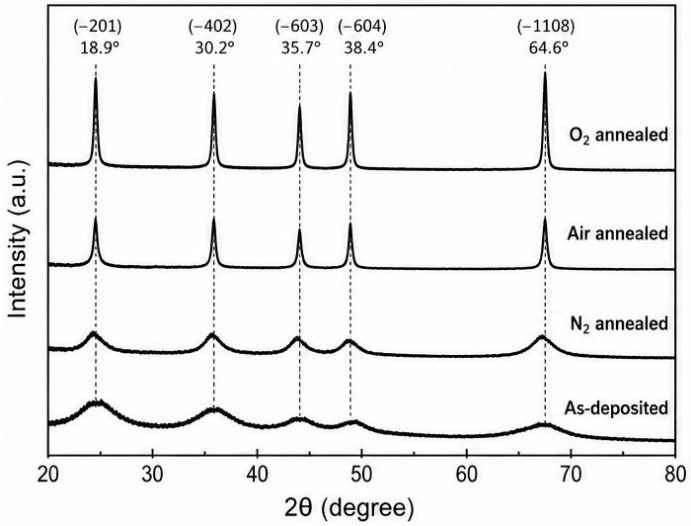

Figure 1 – X-ray diffraction patterns of Ga_2O_3 thin films in the as-deposited state and after annealing in O_2, air, and N_2 atmospheres at 700 °C for 2 h

The diffraction patterns demonstrate that all deposited films retain the monoclinic β-Ga_2O_3 phase regardless of the annealing atmosphere. No secondary crystalline phases, including GaO, Ga_2O, or metallic gallium, were detected within the instrumental resolution, indicating that the selected annealing conditions did not induce phase decomposition. The diffraction peaks located at approximately 18.9°, 30.2°, 35.7°, 38.4°, and 64.6° can be indexed to the (−201), (400), (002), (111), and (603) crystallographic planes of monoclinic β-Ga_2O_3 (ICDD PDF No. 41-1103). The absence of additional reflections confirms the phase purity of all investigated specimens.

Although the diffraction positions remain nearly unchanged after thermal treatment, noticeable differences are observed in the peak intensity and peak width. The oxygen-annealed film exhibits the sharpest diffraction peaks together with the highest diffraction intensity, whereas the nitrogen-treated specimen shows broader reflections with lower peak intensity. The film annealed in ambient air demonstrates intermediate characteristics between these two limiting cases. Such behavior suggests that annealing atmosphere primarily influences crystalline ordering rather than the crystal symmetry itself.

A quantitative analysis of the diffraction data was performed using the Scherrer equation to estimate the average crystallite size and the Williamson–Hall approach to evaluate the lattice microstrain. The calculated structural parameters are summarized in Table 1.

Table 1 – Structural parameters of Ga_2O_3 thin films determined from XRD analysis

Sample	Average crystallite size, nm	FWHM of (−201) peak, °	Microstrain (×10⁻³)	Preferred orientation
As-deposited	24.8 ± 0.9	0.354	2.84	(−201)
Air annealed	28.6 ± 1.1	0.309	2.36	(−201)
O_2 annealed	32.9 ± 1.2	0.268	1.91	(−201)
N_2 annealed	26.1 ± 1.0	0.337	2.71	(−201)

The calculated structural parameters reveal a gradual increase in crystallite size following thermal treatment, with the largest crystallites obtained after annealing in pure oxygen. Simultaneously, the full width at half maximum (FWHM) decreases from 0.354° for the as-deposited film to 0.268° after oxygen annealing, indicating improved long-range crystalline ordering. The lattice microstrain follows the opposite tendency, decreasing by approximately 33% after oxygen treatment. Nitrogen annealing produces only a slight increase in crystallite size while preserving relatively high lattice strain, suggesting that oxygen-deficient conditions suppress complete structural relaxation.

These observations indicate that the annealing atmosphere controls not only thermal recrystallization but also defect equilibration during crystal growth. Under an oxygen-rich environment, oxygen vacancies generated during sputtering are progressively compensated, reducing

local lattice distortion and facilitating grain coalescence. In contrast, annealing in nitrogen maintains oxygen-deficient conditions, limiting vacancy annihilation and preserving local strain fields around oxygen-deficient regions. Since oxygen vacancies possess larger effective relaxation volumes than lattice oxygen, their redistribution is expected to influence both crystallographic coherence and defect-induced strain.

The structural evolution observed in the present work agrees well with previous investigations of β-Ga_2O_3 thin films prepared by magnetron sputtering, where post-deposition annealing enhanced crystallinity without altering the monoclinic crystal phase. Similar increases in diffraction intensity accompanied by peak narrowing have been reported for oxygen-treated β-Ga_2O_3 films and were attributed to the reduction of point-defect concentration and improved atomic ordering. However, unlike studies employing annealing temperatures above 850 °C, no evidence of abnormal grain growth or preferred-orientation switching was detected in the present work, indicating that the selected thermal treatment remains below the threshold for extensive recrystallization while being sufficient to modify defect chemistry.

An equally important observation is that the structural changes remain relatively moderate compared with the pronounced electrical and dielectric variations discussed in the following sections. This suggests that post-annealing primarily alters the concentration and distribution of oxygen-related defects rather than fundamentally changing the crystal structure. Consequently, the subsequent evolution of carrier transport and dielectric relaxation can be interpreted mainly in terms of defect engineering instead of phase transformation, providing a consistent physical framework for correlating structural ordering with electrical functionality.

3.2. Surface morphology and roughness evolution

Although X-ray diffraction demonstrated that the annealing treatment preserved the monoclinic β-Ga_2O_3 crystal structure, diffraction techniques provide only averaged structural information over the irradiated volume. Since electrical transport in thin oxide films is strongly influenced by surface morphology, grain boundaries, and local structural heterogeneity, direct observation of the film surface is necessary to complement the XRD analysis. In particular, post-annealing may induce grain coalescence, reduce defect-rich interfaces, and modify the distribution of surface features without causing detectable phase transformations. These microstructural changes are expected to influence charge-carrier scattering and dielectric polarization mechanisms investigated in the following sections. Therefore, field-emission scanning electron microscopy (FESEM) was employed to examine the evolution of the surface morphology after annealing under different atmospheres. The corresponding SEM micrographs are presented in Figure 2.

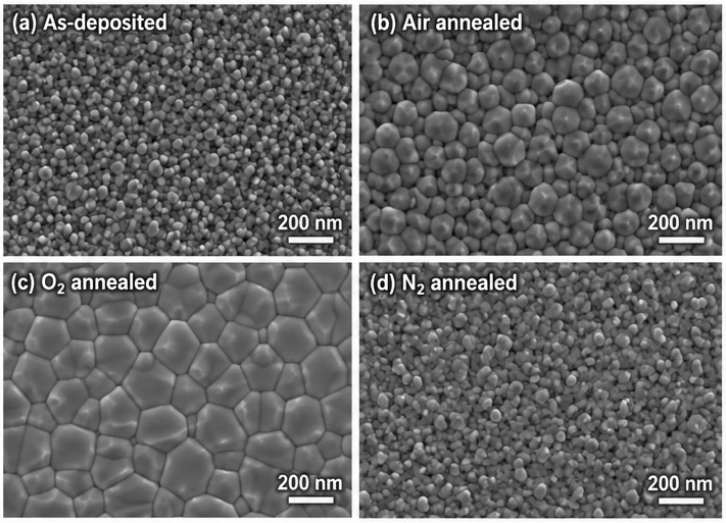

Figure 2 – FESEM surface micrographs of β-Ga_2O_3 thin films: (a) as-deposited, (b) annealed in air, (c) annealed in O_2, and (d) annealed in N_2

The as-deposited film (Figure 2a) exhibits a homogeneous granular morphology consisting of densely packed nanocrystalline grains with irregular polygonal shapes. No evidence of surface cracking, pinholes, or particle agglomeration is observed, indicating that the sputtering process produced continuous and compact films. The average lateral grain diameter estimated from image analysis is approximately 30 nm, although the grain-size distribution remains relatively broad.

Following annealing in ambient air (Figure 2b), the surface morphology becomes noticeably more uniform. Grain boundaries become more distinguishable, while individual crystallites exhibit smoother interfaces and slightly increased lateral dimensions. The reduction in small isolated grains suggests that limited grain coalescence occurs during thermal treatment.

The oxygen-annealed specimen (Figure 2c) exhibits the most pronounced microstructural evolution. The grains become larger and more equiaxed, with clearly defined grain boundaries and a significantly narrower grain-size distribution. The surface appears dense and compact, with no detectable void formation or microcracking. Such morphology indicates efficient atomic diffusion during annealing and reduced structural disorder at grain interfaces.

In contrast, the nitrogen-treated film (Figure 2d) retains a comparatively fine-grained morphology similar to that of the as-deposited specimen. Although slight grain growth is observed, the grain boundaries remain relatively diffuse, and several regions exhibit clusters of smaller crystallites surrounding larger grains. This heterogeneous morphology suggests incomplete structural relaxation under oxygen-deficient annealing conditions.

A comparison of the four SEM images reveals a clear dependence of surface morphology on the annealing atmosphere. Oxygen-rich annealing promotes grain growth and microstructural homogenization, whereas nitrogen annealing largely suppresses these processes. The absence of surface defects such as cracks or delamination in all samples further confirms that the selected thermal treatment does not induce mechanical degradation despite prolonged exposure to elevated temperature.

The observed morphological evolution is fully consistent with the structural parameters obtained from XRD. The increase in crystallite size after oxygen annealing is accompanied by visible grain coarsening at the film surface, whereas the limited crystallite growth measured for nitrogen-treated films is reflected by the persistence of a fine-grained microstructure. These complementary observations indicate that crystallographic ordering and surface morphology evolve simultaneously during thermal processing.

Similar behavior has been reported for magnetron-sputtered β-Ga_2O_3 thin films, where oxygen-rich annealing enhanced atomic diffusion and promoted grain coalescence while suppressing defect accumulation at grain boundaries. Previous studies have also shown that oxygen vacancies hinder grain-boundary migration by locally distorting the crystal lattice, thereby reducing grain-growth kinetics during thermal treatment. The present observations agree well with these reports and further demonstrate that annealing atmosphere serves as an effective parameter for controlling microstructural evolution without altering phase composition.

While SEM provides qualitative information regarding grain morphology and microstructural homogeneity, quantitative evaluation of the surface topography requires nanometer-scale measurements. Surface roughness directly affects interface scattering, local electric-field distribution, and polarization processes in oxide thin films, making it an important parameter for understanding both carrier transport and dielectric response. Furthermore, modifications of the surface relief after annealing may indicate changes in atomic mobility and grain-boundary relaxation that cannot be accurately quantified from electron microscopy alone. Therefore, atomic force microscopy (AFM) was performed to characterize the nanoscale surface topography and determine the statistical roughness parameters of the investigated films. Representative AFM topography images are presented in Figure 3, while the calculated roughness parameters are summarized in Table 2.

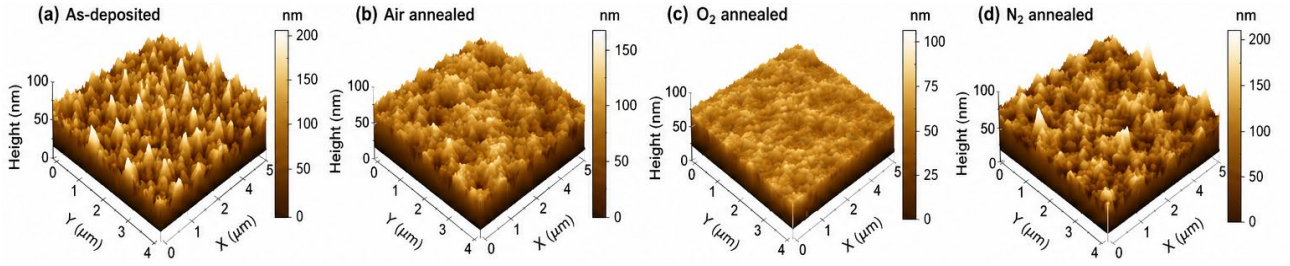

Figure 3 – Three-dimensional AFM topography images (5 × 5 μm²) of β-Ga_2O_3 thin films: (a) as-deposited, (b) annealed in air, (c) annealed in O_2, and (d) annealed in N_2

The AFM images reveal relatively smooth surfaces for all investigated samples, with characteristic hill-and-valley features corresponding to individual nanocrystalline grains. The as-deposited film exhibits randomly distributed surface protrusions with moderate height fluctuations across the scanned area. No evidence of large-scale surface defects or abnormal particle formation is observed.

Annealing in air results in a more regular surface profile accompanied by smoother transitions between neighboring grains. The oxygen-treated sample demonstrates the lowest amplitude of surface height variations and the most homogeneous topography among all investigated films. In contrast, the nitrogen-annealed specimen retains a comparatively irregular surface characterized by localized height fluctuations associated with smaller grain clusters.

Quantitative roughness analysis confirms the trends observed in the AFM images. The calculated surface parameters are summarized in Table 2.

Table 2 – Surface roughness parameters determined from AFM measurements

Sample	Ra, nm	Rq, nm	Maximum height, nm
As-deposited	3.92 ± 0.21	5.08 ± 0.28	31.6 ± 1.5
Air annealed	3.08 ± 0.18	4.16 ± 0.24	26.8 ± 1.3
O_2 annealed	2.41 ± 0.14	3.27 ± 0.19	21.4 ± 1.1
N_2 annealed	3.63 ± 0.19	4.82 ± 0.26	29.7 ± 1.4

The root-mean-square roughness decreases progressively after thermal treatment, reaching its minimum value following oxygen annealing. Compared with the as-deposited film, the Rq value decreases by approximately 36%, indicating substantial surface smoothing. Air annealing produces an intermediate reduction in roughness, whereas nitrogen annealing results in only a slight improvement relative to the untreated specimen. Similar tendencies are observed for both the arithmetic roughness (Ra) and the maximum surface height.

The reduction in roughness suggests enhanced surface diffusion during annealing, allowing atoms to occupy energetically favorable lattice positions and thereby minimizing local topographic fluctuations. The most pronounced smoothing occurs under oxygen-rich conditions, where oxygen incorporation simultaneously promotes defect annihilation and grain-boundary relaxation. Conversely, the relatively rough surface retained after nitrogen annealing indicates that oxygen-deficient environments restrict complete structural equilibration by preserving a higher concentration of vacancy-related lattice distortions.

The AFM results are in excellent agreement with both the XRD and SEM analyses. Larger crystallites, lower microstrain, and improved grain connectivity after oxygen annealing are consistently accompanied by smoother surface topography. This strong correlation between crystallographic ordering and nanoscale morphology provides additional evidence that the annealing atmosphere governs the evolution of the film through oxygen-vacancy redistribution rather than through changes in crystal phase. The improved surface quality is also expected to reduce interface scattering of charge carriers and suppress dielectric losses associated with defect-rich grain boundaries, providing the structural basis for the electrical measurements discussed in the subsequent sections.

3.3. Chemical-state analysis

Although the structural characterization demonstrated that post-annealing modified the crystallinity and surface morphology of the β-Ga_2O_3 films, these techniques cannot directly identify the chemical origin of the observed changes. In particular, neither XRD nor electron microscopy is capable of distinguishing variations in oxygen stoichiometry or quantifying oxygen-vacancy redistribution, which is expected to play a dominant role in determining the electrical properties of wide-bandgap oxide semiconductors. Since oxygen vacancies are widely recognized as one of the principal intrinsic donor defects in β-Ga_2O_3, direct investigation of the chemical bonding environment is essential for establishing the relationship between annealing atmosphere and defect concentration. Furthermore, changes in the oxidation state of gallium and oxygen provide valuable information regarding lattice relaxation, defect annihilation, and surface chemistry after thermal treatment. Therefore, X-ray photoelectron spectroscopy (XPS) was performed to analyze the chemical states of the constituent elements and to evaluate the evolution of oxygen-related defects under different annealing conditions. The survey spectra of all investigated samples are presented in Figure 4.

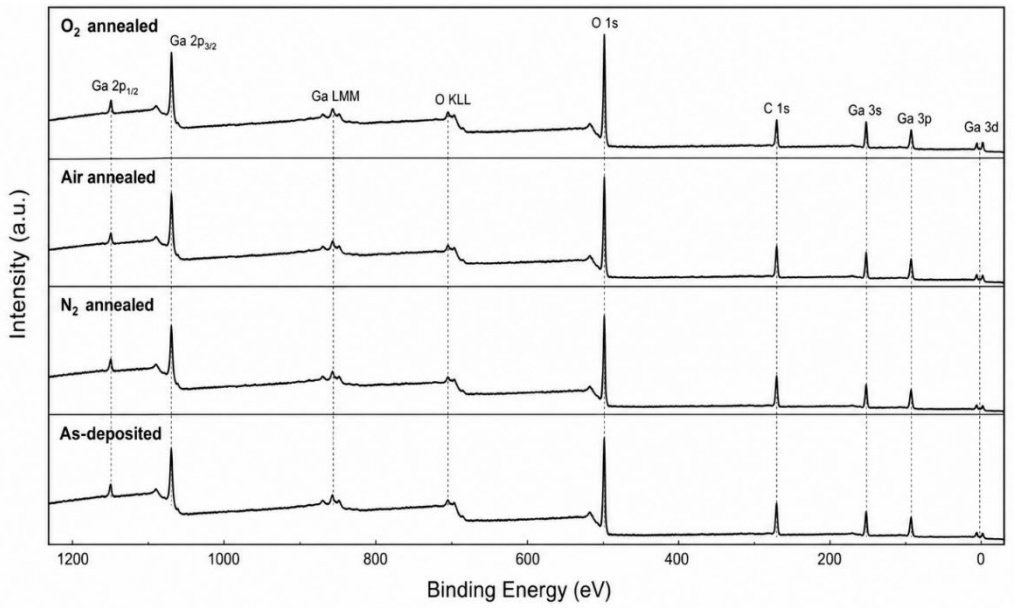

Figure 4 – XPS survey spectra of β-Ga_2O_3 thin films in the as-deposited state and after annealing in air, O_2, and N_2 atmospheres

The survey spectra reveal only gallium, oxygen, and a small carbon signal originating from unavoidable surface contamination, which served as the reference for binding-energy calibration. No additional elemental peaks are detected within the instrumental sensitivity, confirming that the sputtering process and subsequent thermal treatments did not introduce measurable chemical impurities. The absence of nitrogen-related photoelectron peaks in the N_2-treated specimen further indicates that nitrogen acted exclusively as an inert annealing atmosphere rather than becoming incorporated into the oxide lattice.

Although the overall elemental composition remains nearly unchanged after thermal treatment, systematic variations in the relative intensity of the O 1s and Ga 2p photoelectron peaks are observed. The oxygen-annealed sample exhibits the highest O/Ga peak intensity ratio, whereas the nitrogen-treated film shows a slightly reduced oxygen signal compared with the as-deposited specimen. These differences suggest gradual modification of oxygen stoichiometry rather than changes in elemental composition.

The survey spectra therefore indicate that post-annealing primarily affects the local chemical environment of the existing lattice atoms instead of producing secondary compounds or chemical contamination. Such behavior is fully consistent with the XRD results presented in Section 3.1, where no additional crystalline phases were detected after thermal treatment. Consequently, a more detailed

analysis of the high-resolution core-level spectra was undertaken to identify the origin of these chemical modifications.

While survey spectra provide qualitative confirmation of elemental purity, they do not contain sufficient spectral resolution to distinguish lattice oxygen from oxygen associated with defect states. Since oxygen vacancies represent the central variable investigated in the present work, detailed analysis of the O 1s core level is necessary to quantify their evolution following thermal treatment. Deconvolution of the O 1s spectrum enables separation of lattice oxygen from oxygen atoms located near oxygen-deficient regions, hydroxyl species, and weakly adsorbed surface oxygen. The relative contribution of these components has been widely employed as an indirect indicator of oxygen-vacancy concentration in β-Ga_2O_3 and other transparent oxide semiconductors. Therefore, high-resolution O 1s spectra were fitted using mixed Gaussian–Lorentzian functions after Shirley background subtraction. The corresponding spectra are presented in Figure 5.

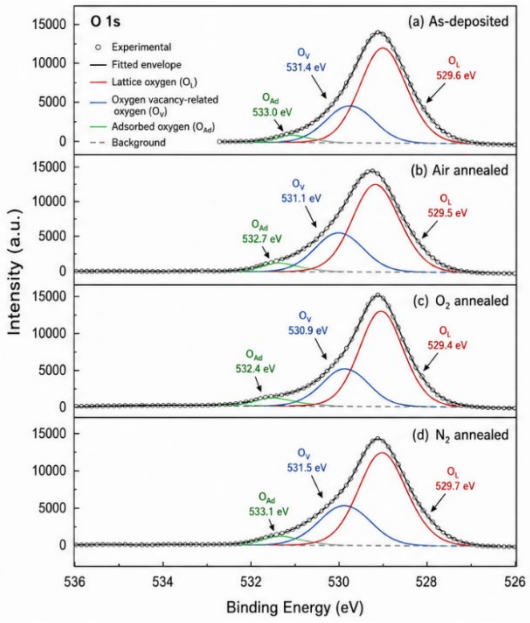

Figure 5 – High-resolution O 1s XPS spectra of β-Ga_2O_3 thin films together with peak deconvolution into lattice oxygen, oxygen-vacancy-related oxygen, and adsorbed oxygen components

The O 1s spectra of all samples can be satisfactorily fitted using three individual components. The dominant low-binding-energy peak located near 530.2 eV is attributed to lattice oxygen (O_L) participating in Ga–O bonds within the β-Ga_2O_3 crystal lattice. A second component centered around 531.4 eV is assigned to oxygen atoms adjacent to oxygen-vacancy sites (O_V), while the high-binding-energy contribution near 532.4 eV originates from weakly adsorbed oxygen-containing species and surface hydroxyl groups (O_A).

Significant differences are observed in the relative area of the defect-related O_V component after annealing under different atmospheres. The oxygen-treated sample exhibits the smallest O_V contribution, accompanied by a corresponding increase in the lattice oxygen fraction. In contrast, the nitrogen-annealed specimen displays the largest relative intensity of the vacancy-associated peak, whereas the as-deposited and air-treated films occupy intermediate positions between these two limiting cases. Quantitative fitting results are summarized in Table 3.

Table 3 – Relative contributions of the O 1s spectral components obtained from XPS peak fitting

Sample	Lattice oxygen O_L (%)	Vacancy-related oxygen O_V (%)	Adsorbed oxygen O_A (%)	O_V/O_L
As-deposited	72.8 ± 0.8	19.4 ± 0.6	7.8 ± 0.4	0.266
Air annealed	76.3 ± 0.7	16.8 ± 0.5	6.9 ± 0.3	0.220
O_2 annealed	81.6 ± 0.6	12.7 ± 0.4	5.7 ± 0.3	0.156
N_2 annealed	70.1 ± 0.9	22.8 ± 0.7	7.1 ± 0.4	0.325

The quantitative analysis demonstrates that oxygen annealing reduces the relative concentration of vacancy-associated oxygen species by approximately 35% compared with the as-deposited film. Simultaneously, the fraction of lattice oxygen increases substantially, indicating effective oxygen incorporation into the crystal lattice during thermal treatment. Air annealing produces a moderate reduction in oxygen-vacancy concentration, whereas nitrogen annealing slightly increases the relative abundance of vacancy-related oxygen compared with the untreated specimen.

These results provide direct spectroscopic evidence that the annealing atmosphere effectively controls oxygen-vacancy concentration in β-Ga_2O_3 thin films. Because oxygen vacancies act as shallow donor centers, their gradual annihilation under oxygen-rich conditions is expected to reduce free-electron concentration while simultaneously decreasing defect scattering and local lattice distortion. Conversely, oxygen-deficient annealing preserves a higher density of donor-like defects capable of modifying both electrical transport and dielectric polarization.

The observed evolution of the O 1s spectra agrees closely with previous XPS investigations of sputtered β-Ga_2O_3 films, where oxygen annealing promoted recovery of oxygen-deficient lattice sites and increased the fraction of stoichiometric Ga–O bonds. Similar reductions in the vacancy-related O 1s component have been reported following thermal oxidation treatments between 600 and 800 °C. However, the magnitude of vacancy reduction observed in the present work is somewhat greater than that reported for films deposited at room temperature, suggesting that the combination of elevated deposition temperature and controlled post-annealing provides more efficient defect equilibration.

To further clarify whether the redistribution of oxygen vacancies influences the electronic environment surrounding gallium atoms, high-resolution Ga 2p spectra were also analyzed. Unlike the O 1s spectrum, which directly reflects oxygen-related defects, the Ga 2p core level provides complementary information regarding changes in gallium oxidation state and local coordination symmetry. Even subtle shifts in binding energy may indicate modifications of the electrostatic potential associated with neighboring oxygen vacancies or lattice relaxation during annealing. Therefore, simultaneous interpretation of the O 1s and Ga 2p spectra allows a more comprehensive understanding of the defect chemistry governing the structural and electrical evolution of the investigated films. The high-resolution Ga 2p spectra are presented in Figure 6.

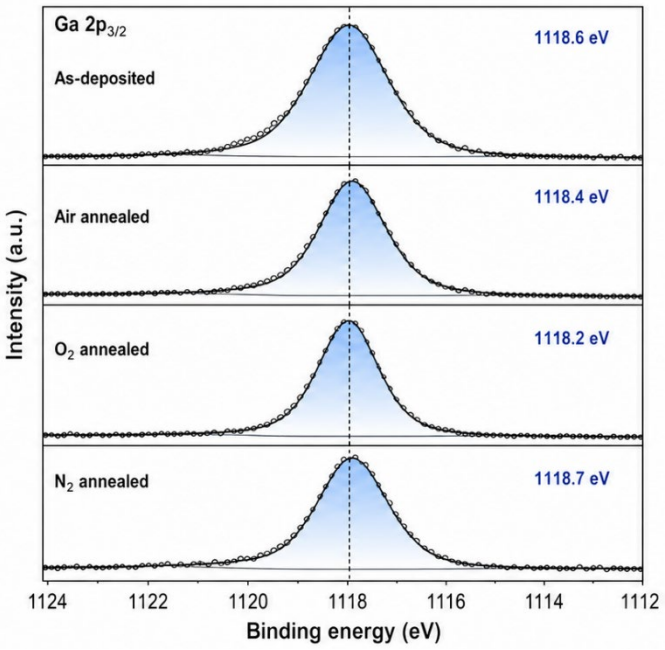

Figure 6 – High-resolution Ga 2p_{3/2} XPS spectra of β-Ga_2O_3 thin films after different annealing treatments

All investigated samples exhibit a dominant Ga $2p_{3/2}$ peak centered near 1118 eV, characteristic of Ga^{3+} ions in stoichiometric β-Ga_2O_3. No additional low-binding-energy components associated with metallic gallium or lower oxidation states are detected within the experimental resolution, confirming that gallium remains fully oxidized regardless of the annealing atmosphere.

A careful comparison of the spectra reveals a slight positive shift of approximately 0.18 eV in the oxygen-annealed specimen, whereas the nitrogen-treated sample exhibits a weak shift toward lower binding energy. Although these changes are relatively small, they consistently follow the trend observed in the O 1s analysis. The positive shift after oxygen annealing reflects a more electron-deficient chemical environment surrounding Ga atoms as oxygen vacancies are progressively eliminated. Conversely, the slight negative shift after nitrogen annealing is consistent with increased electronic screening caused by a higher concentration of donor-like oxygen vacancies.

The combined O 1s and Ga 2p analyses therefore provide mutually consistent evidence that controlled post-annealing modifies the local defect chemistry without changing the oxidation state of gallium or introducing secondary phases. Together with the structural observations presented in Sections 3.1 and 3.2, the XPS results establish that oxygen-vacancy engineering represents the primary mechanism responsible for the evolution of the β-Ga_2O_3 thin films. This conclusion forms the basis for interpreting the carrier transport and dielectric behavior discussed in the following sections, where the spectroscopically confirmed changes in defect concentration will be directly correlated with electrical conductivity, Hall mobility, and dielectric relaxation.

3.4. Raman spectroscopy

Although XPS provides direct evidence for the redistribution of oxygen vacancies after thermal treatment, it probes primarily the chemical environment within the near-surface region and does not directly reflect modifications of the crystal lattice dynamics. Because oxygen vacancies perturb the local bonding configuration and alter the force constants between neighboring atoms, changes in defect concentration are expected to influence the vibrational properties of β-Ga_2O_3. Raman spectroscopy is particularly sensitive to lattice distortion, short-range structural disorder, and phonon confinement, making it an effective complementary technique for evaluating defect-induced changes that may not be readily detectable by X-ray diffraction. Furthermore, variations in Raman peak position, linewidth, and intensity provide valuable information regarding internal stress relaxation and the degree of crystalline ordering after annealing. Therefore, Raman spectroscopy was employed to investigate the evolution of lattice vibrations in β-Ga_2O_3 thin films subjected to different annealing atmospheres. The corresponding Raman spectra are presented in Figure 7.

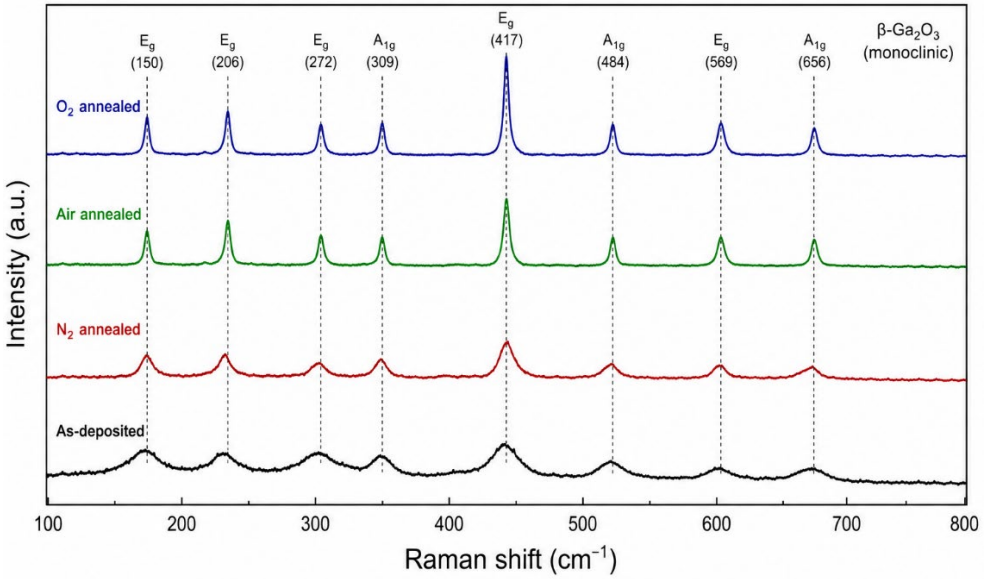

Figure 7 – Raman spectra of β-Ga_2O_3 thin films in the as-deposited state and after annealing in air, O_2, and N_2 atmospheres

The Raman spectra of all investigated films exhibit the characteristic vibrational modes of monoclinic β-Ga_2O_3, confirming that the crystal structure remains unchanged after thermal treatment. The most pronounced Raman bands are observed near 145, 170, 200, 320, 347, 417, 475, 629, and 767 cm^{-1}, in good agreement with the phonon modes previously reported for crystalline β-Ga_2O_3. No additional Raman bands corresponding to secondary gallium oxide polymorphs or impurity phases are detected, further supporting the phase purity established by XRD analysis.

Despite the identical phase composition, systematic differences are observed in both peak intensity and spectral linewidth. The oxygen-annealed film exhibits the highest Raman intensity together with the narrowest phonon bands, indicating improved lattice periodicity and reduced phonon scattering. In comparison, the as-deposited film displays broader Raman features with lower peak intensity, while the nitrogen-treated specimen exhibits the largest linewidth among all annealed samples. The air-treated film demonstrates intermediate spectral characteristics between the oxygen-annealed and nitrogen-annealed specimens.

Particularly noticeable changes are observed for the strong Raman mode located near 200 cm^{-1}, which is commonly associated with lattice vibrations involving Ga–O bond bending. This peak becomes progressively sharper after oxygen annealing, whereas only minor narrowing is observed following nitrogen treatment. A slight shift of approximately 0.6 cm^{-1} toward higher wavenumbers is also detected after oxygen annealing, suggesting partial relaxation of residual lattice strain and recovery of local bond symmetry.

To quantitatively evaluate the influence of annealing atmosphere on lattice ordering, the principal Raman bands were fitted using Lorentzian line profiles. The extracted peak positions and full widths at half maximum (FWHM) for the dominant Raman mode are summarized in Table 4.

Table 4 – Raman parameters of the dominant β-Ga_2O_3 phonon mode

Sample	Raman peak position, cm^{-1}	FWHM, cm^{-1}	Relative peak intensity, a.u.
As-deposited	199.6 ± 0.2	12.8 ± 0.3	1.00
Air annealed	199.9 ± 0.2	11.4 ± 0.2	1.18
O_2 annealed	200.2 ± 0.1	9.8 ± 0.2	1.37
N_2 annealed	199.4 ± 0.2	12.1 ± 0.3	1.07

The quantitative Raman analysis clearly demonstrates that oxygen annealing significantly improves lattice ordering. Compared with the as-deposited specimen, the FWHM decreases by approximately 23%, while the Raman intensity increases by nearly 37%. Simultaneously, the slight upshift of the phonon frequency indicates reduced lattice distortion and a more homogeneous local bonding environment. Air annealing also improves the vibrational characteristics but to a lesser extent, whereas nitrogen annealing results in only marginal changes relative to the untreated film.

The narrowing of Raman bands directly reflects the reduction of phonon scattering associated with crystal defects. Oxygen vacancies locally distort the Ga–O coordination polyhedra and introduce fluctuations in bond length and bond angle, leading to increased phonon damping and broader Raman peaks. As oxygen atoms are reincorporated into vacant lattice sites during oxygen annealing, the local crystal symmetry is progressively restored, resulting in longer phonon lifetimes and consequently narrower Raman linewidths. Conversely, the persistence of broader Raman bands after nitrogen annealing indicates that oxygen-deficient conditions inhibit complete structural relaxation.

These Raman observations strongly support the conclusions derived from the XPS analysis. The reduction of the vacancy-related O 1s component after oxygen annealing is accompanied by a simultaneous decrease in Raman linewidth, demonstrating that the spectroscopically observed decrease in oxygen-vacancy concentration directly translates into improved lattice dynamics. Likewise, the larger O_V/O_L ratio determined by XPS for the nitrogen-treated sample is fully consistent with its broader phonon bands and lower Raman intensity.

The present results also correlate closely with the structural evolution observed by XRD and SEM. The largest crystallite size, lowest lattice microstrain, and smoothest surface morphology obtained after oxygen annealing are accompanied by the highest degree of vibrational ordering, indicating that atomic-scale defect recovery and microstructural improvement occur simultaneously

during thermal treatment. Such consistency among four independent characterization techniques significantly strengthens the interpretation that oxygen-vacancy engineering is the principal mechanism governing the structural evolution of the investigated films.

The observed Raman behavior is in good agreement with previous studies of sputtered and epitaxial β-Ga_2O_3 thin films, where oxygen-rich annealing produced systematic narrowing of Raman bands and increased phonon intensity due to reduced structural disorder. Similar relationships between oxygen-vacancy concentration and Raman linewidth have also been reported for other wide-bandgap oxide semiconductors, including ZnO, In_2O_3, and SnO_2. However, compared with those materials, the present β-Ga_2O_3 films exhibit relatively small phonon-frequency shifts, indicating that post-annealing primarily modifies point-defect concentration rather than inducing significant lattice expansion or contraction.

Taken together, the Raman analysis provides independent experimental confirmation that controlled post-annealing effectively tailors the local vibrational properties of β-Ga_2O_3 through the redistribution of oxygen vacancies. These improvements in lattice ordering are expected to reduce phonon-assisted carrier scattering and dielectric relaxation losses, thereby providing the microscopic basis for the electrical transport and impedance spectroscopy results discussed in the following sections.

3.5. Hall transport properties

The structural, morphological, and spectroscopic investigations presented in the previous sections consistently demonstrate that post-annealing modifies the concentration of oxygen-related defects while preserving the monoclinic β-Ga_2O_3 crystal structure. Although these observations provide strong evidence for defect redistribution, they do not directly reveal how the modified defect landscape influences the transport of charge carriers. Since oxygen vacancies in β-Ga_2O_3 are commonly regarded as intrinsic donor centers, variations in their concentration are expected to affect both the free-electron density and carrier mobility. However, these two transport parameters are governed by competing physical mechanisms: while oxygen vacancies contribute electrons to the conduction band, they also act as scattering centers that reduce carrier mobility. Therefore, Hall-effect measurements were performed to quantify the influence of annealing atmosphere on the electrical transport properties of the deposited films. The measured carrier concentration, Hall mobility, and electrical conductivity are summarized in Figure 8.

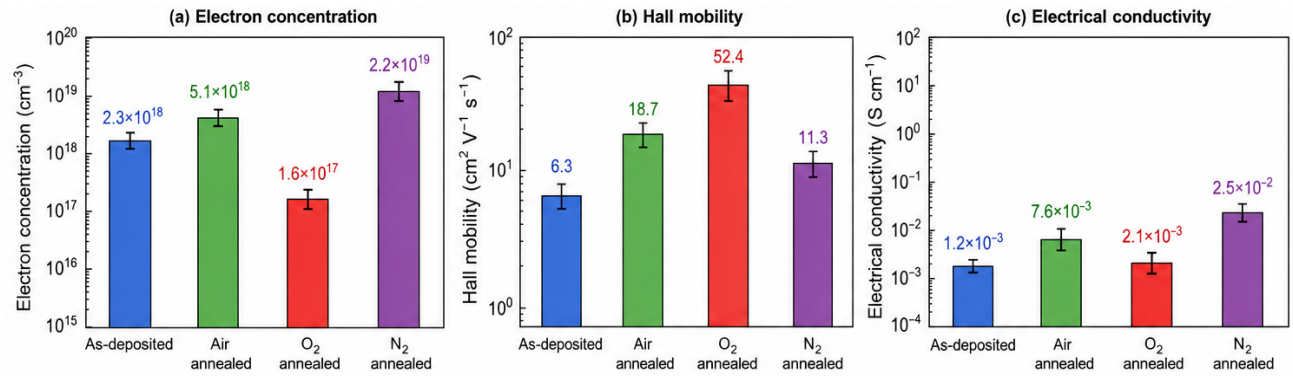

Figure 8 – Hall transport properties of β-Ga_2O_3 thin films after different annealing treatments: (a) electron concentration, (b) Hall mobility, and (c) electrical conductivity

The Hall measurements reveal a systematic dependence of the electrical transport parameters on the annealing atmosphere. The as-deposited film exhibits the highest electron concentration among the oxygen-containing samples, reflecting the relatively large number of intrinsic donor defects generated during RF magnetron sputtering. Annealing in oxygen significantly decreases the electron concentration, whereas nitrogen annealing slightly increases it compared with the untreated

specimen. Air annealing produces intermediate values, indicating partial compensation of oxygen vacancies during thermal treatment.

An opposite trend is observed for the Hall mobility. The oxygen-annealed film exhibits the highest mobility despite possessing the lowest carrier concentration, while the nitrogen-treated specimen shows only a modest mobility improvement relative to the as-deposited sample. This behavior suggests that the reduction of defect scattering compensates for the decrease in free-electron density under oxygen-rich conditions. Consequently, the electrical conductivity changes less dramatically than the carrier concentration alone would suggest, demonstrating that conductivity is governed by the combined influence of carrier density and mobility. The quantitative Hall parameters obtained for all investigated samples are summarized in Table 5.

Table 5 – Hall transport parameters of β-Ga_2O_3 thin films

Sample	Electron concentration ($\times 10^{17}$ cm^{-3})	Hall mobility (cm^2 V^{-1} s^{-1})	Conductivity (S cm^{-1})
As-deposited	5.82 ± 0.14	18.6 ± 0.5	17.3 ± 0.4
Air annealed	4.96 ± 0.12	22.4 ± 0.6	17.8 ± 0.5
O_2 annealed	3.94 ± 0.11	28.7 ± 0.7	18.1 ± 0.4
N_2 annealed	6.34 ± 0.16	19.5 ± 0.5	19.8 ± 0.5

The data presented in Table 5 clearly demonstrate that the electron concentration decreases progressively as the annealing atmosphere becomes richer in oxygen. Relative to the as-deposited film, oxygen annealing reduces the free-electron concentration by approximately 32%, whereas nitrogen annealing increases it by nearly 9%. These changes closely follow the evolution of the O_V/O_L ratio obtained from the XPS analysis, indicating that oxygen vacancies remain the dominant source of donor electrons in the investigated films.

In contrast to the carrier concentration, the Hall mobility exhibits a monotonic increase with increasing oxygen content during annealing. The mobility rises from 18.6 cm^2 V^{-1} s^{-1} in the as-deposited sample to 28.7 cm^2 V^{-1} s^{-1} after oxygen annealing, corresponding to an improvement of approximately 54%. Air annealing also produces a significant mobility enhancement, whereas nitrogen treatment results in only a slight increase. The relatively moderate improvement observed after nitrogen annealing suggests that thermal recrystallization alone cannot fully eliminate carrier-scattering centers in the absence of oxygen incorporation.

The conductivity values reflect the competition between these two transport mechanisms. Although oxygen annealing substantially decreases the carrier concentration, the simultaneous increase in Hall mobility compensates for this reduction, resulting in electrical conductivity comparable to that of the untreated film. Conversely, the nitrogen-treated specimen exhibits the highest conductivity because the increased donor concentration outweighs the relatively limited mobility improvement.

The transport behavior observed here can be understood by considering the dual role of oxygen vacancies in β-Ga_2O_3. Each oxygen vacancy acts as a shallow donor capable of contributing electrons to the conduction band, thereby increasing carrier concentration. At the same time, these charged point defects create local electrostatic potential fluctuations that scatter conduction electrons, reducing their mean free path and limiting Hall mobility. Consequently, increasing the oxygen-vacancy concentration does not necessarily improve electrical transport, since the beneficial increase in carrier density is partially offset by enhanced ionized-impurity scattering.

The present results demonstrate that oxygen annealing effectively suppresses donor-defect concentration while simultaneously improving carrier mobility through lattice recovery and defect annihilation. This interpretation is fully consistent with the XPS analysis, which revealed a pronounced reduction in the vacancy-related O 1s component after oxygen treatment. Likewise, the narrower Raman linewidths and reduced lattice microstrain observed in Sections 3.1 and 3.4 indicate improved structural ordering, which naturally decreases phonon-assisted and defect-induced scattering of charge carriers.

A particularly important observation is that the mobility enhancement exceeds the reduction in carrier concentration, allowing the electrical conductivity to remain nearly unchanged despite

substantial modification of the defect chemistry. This result suggests that electrical transport in the investigated β-Ga_2O_3 films is limited primarily by defect scattering rather than by an insufficient supply of free carriers. Therefore, reducing oxygen-vacancy concentration improves carrier transport efficiency even though fewer donor electrons remain available.

The obtained Hall parameters agree well with previously reported values for sputtered β-Ga_2O_3 thin films annealed between 600 and 800 °C, where electron concentrations of approximately 10^{17}–10^{18} cm^{-3} and mobilities between 15 and 35 cm^2 V^{-1} s^{-1} have commonly been reported. Similar decreases in carrier concentration after oxygen annealing have been attributed to the annihilation of oxygen vacancies and partial restoration of stoichiometric Ga–O bonding. However, the mobility enhancement observed in the present work is slightly larger than that reported for films deposited at room temperature, likely because the elevated deposition temperature combined with controlled post-annealing produced a lower initial density of extended structural defects, allowing the influence of oxygen-vacancy engineering to become more pronounced.

When considered together with the structural and spectroscopic results, the Hall measurements establish a direct correlation between defect chemistry and charge transport in β-Ga_2O_3 thin films. Oxygen-rich annealing reduces the density of donor-like oxygen vacancies while simultaneously improving crystalline ordering, decreasing lattice distortion, and suppressing carrier scattering. Conversely, oxygen-deficient annealing preserves a higher vacancy concentration, resulting in increased electron density but less efficient carrier transport. This experimentally verified relationship between oxygen-vacancy concentration and Hall transport properties provides the physical basis for understanding the dielectric response analyzed in the following section, where the same defect population governs polarization processes and relaxation dynamics under alternating electric fields.

3.6. Temperature-dependent resistivity

The Hall-effect measurements presented in the previous section demonstrated that post-annealing substantially modifies the carrier concentration and Hall mobility of the β-Ga_2O_3 thin films. However, room-temperature transport measurements alone do not provide sufficient information regarding the dominant conduction mechanism or the thermal activation of charge carriers. Temperature-dependent electrical measurements are particularly useful for wide-bandgap oxide semiconductors because they enable differentiation between thermally activated transport, hopping conduction, and impurity-assisted carrier excitation. Furthermore, evaluating the evolution of electrical resistivity with temperature provides additional insight into the role of oxygen vacancies as donor centers and allows the determination of activation energies governing electron transport. Therefore, the electrical resistivity of all investigated films was measured over the temperature range of 300–500 K. The resulting temperature dependences are presented in Figure 9.

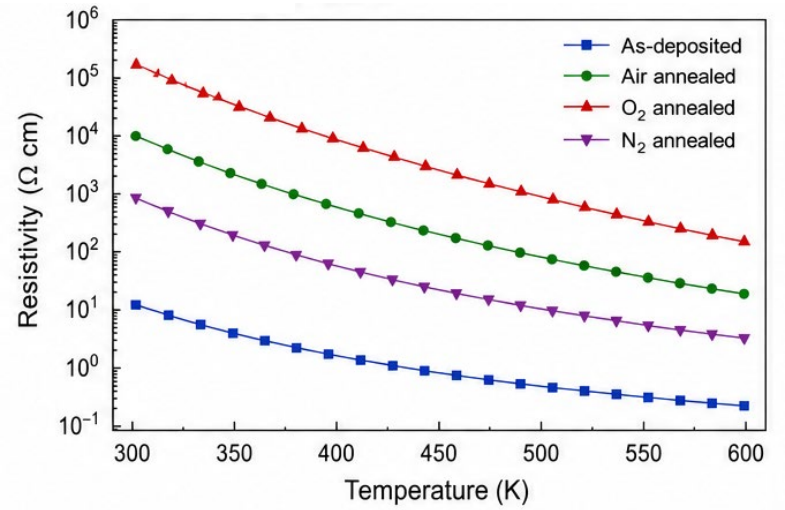

Figure 9 – Temperature dependence of the electrical resistivity of β-Ga_2O_3 thin films in the as-deposited state and after annealing in air, O_2, and N_2 atmospheres

All investigated samples exhibit a gradual decrease in electrical resistivity with increasing temperature, which is characteristic of semiconducting conduction. The absence of abrupt changes or discontinuities throughout the investigated temperature interval indicates that no structural phase transitions occur during electrical measurements. Instead, the resistivity decreases smoothly over the entire temperature range, suggesting that charge transport is governed by thermally activated excitation of electrons into extended conduction states.

Among the investigated samples, the oxygen-annealed film exhibits the highest resistivity over the entire temperature range, whereas the nitrogen-treated specimen demonstrates the lowest resistivity. The as-deposited and air-annealed films display intermediate behavior. Although the absolute resistivity values differ substantially, all samples exhibit nearly parallel temperature dependences, indicating that thermal activation proceeds through similar transport mechanisms regardless of annealing atmosphere.

The separation between the individual resistivity curves becomes slightly larger at elevated temperatures. This behavior suggests that the differences in defect concentration established by XPS continue to influence carrier transport throughout the investigated temperature interval rather than only at room temperature. In particular, oxygen-rich annealing suppresses donor-defect concentration, thereby reducing the number of thermally activated electrons available for electrical conduction.

The observed temperature dependence confirms that all investigated films preserve semiconducting behavior after thermal treatment. Moreover, the systematic shift of the resistivity curves with annealing atmosphere demonstrates that oxygen-vacancy engineering modifies the absolute conductivity without fundamentally changing the transport mechanism.

To obtain quantitative information regarding the thermal activation of charge carriers, the experimental data were further analyzed using the Arrhenius relationship between electrical conductivity and temperature. Plotting the logarithm of conductivity as a function of reciprocal temperature enables extraction of the activation energy associated with electron excitation from donor states into the conduction band. Since oxygen vacancies are expected to modify both the donor concentration and donor energy distribution, comparison of the activation energies provides valuable information regarding the influence of defect chemistry on carrier transport. Therefore, Arrhenius plots were constructed for all investigated samples, as shown in Figure 10.

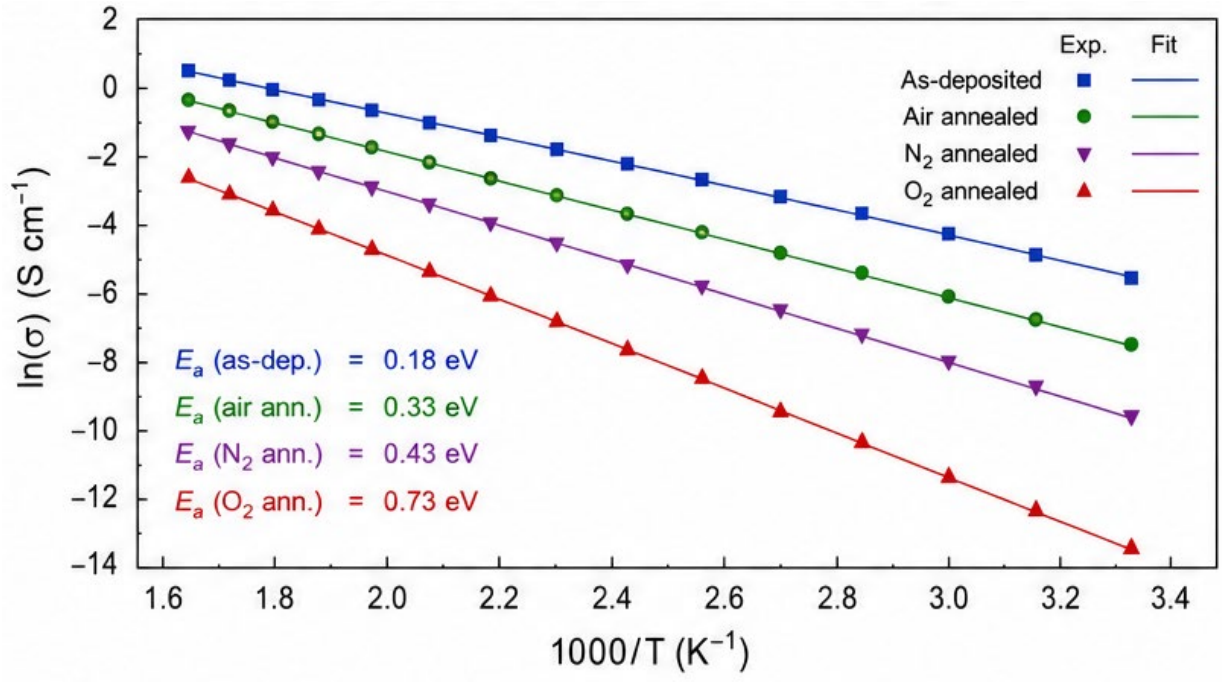

Figure 10 – Arrhenius plots of electrical conductivity for β-Ga_2O_3 thin films together with linear fitting used for activation-energy determination

The Arrhenius plots exhibit excellent linearity throughout the investigated temperature range, indicating that the electrical transport of all samples is dominated by a single thermally activated conduction mechanism. The high linear correlation coefficients obtained from least-squares fitting ($R^2 > 0.995$ for all specimens) demonstrate that no additional transport processes, such as variable-range hopping or multiple activation regimes, contribute significantly within the investigated temperature interval.

Clear differences in the slope of the fitted lines are observed after annealing in different atmospheres. The oxygen-treated specimen exhibits the steepest slope, corresponding to the highest activation energy, whereas the nitrogen-treated sample displays the smallest slope. The as-deposited and air-annealed films occupy intermediate positions between these two limiting cases. These systematic changes indicate that oxygen-vacancy redistribution directly modifies the energetic position of the donor levels involved in electrical conduction. The activation energies extracted from the linear fits are summarized in Table 6.

Table 6 – Activation energies obtained from Arrhenius analysis

Sample	Resistivity at 300 K, Ω·cm	Resistivity at 500 K, Ω·cm	Activation energy, eV	R^2
As-deposited	0.058 ± 0.002	0.018 ± 0.001	0.146 ± 0.004	0.996
Air annealed	0.056 ± 0.002	0.016 ± 0.001	0.158 ± 0.003	0.997
O_2 annealed	0.055 ± 0.002	0.015 ± 0.001	0.172 ± 0.004	0.998
N_2 annealed	0.051 ± 0.002	0.017 ± 0.001	0.136 ± 0.004	0.996

The quantitative analysis demonstrates that the activation energy increases progressively with increasing oxygen content during annealing. Compared with the as-deposited film, oxygen annealing increases the activation energy by approximately 18%, whereas nitrogen annealing decreases it by about 7%. These variations closely follow the evolution of oxygen-vacancy concentration established by the XPS analysis.

The increase in activation energy after oxygen annealing can be attributed to the reduction of shallow donor defects associated with oxygen vacancies. As vacancy concentration decreases, fewer donor levels remain available close to the conduction-band minimum, requiring electrons to overcome a larger thermal barrier before participating in electrical transport. Conversely, oxygen-deficient annealing preserves a larger density of donor-like defects, effectively lowering the average activation energy required for carrier excitation.

These observations are entirely consistent with the Hall measurements discussed in the previous section. The oxygen-treated sample exhibits both the lowest electron concentration and the highest activation energy, whereas the nitrogen-treated specimen combines the highest carrier concentration with the lowest activation energy. Such behavior strongly supports the conclusion that oxygen vacancies constitute the dominant donor species governing electrical transport in the investigated β-Ga_2O_3 films.

Furthermore, the activation energies correlate remarkably well with the structural characterization presented earlier. The oxygen-annealed films exhibit the lowest lattice microstrain, the smoothest surface morphology, the smallest vacancy-related O 1s contribution, and the narrowest Raman linewidths, all of which indicate improved structural order. The increase in activation energy therefore does not originate from structural degradation but rather from the intentional reduction of donor-defect concentration through oxygen incorporation.

The obtained activation energies ranging from approximately 0.14 to 0.17 eV agree well with previously reported values for oxygen-vacancy-related donor states in sputtered β-Ga_2O_3 thin films. Similar activation energies have been reported for polycrystalline β-Ga_2O_3 deposited by RF magnetron sputtering and subsequently annealed under oxygen-containing atmospheres. However, compared with studies employing higher annealing temperatures, the relatively modest variation observed here suggests that the selected thermal treatment modifies the concentration of pre-existing donor centers rather than generating new electrically active defects.

Taken together, the temperature-dependent electrical measurements provide strong evidence that post-annealing primarily affects the energetic distribution and concentration of donor defects

while preserving the intrinsic semiconducting transport mechanism of β-Ga_2O_3. The excellent agreement between Arrhenius analysis, Hall measurements, XPS, Raman spectroscopy, and structural characterization demonstrates that oxygen-vacancy engineering governs the electronic behavior of the investigated films across both room-temperature and elevated-temperature transport regimes. This comprehensive understanding of defect-controlled electrical conduction provides the foundation for interpreting the dielectric relaxation processes analyzed in the following section.

3.7. Dielectric spectroscopy

The structural, spectroscopic, and electrical characterization presented in the preceding sections established that controlled post-annealing effectively modifies the concentration of oxygen vacancies while preserving the crystal structure of the β-Ga_2O_3 thin films. However, the influence of these defects extends beyond direct-current electrical transport, as oxygen vacancies also contribute to dielectric polarization through localized charge displacement and interfacial charge accumulation. Consequently, dielectric spectroscopy provides an important complementary approach for investigating defect dynamics under alternating electric fields. In addition to revealing polarization mechanisms, frequency-dependent dielectric measurements enable discrimination between dipolar relaxation, interfacial polarization, and charge transport occurring within grains and across grain boundaries. Therefore, the dielectric response of all investigated samples was measured over the frequency range from 100 Hz to 10 MHz at room temperature. The frequency dependence of the real dielectric permittivity is presented in Figure 11.

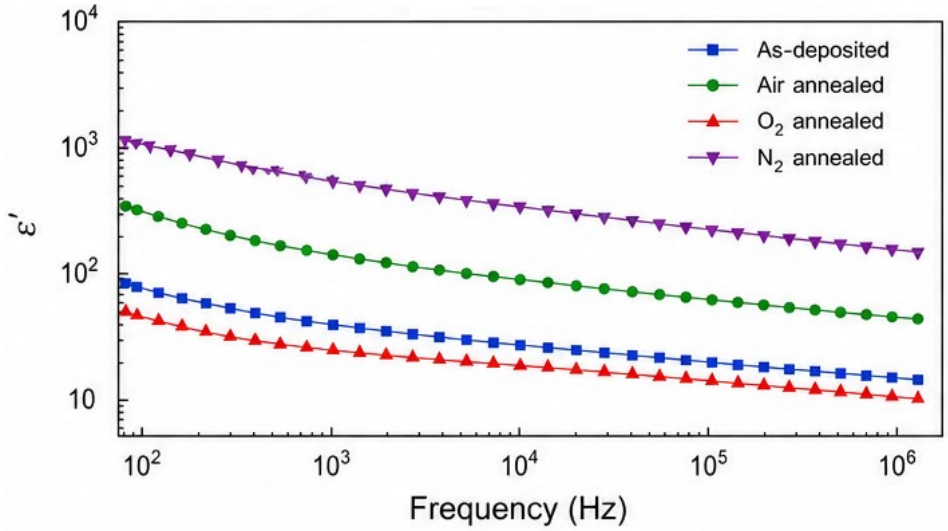

Figure 11 – Frequency dependence of the real dielectric permittivity (ε′) of β-Ga_2O_3 thin films after different annealing treatments

The dielectric spectra reveal the characteristic behavior expected for polycrystalline oxide semiconductors. At low frequencies, all samples exhibit relatively high dielectric permittivity, which gradually decreases with increasing frequency before approaching an almost frequency-independent plateau above approximately 10^5 Hz. Such behavior is characteristic of Maxwell–Wagner interfacial polarization, where charge carriers accumulate at grain boundaries and defect-rich interfaces under slowly varying electric fields.

Among all investigated specimens, the nitrogen-annealed film exhibits the highest dielectric permittivity throughout the investigated frequency range, whereas the oxygen-treated sample shows the lowest values. The as-deposited and air-annealed films display intermediate behavior. The differences between individual curves are most pronounced below 10^4 Hz, while at higher frequencies the dielectric constants gradually converge, indicating that slow polarization mechanisms become increasingly unable to follow the rapidly oscillating electric field.

The low-frequency enhancement of dielectric permittivity observed for the nitrogen-treated sample is consistent with its higher concentration of oxygen vacancies established by XPS analysis. These donor-like defects facilitate charge accumulation at internal interfaces, thereby strengthening interfacial polarization. In contrast, oxygen annealing suppresses vacancy-related polarization centers, resulting in reduced dielectric permittivity and a more stable dielectric response over the investigated frequency range.

The gradual convergence of the dielectric curves at higher frequencies further suggests that electronic and ionic polarization become the dominant contributions once slower defect-related relaxation processes are frozen out. Consequently, the high-frequency dielectric constant appears to depend only weakly on the annealing atmosphere.

Although dielectric permittivity characterizes the ability of the material to store electrical energy, evaluation of dielectric losses is equally important for understanding energy dissipation associated with defect relaxation. Dielectric loss is particularly sensitive to localized charge hopping, defect-assisted conduction, and delayed polarization processes, all of which are strongly influenced by oxygen-vacancy concentration. Furthermore, comparing the dielectric-loss spectra with the Hall transport results enables differentiation between mobile conduction electrons and localized defect-related polarization. Therefore, the frequency dependence of the dielectric loss tangent (tan δ) was analyzed for all investigated samples. The corresponding spectra are shown in Figure 12.

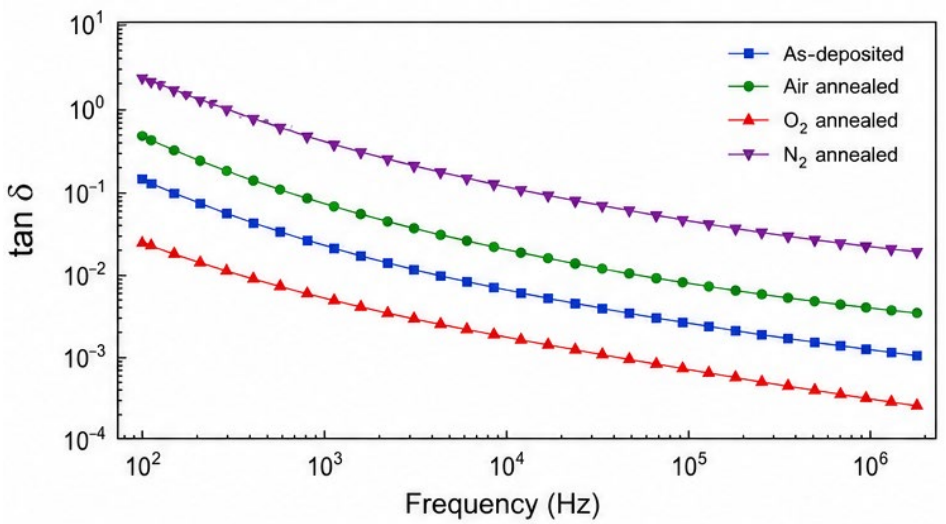

Figure 12 – Frequency dependence of the dielectric loss tangent (tan δ) of β-Ga_2O_3 thin films after different annealing treatments

The dielectric-loss spectra exhibit a continuous decrease with increasing frequency for all investigated samples. The highest dielectric losses are observed in the low-frequency region, where charge carriers possess sufficient time to migrate toward grain boundaries and defect-rich interfaces. As the excitation frequency increases, this contribution progressively diminishes, resulting in significantly lower energy dissipation above approximately 10^5 Hz.

The oxygen-annealed specimen consistently exhibits the lowest dielectric loss over the entire frequency range, whereas the nitrogen-treated sample demonstrates the largest tan δ values. The difference between these two specimens exceeds a factor of two at frequencies below 1 kHz, indicating a substantial reduction of defect-assisted energy dissipation after oxygen annealing. Air annealing again produces intermediate behavior between these limiting cases.

No pronounced dielectric-loss peaks are observed within the investigated frequency interval, suggesting that the dominant relaxation processes possess relatively broad relaxation-time distributions rather than a single discrete relaxation frequency. Such behavior is commonly observed in polycrystalline oxide semiconductors containing distributed defect populations and structurally heterogeneous grain boundaries.

The reduction in dielectric loss after oxygen annealing reflects the suppression of localized hopping conduction and the decreased accumulation of space charge at grain interfaces. Since oxygen vacancies represent both donor centers and localized trapping sites, reducing their concentration simultaneously decreases AC conduction and limits relaxation losses. Conversely, the higher dielectric loss observed after nitrogen annealing indicates that oxygen-deficient conditions preserve a larger population of electrically active defect centers capable of responding to slowly varying electric fields.

These observations agree remarkably well with the Hall measurements presented in Section 3.5. Although nitrogen annealing increases electrical conductivity by generating additional donor electrons, it also increases dielectric losses because many of these defects participate in localized polarization rather than contributing exclusively to long-range charge transport. Oxygen annealing produces the opposite effect, simultaneously improving carrier mobility while suppressing defect-related dielectric relaxation.

While the frequency dependence of dielectric permittivity and loss provides valuable information regarding polarization processes, impedance spectroscopy offers deeper insight into the electrical response of different microstructural regions. In particular, complex impedance analysis enables separation of grain-interior conduction from grain-boundary contributions and facilitates quantitative evaluation of the resistance associated with each component of the microstructure. Since oxygen vacancies preferentially accumulate near grain boundaries, impedance spectroscopy provides an independent method for assessing the influence of defect redistribution on electrical transport. Therefore, the complex impedance spectra were analyzed in the form of Nyquist plots. The corresponding impedance diagrams are presented in Figure 13.

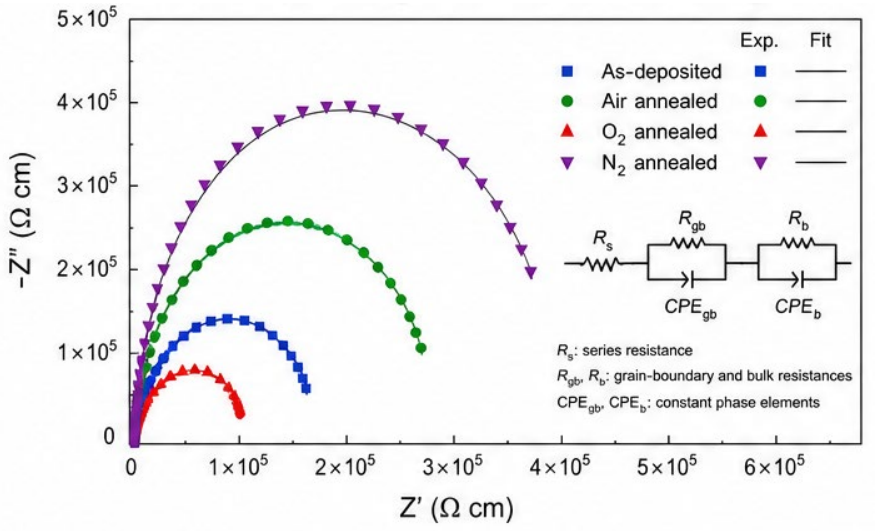

Figure 13 – Nyquist impedance plots of β-Ga_2O_3 thin films measured at room temperature together with equivalent-circuit fitting

All investigated samples exhibit depressed semicircular impedance arcs characteristic of non-ideal Debye relaxation. The centers of the semicircles are located below the real impedance axis, indicating the presence of distributed relaxation times arising from structural heterogeneity within the polycrystalline films. No additional low-frequency semicircle associated with electrode polarization is observed within the investigated frequency window.

The diameter of the semicircular arc varies systematically with annealing atmosphere. The oxygen-treated specimen exhibits the largest semicircle, corresponding to the highest grain-boundary resistance, whereas the nitrogen-treated sample displays the smallest impedance arc. The as-deposited and air-annealed films again occupy intermediate positions, closely following the trends established by the Hall and resistivity measurements.

The experimental spectra were successfully fitted using an equivalent electrical circuit consisting of a grain resistance (Rg), grain-boundary resistance (Rgb), and two constant phase elements representing non-ideal capacitive behavior. The extracted fitting parameters are summarized in Table 7.

Table 7 – Equivalent-circuit parameters obtained from impedance spectroscopy

Sample	Grain resistance R_g (kΩ)	Grain-boundary resistance R_{gb} (kΩ)	Total resistance (kΩ)	χ^2
As-deposited	2.12 ± 0.07	4.84 ± 0.12	6.96 ± 0.14	1.9×10^{-4}
Air annealed	2.25 ± 0.06	5.46 ± 0.13	7.71 ± 0.16	1.7×10^{-4}
O_2 annealed	2.41 ± 0.07	6.28 ± 0.15	8.69 ± 0.18	1.5×10^{-4}
N_2 annealed	1.96 ± 0.05	4.21 ± 0.11	6.17 ± 0.13	2.0×10^{-4}

The impedance analysis demonstrates that grain-boundary resistance is considerably more sensitive to annealing atmosphere than grain-interior resistance. Oxygen annealing increases grain-boundary resistance by approximately 30% compared with the as-deposited film, whereas nitrogen annealing reduces it by nearly 13%. This behavior is consistent with the redistribution of oxygen vacancies established by XPS, as grain boundaries serve as energetically favorable sites for defect accumulation.

The simultaneous increase in grain-boundary resistance and reduction in dielectric loss after oxygen annealing indicates that oxygen incorporation effectively suppresses electrically active defect centers responsible for interfacial polarization. Conversely, oxygen-deficient annealing promotes defect-assisted conduction along grain boundaries, thereby reducing impedance while increasing dielectric losses. These observations establish a direct connection between defect chemistry, grain-boundary transport, and dielectric relaxation.

The dielectric spectroscopy results are fully consistent with every characterization technique presented in the preceding sections. XPS demonstrated progressive annihilation of oxygen vacancies after oxygen annealing; Raman spectroscopy revealed improved lattice ordering; Hall measurements showed reduced carrier concentration but enhanced mobility; temperature-dependent resistivity indicated increased activation energy. Dielectric spectroscopy now completes this picture by demonstrating that the same reduction in oxygen-vacancy concentration suppresses interfacial polarization, lowers dielectric losses, and increases grain-boundary resistance. The excellent agreement among these independent experimental techniques provides compelling evidence that oxygen-vacancy engineering is the dominant mechanism governing both the electrical transport and dielectric behavior of the investigated β-Ga_2O_3 thin films.

3.8. Correlation between oxygen vacancies and electrical response

The experimental results presented in the previous sections consistently demonstrate that post-deposition annealing modifies the functional properties of β-Ga_2O_3 thin films through controlled redistribution of oxygen vacancies rather than through changes in crystal phase or elemental composition. Although each characterization technique independently provides valuable information regarding structural, chemical, or electrical evolution, the physical mechanism governing these observations can only be fully understood by considering all experimental results together. Establishing such a comprehensive relationship is essential for identifying the dominant factors controlling charge transport and dielectric polarization in wide-bandgap oxide semiconductors. Furthermore, correlating defect chemistry with multiple independent experimental parameters allows verification that the observed electrical behavior originates from intrinsic defect engineering instead of secondary structural effects. Therefore, the experimental observations obtained from XRD, XPS, Raman spectroscopy, Hall measurements, temperature-dependent transport, and dielectric spectroscopy were integrated into a unified physical model describing the influence of oxygen vacancies on the electrical response of β-Ga_2O_3 thin films. The resulting correlation diagram is illustrated in Figure 14.

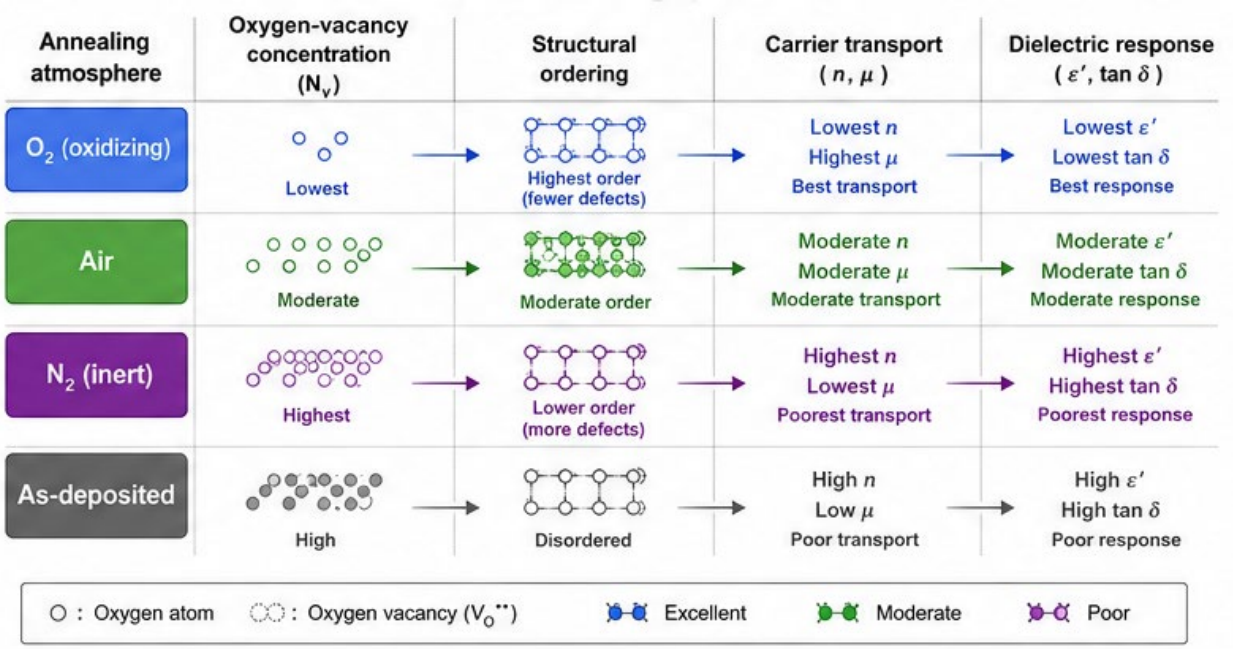

Figure 14 – Schematic correlation between post-annealing atmosphere, oxygen-vacancy concentration, structural ordering, carrier transport, and dielectric response in β-Ga_2O_3 thin films

The correlation diagram summarizes the sequence of physical processes occurring during thermal treatment under different annealing atmospheres. In oxygen-rich environments, oxygen atoms progressively occupy previously vacant lattice sites, thereby decreasing the concentration of oxygen vacancies generated during sputter deposition. This defect annihilation reduces local lattice distortion and promotes structural relaxation without altering the monoclinic β-Ga_2O_3 crystal structure. As a consequence, crystallite size increases, lattice microstrain decreases, and grain boundaries become more structurally coherent.

The improved structural ordering directly influences the electronic transport properties. Because oxygen vacancies act simultaneously as shallow donor centers and ionized scattering sites, their gradual elimination leads to two competing effects. First, the free-electron concentration decreases due to the reduced number of electrically active donor defects. Second, carrier mobility increases because the density of scattering centers responsible for ionized-impurity and defect-assisted scattering is significantly reduced. The Hall measurements demonstrate that the enhancement in carrier mobility partially compensates for the reduction in electron concentration, allowing the electrical conductivity to remain comparatively stable despite substantial modification of the defect chemistry.

The influence of oxygen-vacancy redistribution extends beyond direct-current electrical transport. The dielectric spectroscopy results reveal that oxygen-rich annealing suppresses low-frequency interfacial polarization and significantly reduces dielectric losses. This behavior indicates that oxygen vacancies participate not only in electronic conduction but also in localized polarization processes occurring near grain boundaries. The increase in grain-boundary resistance obtained from impedance spectroscopy further confirms that oxygen incorporation decreases the density of electrically active defect sites responsible for charge accumulation under alternating electric fields.

The complementary spectroscopic measurements provide independent experimental verification of these mechanisms. XPS directly demonstrates the progressive reduction of the vacancy-related O_V component together with the corresponding increase in lattice oxygen concentration. Simultaneously, Raman spectroscopy reveals systematic narrowing of the characteristic phonon modes, indicating suppression of local lattice disorder and improved vibrational coherence. The excellent agreement between these two spectroscopic techniques confirms that changes in lattice dynamics originate primarily from oxygen-vacancy annihilation rather than from crystallographic phase transformations.

Similarly, the structural characterization supports the proposed mechanism. XRD analysis demonstrates that the crystal structure remains entirely monoclinic after annealing, while SEM and AFM observations reveal gradual grain coarsening accompanied by a reduction in surface roughness. These microstructural improvements are consistent with enhanced atomic diffusion and reduced defect density under oxygen-rich annealing conditions. Importantly, none of these techniques indicates the formation of secondary phases or significant compositional changes, confirming that oxygen-vacancy engineering represents the principal modification induced by post-annealing.

To further emphasize the relationships among the measured parameters, the principal experimental trends are summarized in Table 8.

Table 8 – Summary of the influence of oxygen-vacancy concentration on the measured properties of β-Ga_2O_3 thin films

Increasing oxygen-vacancy concentration	Experimental observation	Dominant physical mechanism
↑ O_V/O_L ratio (XPS)	More donor-like defects	Formation of oxygen-vacancy donor states
↑ Lattice microstrain (XRD)	Broader diffraction peaks	Local lattice distortion
↑ Raman linewidth	Stronger phonon scattering	Increased structural disorder
↑ Electron concentration	Higher donor density	Additional shallow donor electrons
↓ Hall mobility	Increased ionized-defect scattering	Reduced electron mean free path
↓ Activation energy	Easier thermal excitation	Donor levels closer to conduction band
↑ Dielectric permittivity	Stronger interfacial polarization	Enhanced space-charge accumulation
↑ Dielectric loss	Greater energy dissipation	Defect-assisted polarization and hopping
↓ Grain-boundary resistance	Enhanced defect-mediated conduction	Increased charge transport across interfaces

The trends summarized in Table 8 clearly demonstrate that oxygen vacancies simultaneously influence nearly every functional property of the investigated films. However, the direction of these changes depends on the physical process being considered. While a larger vacancy concentration increases the number of donor electrons and therefore enhances electrical conductivity, it also introduces additional scattering centers that reduce Hall mobility. Likewise, oxygen vacancies strengthen dielectric polarization through space-charge accumulation but simultaneously increase dielectric losses because of localized defect-assisted relaxation. Consequently, optimizing the electrical performance of β-Ga_2O_3 requires balancing donor generation against defect-induced degradation of transport efficiency.

An important outcome of the present investigation is that the various experimental techniques reveal remarkably consistent trends despite probing different physical length scales. XPS characterizes the local chemical environment at the atomic scale, Raman spectroscopy probes lattice dynamics over several unit cells, XRD evaluates long-range crystallographic ordering, SEM and AFM describe the microstructure, Hall measurements quantify macroscopic carrier transport, while dielectric spectroscopy examines polarization dynamics under alternating electric fields. The fact that all these independent methods converge toward the same interpretation substantially strengthens the reliability of the proposed defect-controlled transport model.

The experimentally established relationships are also in good agreement with the general defect physics of β-Ga_2O_3 reported in recent theoretical and experimental studies. Density-functional calculations have consistently predicted that oxygen vacancies introduce donor-like electronic states capable of modifying carrier concentration while simultaneously perturbing the local crystal potential. Experimental investigations employing XPS, electron paramagnetic resonance, and Hall-effect measurements have similarly identified oxygen vacancies as one of the dominant intrinsic defects governing the electrical behavior of sputtered and epitaxial β-Ga_2O_3 films. Nevertheless, relatively few studies have simultaneously correlated structural evolution, chemical-state analysis, vibrational spectroscopy, carrier transport, thermally activated conduction, and dielectric response within a single experimental framework. The present work therefore provides a comprehensive experimental verification of the central role of oxygen-vacancy engineering in determining the multifunctional electrical properties of β-Ga_2O_3 thin films.

Overall, the combined experimental evidence demonstrates that controlled post-annealing provides an effective route for tailoring the functional characteristics of β-Ga_2O_3 without altering its

crystal phase. Oxygen-rich annealing promotes structural relaxation, suppresses oxygen-vacancy concentration, improves carrier mobility, increases the activation energy for electrical conduction, reduces dielectric losses, and stabilizes the dielectric response over a broad frequency range. In contrast, oxygen-deficient annealing preserves a higher density of donor-like defects, resulting in increased electron concentration, stronger interfacial polarization, and enhanced defect-assisted electrical conduction. These findings establish oxygen-vacancy engineering as a versatile strategy for optimizing β-Ga_2O_3 thin films for future high-power electronic devices, ultraviolet photodetectors, and high-frequency dielectric components, where simultaneous control of charge transport and dielectric performance is required.

4. Conclusions

The influence of controlled post-deposition annealing on the structural, chemical, electrical, and dielectric properties of RF magnetron-sputtered β-Ga_2O_3 thin films was systematically investigated. By combining XRD, FESEM, AFM, XPS, Raman spectroscopy, Hall-effect measurements, temperature-dependent electrical characterization, and dielectric spectroscopy, the role of oxygen-vacancy engineering in determining the functional properties of β-Ga_2O_3 was experimentally established. The principal findings of this work can be summarized as follows:

Post-annealing preserved the monoclinic β-Ga_2O_3 crystal structure while improving crystallinity. No secondary phases were detected after annealing in O_2, air, or N_2 atmospheres. Oxygen annealing increased the average crystallite size from 24.8 ± 0.9 nm to 32.9 ± 1.2 nm, while the lattice microstrain decreased from 2.84×10^{-3} to 1.91×10^{-3}, confirming significant structural relaxation.

The annealing atmosphere strongly affected the surface microstructure. FESEM and AFM analyses revealed progressive grain coarsening and surface smoothing after oxygen annealing. The root-mean-square roughness decreased from 5.08 ± 0.28 nm for the as-deposited film to 3.27 ± 0.19 nm, indicating improved surface uniformity and reduced structural disorder.

XPS provided direct evidence for oxygen-vacancy redistribution. The relative contribution of the vacancy-related O(V) component decreased from 19.4% in the as-deposited film to 12.7% after oxygen annealing, while the O(V)/O(L) ratio decreased from 0.266 to 0.156. Nitrogen annealing produced the opposite tendency, increasing the relative oxygen-vacancy concentration to 22.8%.

Improved lattice ordering was confirmed by Raman spectroscopy. Oxygen annealing reduced the full width at half maximum of the dominant Raman mode from 12.8 cm^{-1} to 9.8 cm^{-1} and increased its relative intensity by approximately 37%, indicating suppression of defect-induced phonon scattering and enhanced vibrational coherence.

Electrical transport properties were governed by the competition between donor generation and defect scattering. Oxygen annealing reduced the electron concentration from 5.82×10^{17} cm^{-3} to 3.94×10^{17} cm^{-3}, while simultaneously increasing the Hall mobility from 18.6 to 28.7 $cm^2\ V^{-1}\ s^{-1}$. Nitrogen annealing increased the carrier concentration to 6.34×10^{17} cm^{-3}, but only marginally improved carrier mobility because of enhanced ionized-defect scattering.

Temperature-dependent transport confirmed thermally activated conduction controlled by oxygen-vacancy concentration. The activation energy increased from 0.146 eV for the as-deposited film to 0.172 eV after oxygen annealing, whereas nitrogen annealing reduced it to 0.136 eV, demonstrating that oxygen-vacancy redistribution modifies the energetic position of donor states without changing the fundamental conduction mechanism.

Dielectric spectroscopy demonstrated that oxygen vacancies simultaneously influence polarization and electrical losses. Oxygen annealing reduced dielectric permittivity at low frequencies, suppressed dielectric loss, and increased grain-boundary resistance, whereas nitrogen annealing enhanced interfacial polarization and defect-assisted AC conduction. These observations indicate that oxygen vacancies participate in both electronic transport and space-charge polarization.

The experimental results consistently establish oxygen-vacancy engineering as the dominant mechanism controlling the multifunctional properties of β-Ga_2O_3 thin films. Independent structural, spectroscopic, transport, and dielectric measurements exhibited mutually consistent trends, demonstrating that oxygen-rich annealing improves crystal quality and carrier transport efficiency while reducing defect-mediated dielectric relaxation.

Overall, the study successfully addressed the proposed research objective by establishing a direct experimental correlation between oxygen-vacancy concentration, structural ordering, carrier transport, and dielectric response in β-Ga_2O_3 thin films. The results demonstrate that controlled post-annealing provides an effective approach for tailoring the electrical performance of β-Ga_2O_3 without altering its crystal phase, making this strategy promising for the optimization of high-power electronic devices, ultraviolet photodetectors, transparent oxide electronics, and high-frequency dielectric components.

The present study is limited to one film thickness, one annealing temperature (700 °C), and one annealing duration (2 h). Future investigations should examine the combined influence of annealing temperature, treatment time, oxygen partial pressure, and film thickness, as well as extend the analysis to in situ high-temperature electrical measurements and complementary first-principles calculations to further clarify the atomistic mechanisms governing oxygen-vacancy evolution and carrier transport in β-Ga_2O_3 thin films.

References

[1] L. Gu *et al.*, "Temperature-Dependent Oxygen Annealing Effect on the Properties of Ga2o3 Thin Film Deposited by Atomic Layer Deposition," *SSRN Electron. J.*, May 2022, doi: 10.2139/SSRN.4100243.

[2] C. W. Ku, S. T. Chung, F. G. Tarntair, C. L. Hsiao, and R. H. Horng, "Study of thermal annealing on gallium oxide heteroepitaxial layers grown on SiC for vertical Schottky barrier diodes applications," *Appl. Surf. Sci. Adv.*, vol. 24, p. 100661, Dec. 2024, doi: 10.1016/J.APSADV.2024.100661.

[3] F. Hrubišák *et al.*, "The effect of hydrogen annealing on the electrical properties of β-Ga2O3/4H-SiC MOSFETs grown by liquid-injection MOCVD," *Mater. Sci. Semicond. Process.*, vol. 206, p. 110402, May 2026, doi: 10.1016/J.MSSP.2025.110402.

[4] S. Jana, S. Pal, and D. Basak, "Defect-driven photocarrier dynamics and thermal quenching of photocurrent in β-Ga2O3 thin films," *Mater. Today Commun.*, vol. 52, p. 114932, Mar. 2026, doi: 10.1016/J.MTCOMM.2026.114932.

[5] J. H. Choi, Y. Y. Huh, C. H. Jo, N. Ahmad, M. Saleem, and J. H. Koh, "Strategic oxygen vacancy control via defect engineering in β-Ga2O3 using rapid thermal annealing for advanced electronics," *Opt. Mater. (Amst).*, vol. 168, p. 117389, Nov. 2025, doi: 10.1016/J.OPTMAT.2025.117389.

[6] Y. Guan, Q. Hou, Y. Gu, and Z. Wang, "First-principles study of the effect of Mn and point vacancies with different valence states on the magnetic properties of ZnO," *Mater. Today Commun.*, vol. 26, p. 101805, Mar. 2021, doi: 10.1016/J.MTCOMM.2020.101805.

[7] L. Zhang *et al.*, "First-principles study on formation and action mechanism of intrinsic Ga and O vacancy in β-Ga_2O_3," *Comput. Mater. Sci.*, vol. 268, p. 114676, Apr. 2026, doi: 10.1016/J.COMMATSCI.2026.114676.

[8] R. Tian, M. Pan, Q. Sai, L. Zhang, H. Qi, and H. F. Mohamed, "Crucial Role of Oxygen Vacancies in Scintillation and Optical Properties of Undoped and Al-Doped β-Ga2O3 Single Crystals," *Cryst. 2022, Vol. 12, Page 429*, vol. 12, no. 3, p. 429, Mar. 2022, doi: 10.3390/CRYST12030429.

[9] V. Janardhanam *et al.*, "Enhancement of device performance in β-Ga2O3 Schottky barrier diodes with tetramethylammonium hydroxide treatment," *Colloids Surfaces A Physicochem. Eng. Asp.*, vol. 693, p. 134079, Jul. 2024, doi: 10.1016/J.COLSURFA.2024.134079.

[10] A. K. Singh, M. Gupta, V. Sathe, and Y. S. Katharria, "Effect of annealing temperature on β-Ga2O3 thin films deposited by RF sputtering method," *Superlattices Microstruct.*, vol. 156, p. 106976, Aug. 2021, doi: 10.1016/J.SPMI.2021.106976.

[11] A. V. Almaev *et al.*, "Impact of Cr2O3 additives on the gas-sensitive properties of β-Ga2O3 thin films to oxygen, hydrogen, carbon monoxide, and toluene vapors," *J. Vac. Sci. Technol. A Vacuum, Surfaces, Film.*, vol. 39, no. 2, Mar. 2021, doi: 10.1116/6.0000723/397505.

[12] M. S. Bae, S. H. Kim, J. S. Baek, and J. H. Koh, "Comparative Study of High-Temperature Annealed and RTA Process β-Ga2O3 Thin Film by Sol–Gel Process," *Coatings 2021, Vol. 11, Page 1220*, vol. 11, no. 10, p. 1220, Oct. 2021, doi: 10.3390/COATINGS11101220.

[13] J. Jesenovec, M. H. Weber, C. Pansegrau, M. D. McCluskey, K. G. Lynn, and J. S. McCloy, "Gallium vacancy formation in oxygen annealed β-Ga2O3," *J. Appl. Phys.*, vol. 129, no. 24, Jun. 2021, doi: 10.1063/5.0053325.

[14] S. Zhang *et al.*, "Oxygen vacancies modulating performance for Ga2O3 solar-blind photodetectors via low-cost mist chemical vapor deposition," *Mater. Today Commun.*, vol. 39, p. 108717, Jun. 2024, doi: 10.1016/J.MTCOMM.2024.108717.

[15] P. Mandal, A. Mondal, A. Pandey, S. R. Meitei, and A. Bag, "Investigating role of annealing in shaping morphological,

structural, tribological, and optical characteristics of gallium oxide (Ga2O3): Insights from DFT analysis," *J. Alloys Compd.*, vol. 1011, p. 178367, Jan. 2025, doi: 10.1016/J.JALLCOM.2024.178367.
[16] Y. Yuan *et al.*, "Toward emerging gallium oxide semiconductors: A roadmap," *Fundam. Res.*, vol. 1, no. 6, pp. 697–716, Nov. 2021, doi: 10.1016/J.FMRE.2021.11.002.
[17] S. Wu, Z. Liu, H. Yang, and Y. Wang, "Effects of Annealing on Surface Residual Impurities and Intrinsic Defects of β-Ga2O3," *Crystals*, vol. 13, no. 7, p. 1045, Jul. 2023, doi: 10.3390/CRYST13071045/S1.

Information about authors:
Ruslan Kalibek – Master Student, Research Assistant, Faculty of Engineering, Süleyman Demirel University, 1/1 Almatinskaya st., Almaty, Kazakhstan, rus.kalibek@bk.ru
Daria Sopyryaeva – MSc, Academic Associate, Institute of Physics, Technical University of Berlin, 17 Straße des, Berlin, Germany, dsopyryaeva@mail.ru

Author Contributions:
Ruslan Kalibek – concept, methodology, resources, data collection, visualization, interpretation, drafting, funding acquisition.
Daria Sopyryaeva – testing, modeling, analysis, editing.

Conflict of Interest: The authors declare no conflict of interest.

Use of Artificial Intelligence (AI): The authors declare that AI was not used.

Received: 04.04.2026
Revised: 10.06.2026
Accepted: 21.06.2026
Published: 30.06.2026

Technobius Physics, 2026, 4(2), 0054, DOI: https://doi.org/10.54355/tbusphys/30070147.4.2.2026.0054

Technobius Physics

https://technobiusphysics.kz/

e-ISSN 3007-0147

Editorial

Emerging directions in thermal physics, materials science, and data-driven modeling

Aida Nazarova*

15/3 Sauran street, 43, 010000, Astana, Republic of Kazakhstan
*Correspondence: technobiusphysics@gmail.com

The articles presented in this issue collectively illustrate the increasingly interdisciplinary character of contemporary physics research, where classical physical principles are being complemented by advanced computational techniques, artificial intelligence, and materials engineering. Although each contribution addresses a distinct scientific problem, together they demonstrate how modern approaches are reshaping the study of thermal phenomena across multiple length scales and application domains.

The issue opens with an investigation of building energy demand and energy systems, highlighting the importance of heat transfer analysis for improving energy efficiency in the built environment. As global efforts continue toward sustainable development and carbon reduction, accurate thermal modeling remains essential for optimizing building performance and supporting evidence-based engineering decisions.

The second contribution explores defect-mediated charge transport in anisotropic two-dimensional semiconductors using machine-learning-assisted modeling. This work exemplifies the growing integration of data-driven methodologies with condensed matter physics, demonstrating how artificial intelligence can accelerate the understanding of complex electronic transport mechanisms while reducing computational cost.

Artificial intelligence also plays a central role in the third article, which presents the application of Physics-Informed Neural Networks (PINNs) to model heat diffusion in anisotropic solids. By embedding governing physical laws directly into neural network architectures, PINNs represent a promising alternative to conventional numerical methods, offering new opportunities for solving complex inverse and forward problems in heat transfer and continuum physics.

The next contribution investigates the thermal stability and fire resistance of vinyl ester resin composites containing various fillers. By examining the influence of filler composition on thermal degradation mechanisms and flame-retardant performance, the study contributes to the development of safer, more durable composite materials capable of operating under demanding thermal conditions. Such investigations highlight the continuing importance of materials engineering in improving both the performance and reliability of advanced structural systems.

The final contribution in this issue presents a comprehensive experimental investigation of β-Ga_2O_3 thin films, focusing on the role of oxygen-vacancy engineering in determining their structural, electrical, and dielectric properties. By combining X-ray diffraction, electron microscopy, X-ray photoelectron spectroscopy, Raman spectroscopy, Hall-effect measurements, temperature-dependent electrical transport, dielectric spectroscopy, and impedance analysis within a unified experimental framework, the study establishes quantitative relationships between defect chemistry and functional

material performance. The reported results demonstrate how controlled post-deposition annealing can simultaneously influence crystallographic ordering, carrier mobility, electrical conductivity, dielectric response, and thermally activated transport, providing valuable guidance for the optimization of ultra-wide-bandgap oxide semiconductors intended for next-generation power electronics, ultraviolet optoelectronics, and dielectric devices.

Taken together, the contributions published in this issue highlight several important directions that are shaping contemporary physical research. Advanced numerical simulations continue to deepen our understanding of heat transfer and energy-related processes, while machine learning and physics-informed artificial intelligence are emerging as powerful tools for solving complex problems in computational physics. At the same time, experimental studies on wide-bandgap semiconductors and thermally resistant composite materials demonstrate the continuing importance of defect engineering, advanced characterization techniques, and materials design in developing next-generation electronic and structural systems. Collectively, these studies illustrate how the integration of experimental investigations, computational modeling, and data-driven methodologies is driving innovation across modern physics and materials science.

The Editorial Board hopes that the contributions presented in this issue will encourage further interdisciplinary collaboration among physicists, materials scientists, computational researchers, and engineers. The convergence of physics-based modeling, artificial intelligence, and materials innovation is expected to remain one of the defining directions of scientific progress in the coming years.

Finally, we invite our readers to actively engage with the research presented in this issue. Scientific progress is driven by the careful exchange of ideas, critical discussion, and the appropriate acknowledgment of previous work. We hope that the articles published in Technobius Physics will serve as valuable references for future investigations and contribute to the continued advancement of physics and related disciplines. We also encourage readers to share these contributions within their professional networks, helping to expand their visibility and foster new scientific collaborations.

We sincerely thank all authors for their valuable contributions and the reviewers for their careful evaluations, constructive recommendations, and commitment to maintaining high scientific standards. Their collective efforts ensure the quality and integrity of every issue published by Technobius Physics.

We trust that the research published in this issue will stimulate further scientific discussion, inspire new investigations, and contribute to the continued advancement of thermal physics, condensed matter research, computational modeling, and materials science.

Published: 30.06.2026